

ALGEBRAIC MULTISCALE FINITE-VOLUME METHODS FOR
RESERVOIR SIMULATION

A DISSERTATION
SUBMITTED TO THE DEPARTMENT OF ENERGY RESOURCES
ENGINEERING
AND THE COMMITTEE ON GRADUATE STUDIES
OF STANFORD UNIVERSITY
IN PARTIAL FULFILLMENT OF THE REQUIREMENTS
FOR THE DEGREE OF
DOCTOR OF PHILOSOPHY

Hui Zhou

May 2010

© Copyright by Hui Zhou 2010
All Rights Reserved

I certify that I have read this dissertation and that, in my opinion, it is fully adequate in scope and quality as a dissertation for the degree of Doctor of Philosophy.

(Hamdi A. Tchelepi) Principal Adviser

I certify that I have read this dissertation and that, in my opinion, it is fully adequate in scope and quality as a dissertation for the degree of Doctor of Philosophy.

(Louis J. Durlofsky)

I certify that I have read this dissertation and that, in my opinion, it is fully adequate in scope and quality as a dissertation for the degree of Doctor of Philosophy.

(Seong H. Lee)

Approved for the University Committee on Graduate Studies.

Abstract

One of the major challenges in reservoir simulation is posed by the existence of multiple scales in reservoirs and the resulting high resolution geophysical models. It is usually too expensive to compute directly on the finest geo-cellular scale. On the other hand, the accuracy of simulating subsurface flow relies strongly on the detailed geophysical properties of natural heterogeneous formations. Multiscale methods have been shown to be very promising to bridge the gap between the geological and flow-simulation scales. However, there are a few limitations in existing multiscale methods, e.g., the extension to physical mechanisms (such as compressibility, gravity and capillary pressure), and difficulties for cases with channelized permeability or high anisotropy. Moreover, the multiscale method has been applied only to the flow problem for efficient solutions of the pressure and velocity fields, while the transport problem is solved on the fine scale. In this work, we develop an algebraic multiscale framework for coupled flow and transport problems in heterogeneous porous media.

An operator-based multiscale method (OBMM) is proposed to solve general multiphase flow problems. The key ingredients of the method are two algebraic multiscale operators, prolongation and restriction, with which the multiscale solution can be constructed algebraically. It is straightforward to extend OBMM to general flow problems that involve more physical mechanisms, such as compressibility, gravity and capillary pressure. The efficiency and accuracy of OBMM are demonstrated by a wide range of problems.

An adaptive multiscale formulation for the saturation equations is developed within the algebraic multiscale framework, which is the first multiscale treatment of transport problems. Our multiscale formulation employs a conservative restriction operator and three adaptive prolongation operators. For the time interval of interest, the physical domain is divided into three distinct regions according to the coarse-scale saturation solution. Then, different prolongation operators are defined and used adaptively in different regions to construct the fine-scale saturation field. The multiscale computations of coupled flow and transport further improve the computational efficiency over the original multiscale finite-volume method, which is already significantly more efficient than fine-scale methods.

An efficient two-stage algebraic multiscale (TAMS) method is also developed, which overcomes the limitations of the multiscale finite-volume method for channelized permeability fields and highly anisotropic problems. The TAMS method consists of two stages, one global and one local. In the global stage, a multiscale solution is obtained purely algebraically from the fine-scale matrix. The prolongation operator is obtained algebraically using the wirebasket ordered reduced system of the original fine-scale coefficient matrix. In the second stage, a local solution is constructed from a simple block preconditioner, such as Block ILU(0) (BILU), or an Additive Schwarz (AS) method. The TAMS method is purely algebraic and only needs the fine-scale coefficient matrix and the wirebasket ordering information of the multiscale grid. Thus, the TAMS method can be applied as a preconditioner for solving the large-scale linear systems associated with the flow problem. The TAMS method converges rapidly even for problems with channelized permeability fields and high anisotropy ratios. TAMS also preserve the favorable property of local mass conservation of the multiscale finite-volume method. Therefore, the TAMS method can be applied as either an efficient linear solver or a fast approximation approach with very good accuracy.

Acknowledgements

The writing of the dissertation is a long journey for me. There was frustration at some point during this journey, but when it comes to the end, what remain in my mind are only pride and joy. It would have not been possible without the support of many people. My sincere gratitude goes to my advisor, my parents, my wife, my brother, my friends and the faculty and staff in the Department of Energy Resources Engineering at Stanford University.

My deepest gratitude is to my advisor, Professor Hamdi Tchelepi. During my five years at Stanford University, I learned tremendously from Hamdi not only on research but also on many other aspects that will be beneficial to all my life, such as how to communicate with people, plan work and face difficulties. His patience and support helped me overcome many challenging situations and complete this dissertation. I owe special thanks to Hamdi for careful reading of many drafts of this dissertation and being so considerate in my graduation schedule. I have been amazingly fortunate to have him as my advisor.

I wish to thank Professor Lou Durlofsky for his insightful comments and constructive discussions at different stages of my research, which helped me a lot. I am also grateful to him for carefully reading and commenting on my dissertation.

I am grateful to Dr. Seong Lee for taking me as an intern in two summers. It has been a true pleasure to work with him. The discussions with him helped me sort out many technical details and spark new ideas. He has always been there to listen and

give advice even after my internship was over. I am deeply grateful for his continuous encouragement and guidance.

Thanks are also due to Professor Khalid Aziz for his support and advice. I especially appreciate his comments and suggestions during my PhD oral defense, which has inspired me a lot. I am thankful to Professor Biondo Biondi for kindly sharing my PhD oral defense.

I owe many thanks to the Department of Energy Resources Engineering of Stanford University, all the faculty, staff and my fellow students for making the department such an attractive place for pursuing PhD study. Specially, I wish to thank Karyn Borella for taking care of so many steps of my graduation.

Many friends have helped me through my years at Stanford. I greatly value their friendship and I deeply appreciate their support. Specially, I would like to take this opportunity to acknowledge Yuanlin Jiang, Yaqing Fan, Jianbing Wu, Yongshe Liu, Yuguang Chen, Qing Chen, Tianhong Chen, Yulin Jin, Chunmei Shi, Jerome Onwunali, Pipat Likanapaisal, Xiaochen Wang, Yifan Zhou and Yang Liu.

Most importantly, nothing would have been possible without the love and support of my family. They have been a constant source of love, support and strength all these years. I thank my wife, Jing Peng, from the bottom my heart. We have always been together, experiencing happiness and joy, and sharing sadness and sorrow. Her unwavering love has strengthened me and made my life so much easier and happier. My parents have encouraged and supported my education since I was a little kid. Their unconditional support is so precious for me. I would also like to thank my younger brother Xionghui for taking care of the family when I was away.

Nomenclature

Domains and Related

Ω^c	primal coarse-scale grid
Ω^d	dual coarse-scale grid
Ω^f	fine-scale grid
C_r	coarsening ratio
L_x, L_y, L_z	lengths of physical domain
n_c	dimension of coarse-scale grids
n_f	dimension of fine-scale grids

Matrices and Vectors

\mathbf{A}	fine-scale matrix
\mathbf{A}^c	coarse-scale matrix
\mathcal{P}	prolongation operator
\mathbf{q}	fine-scale right hand side vector
\mathbf{q}^c	coarse-scale right hand side vector

\mathcal{R} restriction operator

M^{-1} preconditioner

Superscripts and Subscripts

i, j, k indices for fine-scale grids

I, J, K indices for coarse-scale grids

f denotes fine-scale variable

c denotes coarse-scale variable

ms denote multiscale solutions

w denotes well variable

FM solution by fine-scale method

$MSOM$ multiscale solution by original method

$MSAT$ multiscale solution by adaptive transport computation

Thresholds

Δ_1 saturation threshold to detect Region 1 and Region 2 for adaptive transport computation

Δ_2 saturation threshold to detect Region 2 and Region 3 for adaptive transport computation

Δ_ξ threshold for using the AS operator in Region 3

Δ_v velocity threshold to detect Region 2 and Region 3 for adaptive transport computation

ϵ_λ	mobility threshold for adaptive updating basis functions
ϵ_g	gravity threshold for adaptive updating correction functions
ϵ_{pc}	capillary pressure threshold for adaptive updating correction functions

Variables

\mathbf{k}	absolute permeability
λ_l	mobility of phase l
μ_l	viscosity of phase l
ϕ	porosity
Φ_l	hydraulic potential of phase l
ρ_l	density of phase l
\mathbf{u}_l	velocity of phase l
\mathbf{u}_t	total velocity
b_l	inverse of formation volume factor of phase l
f_l	fractional flow of phase l
H	depth of physical domain
p	pressure
p_E	pressure of edge cells
p_I	pressure of interior cells
p_V	pressure of vertex cells

q_l source term of phase l

S_l saturation of phase l

Contents

Abstract	v
Acknowledgements	vii
1 Introduction	1
1.1 Motivation for Multiscale Methods	1
1.2 Upscaling Methods	5
1.2.1 Upscaling of Flow	5
1.2.2 Upscaling of Transport	8
1.3 Multiscale Methods	9
1.3.1 Dual-Grid Methods	10
1.3.2 Multiscale Finite-Element Methods	11
1.3.3 Variational Multiscale Methods	14
1.3.4 Multiscale Finite-Volume Methods	16
1.3.5 Multiscale Methods for Transport	18
1.4 Objectives of Work	19
1.5 Outline	22
2 General Algebraic Multiscale Framework	24
2.1 Introduction	24

2.2	Model Problem and Discrete Formulation	26
2.3	Operator Based Multiscale Method	29
2.3.1	Notations	30
2.3.2	General Framework	31
2.3.3	Prolongation Operator for Pressure	33
2.3.4	Restriction Operator	35
2.4	Application of OBMM to Flow Problems	38
2.4.1	Simple Flow Model	38
2.4.2	Extension to Compressibility	41
2.4.3	Extension to Gravity and Capillary Pressure	43
2.5	Fine-scale Velocity and Saturation	44
2.5.1	Fine-Scale Velocity Reconstruction	45
2.5.2	Fine-scale Saturation Computation	46
2.6	Computational Aspects of OBMM for Flow	46
2.6.1	Adaptive Computation	46
2.6.2	Computational Complexity	49
2.7	OBMM for Complex Physics	51
2.7.1	1D Single-Phase Compressible Flow	52
2.7.2	2D Two-Phase Compressible Flow	53
2.7.3	Gravity Segregation	59
2.8	General Two-phase Flows	64
2.8.1	Effects of Coarsening Ratio	66
2.8.2	Effects of Threshold on Adaptive Computation	68
2.9	Limitations of OBMM	71
2.10	Conclusions	75

3	Multiscale Modeling of Multiphase Transport	78
3.1	Introduction	78
3.2	Restriction and Prolongation Operators	81
3.2.1	Prolongation Operator I: Full Velocity-Full Saturation (FVFS)	86
3.2.2	Prolongation Operator II: Approximate Velocity-Full Saturation (AVFS)	87
3.2.3	Prolongation Operator III: Approximate Saturation (AS) . . .	89
3.3	Adaptive Computation of Saturation	90
3.4	Computational Aspects	92
3.4.1	Algorithm for Coupled Flow and Transport Problems	92
3.4.2	Computational Complexity	92
3.5	Numerical Examples	95
3.5.1	Incompressible Two-Phase Flow and Transport	96
3.5.2	More General Problems	111
3.5.3	Efficiency Study	120
3.6	Conclusions	125
4	Two-Stage Algebraic Multiscale Solver	128
4.1	Introduction	128
4.2	Algebraic Multiscale Solver(AMS)	131
4.3	Two-Stage Algebraic Multiscale Solver	135
4.3.1	Convergence Analysis of AMS	135
4.3.2	TAMS	140
4.3.3	Local Mass Conservation of TAMS	146
4.4	Numerical Performance of TAMS	148
4.4.1	Convergence Study	148
4.4.2	Conservation Study	151

4.4.3	Efficiency Study	154
4.4.4	Scalability Analysis	160
4.5	Conclusions	162
5	Conclusions and Future Work	165
5.1	Summary and Conclusions	165
5.2	Recommendations for Future Work	170
	Bibliography	172

List of Tables

2.1	Errors and percentage of the recomputed basis functions at several timesteps for the compressible flow in SPE10 top layer	58
2.2	Errors and percentage of the recomputed basis functions at several times for the vertical segregation in heterogeneous reservoir	64
2.3	Properties used for the study of general two-phase flows.	65
2.4	Pressure and saturation errors and percentage of recomputed basis and correction functions for different coarsening ratios	67
2.5	Pressure and saturation errors and percentage of recomputed basis and correction functions for different adaptivity thresholds	70
3.1	Error norms and adaptivity statistics for Case 1 with homogeneous permeability: e_p and e_s are L_2 error norms for pressure and saturation, respectively. The f_p denotes the fraction of updated pressure basis functions employed from the initial time to the current time step. The f_I and f_{II} , respectively, denote the fraction of Prolongation Operators I and II employed in the transport computations from the initial time to the current time step.	102
3.2	Error norms and adaptivity statistics for Case 2 with log-normal permeability: the variables are defined in the caption of Table (3.1). . . .	105

3.3	Error norms and adaptivity statistics for Case 3: the variables are defined in the caption of Table (3.1).	109
3.4	Statistics of error and ratios of full construction at various time steps for Case 4	115
3.5	Statistics of error and fraction of full construction at various time steps for Case 5.	117
3.6	Statistics of error and fraction of full construction at various time steps for buoyancy-driven flow.	121
3.7	CPU comparisons for 3D models at $t = 0.6PVI$	123
3.8	Groups of transport adaptivity thresholds	124
3.9	Statistics of error and ratios of full construction at various time steps for three groups of adaptivity thresholds. The values for e_p , e_s , f_I and f_{II} in the table denote percentages (i.e., 1.27 means 1.27%).	124
4.1	The TAMS algorithm for the Richardson iterative scheme.	141
4.2	Various options and parameters for TAMS	157
4.3	GMRES iterations and solver CPU time (seconds) of TAMS with different options and parameters for the two three-dimensional cases.	158
4.4	Comparison of CPU time for TAMS and AMG in the efficiency test cases.	159
4.5	Iteration numbers and CPU time for different sizes of problems	161
4.6	Iteration numbers and CPU time for different coarsening ratios.	162

List of Figures

1.1	Two-dimensional multiscale grid in MsFVM. The enlarged dual control volume shows the underlying fine grid.	16
2.1	A two-dimensional multiscale grid: the bold solid and dashed lines indicate the coarse grid (Ω^c) and dual coarse grid (Ω^d), respectively; solid thin lines denotes the fine grid (Ω^f).	30
2.2	A dual block in a multiscale grid.	34
2.3	Support dual blocks (dashed lines) for primal coarse node K in a multiscale grid	35
2.4	1D multiscale grid.	39
2.5	The pseudo code of OBMM with SFI scheme for one timestep.	47
2.6	Speedup of OBMM for flow problem	51
2.7	Comparison of pressure results of OBMM, FSA, and fine-scale reference solution for 1D single-phase gas flow at three times.	53
2.8	Log-permeability of the top layer of the SPE 10 model.	54
2.9	Fine-scale pressure at $t = 5 \times 10^{-3}\tau$: (a) using fine-scale method; (b) using OBMM.	55
2.10	Fine-scale oil saturation at $t = 5 \times 10^{-3}\tau$: (a) using fine-scale method; (b) using OBMM.	56

2.11	Fine-scale pressure at $t = 0.2\tau$: (a) using fine-scale method; (b) using OBMM.	56
2.12	Fine-scale oil saturation at $t = 0.2\tau$: (a) using fine-scale method; (b) using OBMM.	57
2.13	Fine-scale pressure at $t = 1\tau$: (a) using fine-scale method; (b) using OBMM.	57
2.14	Fine-scale oil saturation at $t = 1\tau$: (a) using fine-scale method; (b) using OBMM.	58
2.15	Vertical segregation problem	59
2.16	Multiscale solution for the vertical segregation in homogeneous reservoir at $t = 1\tau$	61
2.17	The multiscale saturation and the reference fine-scale saturation are identical for the vertical segregation in a homogeneous reservoir. . . .	62
2.18	Log-normal permeability field	62
2.19	Comparison of the multiscale solutions of pressure and saturation with the fine-scale reference for the vertical segregation in a heterogeneous reservoir: solid lines denote reference solution, dotted lines denote multiscale solution.	63
2.20	Fine-scale reference saturation and multiscale saturation for different coarsening ratios at $t = 1\tau$	67
2.21	Fine-scale reference saturation and multiscale saturation for different adaptivity thresholds	69
2.22	Recovery and production history of the fine-scale and the multiscale method with different adaptivity thresholds: blue lines denote the ratio of recovered oil and red lines represent the fraction of oil in the production well	70
2.23	Permeability and pressure solutions for the SPE 10 bottom layer . . .	73

2.24	Permeability and pressure solutions for the anisotropic case	74
3.1	Typical Buckley-Leverett saturation profiles at time t and $t + \Delta t$ for a 1D problem divided into three regions.	83
3.2	Adaptive multiscale computation of both flow and transport	93
3.3	Speedup of MSAT over MSOM for transport	95
3.4	Pressure distribution at $t = 0.2$ PVI in Case 1 with homogeneous per- meability	98
3.5	Saturation distribution at $t = 0.2$ PVI for Case 1 with homogeneous permeability	98
3.6	Pressure distribution at $t = 0.8$ PVI for Case 1 with homogeneous permeability	99
3.7	Saturation distribution at $t = 0.8$ PVI for Case 1 with homogeneous permeability	99
3.8	Adaptive saturation computation at three times for Case 1: the white and black squares, respectively, denote the regions where Prolonga- tion Operators I and II are used, at least once, during the iterative saturation computation for the particular time step.	100
3.9	Cumulative oil recovery and oil fraction for Case 1	101
3.10	Pressure distribution at $t = 0.2$ PVI in Case 2 with log-normal perme- ability	103
3.11	Saturation distribution at $t = 0.2$ PVI in Case 2 with log-normal per- meability	104
3.12	Pressure distribution at $t = 0.8$ PVI in Case 2 with log-normal perme- ability	104
3.13	Saturation distribution at $t = 0.8$ PVI in Case 2 with log-normal per- meability	105

3.14	Adaptive saturation computation for three time steps in Case 2: the white and black squares respectively denote the region where Prolongation Operator I and II is applied, at least once, in iterative saturation calculation of the time step.	106
3.15	Cumulative oil recovery and oil fraction in production (oil cut) in Case 2	106
3.16	Pressure distribution at $t = \tau_o$ in Case 3 with Dirichlet boundary condition	108
3.17	Saturation distribution at $t = \tau_o$ in Case 3 with Dirichlet boundary condition	108
3.18	Pressure distribution at $t = 4\tau_o$ in Case 3 with Dirichlet boundary condition	109
3.19	Saturation distribution at $t = 4\tau_o$ in Case 3 with Dirichlet boundary condition	109
3.20	Adaptive saturation computation for three time steps in Case 3: the white and black squares respectively denote the region where Prolongation Operator I and II is applied respectively, at least once, in iterative saturation calculation for this time step.	110
3.21	Cumulative Oil recovery and oil fraction in production (oil cut) in Case 3	111
3.22	Pressure contours of fine-scale and multiscale results at 0.3, 0.8, 1.5 PVI time for a quarter of five-spot injection case. Solid lines denote fine-scale solution and dash lines denote multiscale solution.	113
3.23	Saturation contours of fine-scale and multiscale results at 0.3, 0.8, 1.5 PVI time for a quarter of five-spot injection case . Solid lines denote fine-scale solution and dash lines denote multiscale solution.	114

3.24	Adaptive computation of saturation at 0.3, 0.8, 1.5 PVI time for a quarter of five-spot injection case. The white squares denote the regions where full construction of velocity and saturation (FVFS) is used while the black squares denote the regions where full construction of saturation is obtained using linearly interpolated velocity (AVFS). In regions without squares, direct interpolation of saturation (AS) is applied. . .	114
3.25	Cumulative oil recovery and oil fraction in production for Case 4 . . .	115
3.26	Pressure contours of fine-scale and multiscale results at 0.8, 1.0, 1.5 PVI time for a quarter of five-spot injection with switch of injector and producer at 0.75 PVI. Solid lines denote fine-scale solution and dash lines denote multiscale solution.	117
3.27	Saturation contours of fine-scale and multiscale results at 0.3, 0.8, 1.5 PVI time for a quarter of five-spot injection with switch of injector and producer at 0.75 PVI. Solid lines denote fine-scale solution and dash lines denote multiscale solution.	117
3.28	Adaptive computation of saturation at three time steps for a quarter of five-spot injection with switch of injector and producer at 0.75 PVI. The squares are defined as in Fig. (3.24).	118
3.29	Cumulative oil recovery and oil fraction in production for a quarter of five-spot injection with switch of injector and producer at 0.75 PVI. .	118
3.30	Pressure contours of fine-scale and multiscale results at 0.5τ , 1.0τ , 2.0τ PVI time for buoyancy-driven flow. Solid lines denote fine-scale solution and dash lines denote multiscale solution.	120
3.31	Saturation contours of fine-scale and multiscale results at 0.5τ , 1.0τ , 2.0τ PVI time for buoyancy-driven flow. Solid lines denote fine-scale solution and dash lines denote multiscale solution.	120

3.32	Adaptive computation of saturation at three time steps for buoyancy-driven flow. The squares are defined as in Fig. (3.24).	121
3.33	Logarithmic permeability for the fine grid of size $45 \times 45 \times 48$	122
3.34	Adaptive computation of saturation at 0.8 PVI for three groups of adaptive thresholds. The white squares denote the regions where full construction of velocity and saturation (FVFS) is used while the black squares denote the regions where full construction of saturation is obtained using linearly interpolated velocity (AVFS). In regions without squares, direct interpolation of saturation (AS) is applied.	125
4.1	The multiscale grid with the wirebasket ordering	132
4.2	The full spectra of the iteration matrix of AMS (denoted by dots) for an isotropic homogeneous case.	138
4.3	Eigenvectors of AMS iteration matrix that are associated with the largest and smallest eigenvalues (1 and 0, respectively).	139
4.4	Eigenvectors of A^{-1} and M_{ms}^{-1} with the highest frequency.	139
4.5	Eigenvectors of A^{-1} and M_{ms}^{-1} with the lowest frequency.	140
4.6	The full spectra of the iteration matrix(denoted by dots) for the isotropic homogeneous case.	142
4.7	Histogram of the eigenvalues of the iteration matrix for the isotropic homogeneous case.	142
4.8	Eigenvectors of M_{TAMS}^{-1} with the highest and lowest frequencies . . .	143
4.9	Eigenvectors of the local preconditioner M_{BILU}^{-1} with the highest and lowest frequencies	144
4.10	The full spectra of the iteration matrix(denoted by dots) for the isotropic homogeneous case: the block size of BILU is 4×4	144

4.11	The histogram of the spectra of the iteration matrix for the isotropic homogeneous case: the block size of BILU is 4×4	144
4.12	The natural logarithm of the top layer of the SPE 10 permeability. . .	145
4.13	The spectra of the TAMS iteration matrix for the SPE 10 top layer permeability field.	145
4.14	The natural logarithm of heterogeneous permeability for convergence study.	149
4.15	The convergence histories for homogeneous and heterogeneous cases with $\alpha = 1, 10$ (the legend of the plots shown in (e)).	150
4.16	Pressure solutions of the fine-scale reference, the TAMS method (after one iteration) and the AMS in the case of conservation study	153
4.17	Conservation errors after one iteration of TAMS	153
4.18	Conservation errors after one iteration of TAMS followed by applying one step of AMS with the finite-volume type restriction operator and a reconstruction process	153
4.19	Fine-scale reference saturation and saturation computed from the reconstructed velocity or directly from TAMS	154
4.20	Saturation error versus the number of TAMS iterations	155
4.21	The natural logarithm of the log-normal distributed permeability field.	156
4.22	The logarithm of the SPE 10 permeability field.	156
4.23	Solution of the log-normal case.	156
4.24	Solution of the SPE 10 case.	156
4.25	The natural logarithm of heterogeneous permeability for scalability study.	161
4.26	The increase of CPU time with problem sizes. The CPU time and problems size are normalized by those of the $32 \times 32 \times 32$ problem . .	161

Chapter 1

Introduction

1.1 Motivation for Multiscale Methods

In the past few years, there has been increasing interest in multiscale methods for a wide range of physics and engineering problems. The growth in this area is motivated by (1) the complexity and inherent multiscale nature of many challenging problems across a wide range of disciplines, (2) the rapid growth of computational power, and (3) the need to solve highly detailed multiscale, multi-physics problems accurately and efficiently. For most problems that involve a wide range of scales (in the coefficients or solutions), it is often too expensive to compute on the smallest (finest) scale even with state-of-the-art super-computers. This is because the finest scale contains too many unknowns, especially if relatively large length and time scales are of interest. On the other hand, computing on a larger (coarse) scale exclusively may not be accurate because the fine-scale properties usually have a significant impact on the coarse-scale behavior. Moreover, it is often the case that the coarse-scale properties and governing equations are not well defined.

Most existing multiscale methods combine fine-scale and coarse-scale computations to resolve the most important fine-scale information efficiently without having

to compute directly on the global fine-scale problem. For instance, in solid mechanics, the coarse-scale (macroscopic) continuum theory is coupled with molecular dynamics on the fine-scale (microscopic) to compute accurate macroscopic behaviors of materials [Car and Parrinello, 1985; Zhang et al., 1999; Li and E, 2005]; in computational fluid dynamics, coarse-scale hydrodynamics and fine-scale kinetic models are coupled to capture the distribution of shocks [Le Tallec and Mallinger, 1997; Schwartzentruber and Boyd, 2006]. Multiscale methods have also been applied to study turbulent flow [Hughes et al., 2001], and nano materials [Liu et al., 2004].

Flow in porous media is another important application area for multiscale methods. The understanding of flow in porous media is fundamental to many branches of engineering, such as petroleum, civil and environmental engineering. In our work, we focus on applications in petroleum engineering and subsurface CO₂ sequestration. In petroleum engineering, numerical modeling of multiphase flow in porous media is often referred to as reservoir simulation, and the computer program that is used for reservoir simulation is called a reservoir simulator. Reservoir simulation is now an essential tool for quantitative reservoir management in the oil and gas industry. It has been applied to improve petroleum production, design optimal development plans, understand reservoir features through history matching, and assess uncertainties associated with production decisions. Therefore, research on reservoir simulation is of great importance, both academically and industrially.

One of the major challenges in reservoir simulation is posed by the existence of multiple scales in reservoirs and the resulting high-resolution reservoir description models. A reservoir, which is a subsurface geological formation, is usually of the scale of miles in the areal dimensions. On the other hand, reservoir properties, such as porosity and permeability typically show strong heterogeneity and may vary over many scales from the pore scale (10 μ m), the core scale (10cm) to the geological scale (1km). Modern reservoir characterization and geostatistical modeling techniques are

able to integrate information from these different scales, and build geo-cellular models that describe the reservoir properties in great detail [Caers, 2005]. Such geo-cellular models are often quit large and may contain $O(10^7) - O(10^8)$ grid cells. It is, however, too expensive to solve multiphase flow problems on these large-scale geo-cellular grids even with state-of-the-art reservoir simulators and computing facilities. Typically, a reservoir simulator handles models with $10^5 - 10^6$ grid cells. Furthermore, many applications in petroleum engineering, such as history matching, production optimization, and uncertainty assessment, require performing large numbers of simulations. For such computationally demanding applications, the robustness and efficiency of the reservoir simulator are crucial requirements.

It is thus practically infeasible to compute directly on the finest geo-cellular scale; on the other hand, the accuracy of simulating subsurface flow relies strongly on the detailed geological properties of the heterogeneous porous medium [Bachu and Cuthiell, 1990]. The governing equations for flow and transport in porous media are the mass conservation equations for each fluid component in the reservoir. Those equations can be further expressed as a pressure equation and several saturation equations. The pressure equation is often referred to as the flow equation and the saturation equations as the transport equations. Both porosity and permeability are important factors in the governing equations. The spatial variations of permeability result in complex pressure distributions of the pressure, total and phase velocities, and saturation.

Similar to multiscale modeling in other scientific areas, we hope to capture the most important fine-scale effects that are essential for accurate description of the multiphase flow and transport behaviors, without direct solution on the global fine-scale problem.

It is also important to note that, there is one significant difference between multiscale methods for flow in porous media and for other areas (e.g., solid mechanics, computational fluid dynamics). The scales in reservoir formations are continuous

and inseparable, and they span a very rich set of length scales. Heterogeneity exists across all scales from the pore to the reservoir, but there are no obvious separations between the various scales. In contrast, problems in many other fields have obvious scale separation. For example, in solid mechanics, the molecular scale is well defined and periodic boundary conditions can be applied to localize fine-scale problems. Therefore, multiscale methods that rely on scale separation [E and Engquist, 2003; E et al., 2003] are not directly applicable for the coupled flow and transport problems in porous media. We need to develop multiscale methods that take into account the complex hierarchy of scales associated with natural geologic formations.

Extensive research and development have been performed to resolve the scale gap between the geo-cellular and flow-simulation models. Upscaling is a classical technique that aims to develop accurate coarse-scale models that are amenable for numerical flow computations. However, traditional upscaling techniques lose the fine-scale details during the dynamic flow simulation process, which may lead to significant deterioration in accuracy as the actual flow process of interest differs significantly from the upscaling assumptions. Multiscale methods, on the other hand, are aimed at the fine-scale resolution of the dynamic flow process of interest.

Recent advances in multiscale methods show great promise in efficiently simulating large-scale models for highly heterogeneous porous media. However, there are several limitations in existing multiscale methods. These include extension to complex physical mechanisms, such as compressibility, gravity and capillary pressure, and difficulties for cases with channelized permeability or high anisotropy ratio in mobility. Moreover, existing multiscale methods have focused on the flow problem (i.e., pressure and total-velocity) only, while the transport problem is solved on the fine scale. In this dissertation, we aim to develop efficient and accurate multiscale methods that are well suited for simulating coupled flow and transport equations. Moreover, the developed methods must provide high-quality approximations as well

as fully converged fine-scale solutions when necessary. It is also important to employ algebraic description and implementation of the developed multiscale algorithms in order to ensure efficiency and extensibility.

In this chapter, we first review upscaling methods for flow and transport problems. Then, a survey of various multiscale methods are presented. Advantages and limitations of existing methods are discussed. We then discuss the specific objectives of our work and the organization of this dissertation.

1.2 Upscaling Methods

Upscaling, or homogenization, techniques have been widely used to solve large scale subsurface flow problems. The main idea of upscaling is to compute effective properties on a coarse scale by some pre-processing steps, and then solve the coarse-scale equations. The governing equations for subsurface flow can be split into the flow problem (pressure equation) and the transport problem (saturation equations). Consequently, upscaling can be classified into upscaling of flow and upscaling of transport. For comprehensive reviews of upscaling methods, refer to Wen and Gómez-Hernández [1996]; Renard and de Marsily [1997]; Christie [2001]; Farmer [2002]; Durlofsky [2003] and Chen [2005].

1.2.1 Upscaling of Flow

Upscaling of flow focuses on calculating effective coarse-scale reservoir properties, such as porosity and permeability, for single-phase flow or the pressure equation of multiphase flow. The permeability, which is also referred to as absolute permeability, is the most often considered upscaling parameter. Upscaling of absolute permeability can be performed by deterministic, heuristic, or stochastic approaches as described in Renard and de Marsily [1997]. Heuristic upscaling includes power-law averaging

in coarse blocks [Journal et al., 1986; Deutsch, 1989] and the renormalization approach that calculates permeability by a series of successive aggregation [King, 1989]. Stochastic upscaling considers permeability as a random function in space, and the effective permeability is determined as the mathematical expectation from the governing stochastic differential equations. Other methods involve the statistical expansion of geometric averaging [Dagan, 1993], and calculating the stochastic expectation from the block permeability [Rubin and Gómez-Hernández, 1990; Gómez-Hernández and Journal, 1990]. A critical review for stochastic upscaling can be found in Wen and Gómez-Hernández [1996].

Our interest is in deterministic upscaling schemes, among which flow-based upscaling methods are the most widely used due to their accuracy and flexibility [Durlofsky, 1992]. The basic idea of flow-based upscaling is to solve fine-scale flow problems over some region corresponding to each coarse-scale block and then use the solutions to calculate effective coarse-scale parameters. The region used for fine-scale calculation can be chosen to be the target coarse block, the entire global domain, or something in between, for example, the target coarse block plus some extended neighboring fine cells. Depending on the choices of the calculation regions, flow-based upscaling can accordingly be classified into local, global, and extended local upscaling.

It is also important to choose boundary conditions for the calculation regions, which have a significant impact on the upscaling results. A widely used boundary condition for local upscaling is constant pressure and no-flow, in which pressure is fixed on the boundaries vertical to the flow direction, and no-flow boundary conditions are specified on the boundaries parallel to the flow direction. Durlofsky [1991; 1992] proposed to use periodic boundary conditions for local upscaling, which guarantees symmetry and positive-definiteness of the effective permeability. Pickup et al. [1994] further showed the accuracy and robustness of using periodic boundary conditions for general heterogeneous permeability fields. Other boundary conditions including the

linear pressure boundary condition have also been applied [King and Mansfield, 1999]. Generally, the quality of local upscaling deteriorates when the actual flow scenario of interest deviates from linear flow, which is the case for radial flow in near wellbore regions, or when permeability fields have large-scale structures, such as channels. By construction, local upscaling does not account for effects that depend on large-scale global structures, which can be quite important for accurate representation of the pressure and velocity fields.

Global upscaling, on the other hand, calculates the coarse-scale properties based on fine-scale solutions over the entire domain for a simplified flow process. A commonly used procedure is to apply a specific global flow scenario to obtain coarse-scale properties that minimize the pressure and velocity errors between the global fine- and coarse-scale solutions [Nielsen and Tveito, 1998; Holden and Nielsen, 2000]. Global upscaling overcomes the limitation of local upscaling in near-well regions and channelized permeability fields, but it is computationally much more expensive than local methods and also strongly dependent on the specific flow scenario.

Extended local upscaling falls between local and global upscaling. It is quite similar to local upscaling, except that the fine-scale problem is solved on an extended local domain, which comprises the target coarse block and some neighboring cells. The use of an extended domain can reduce the influence of the local boundary conditions and improve the quality of the upscaling results. Wen et al. [2003a; 2003b] applied extended local upscaling to practical geological models and obtained improved results for channelized permeability fields compared with local upscaling.

More recently, Chen et al. [2003] and Chen and Durlofsky [2006] developed local-global upscaling methods, in which the global coarse-scale solution is used to determine appropriate boundary conditions for the local upscaling calculation. Global coarse- and local fine-scale problems are solved iteratively to achieve consistency. In the coupled local-global upscaling approach [Chen et al., 2003], two generic global

flows (linearly-independent flows in x and y directions of two-dimensional problems) are applied, which may cause the upscaled properties to be process-dependent. The adaptive local-global upscaling [Chen and Durlofsky, 2006], on the other hand, applies a specific global flow and flow-based criterion that is used to determine where the local boundary conditions need to be updated. Only a portion of the local regions need to be solved.

1.2.2 Upscaling of Transport

The upscaling, or coarsening, of the nonlinear transport (saturation) equations is much more challenging than that of the pressure equations. The first reason is that the transport equations are strongly time dependent and so are the parameters in these equations. Thus, it is not possible to develop pre-processed time independent parameters for coarse-scale transport computation. The second reason is due to the nature of the hyperbolic transport equations, where the interactions of the saturation front and underlying heterogeneous permeability are strongly nonlinear and the non-local effect on the transport is dominant [Hou et al., 2006].

The pseudo relative permeability approach was proposed by Kyte and Berry [1975] to construct coarse-scale transport parameters. The pseudo relative permeability is generated from reference fine-scale simulation models. Kyte and Berry [1975] used average pressures and fluxes to compute coarse-scale pseudo-relative permeability for each coarse block. Stone [1990] directly used the total mobility to obtain pseudo functions. These are two major categories of methods for calculation of pseudo relative permeability. Ekrann and Mykkeltveit [1995] showed that the calculation of pseudo functions generally depends on the reference fine-scale solution from which they are derived. Barker and Thibeu [1997] and Barker and Dupouy [1999] also pointed out the dependency of pseudo relative permeability on the flow scenario. The inaccuracy of computing pseudo relative permeability functions makes it difficult to reproduce

the fine-scale solution, even without considering physical mechanisms such as gravity and capillarity [Barker and Thibeu, 1997; Barker and Dupouy, 1999]. Christie et al. [2000] and Wallstrom et al. [2002a;b] proposed effective flux boundary conditions for the calculation of pseudo relative permeability, and they showed that more accurate results can be obtained.

Efendiev and Durlofsky [2002] and Efendiev et al. [2000a] derived a non-local time dependent macro-dispersion model that incorporates subgrid effects. In their model, the macro-dispersion contribution was estimated based on coarse-scale streamlines and the magnitude of the local velocity fluctuations. Later, Efendiev and Durlofsky [2003] developed a generalized convection-diffusion model for the coarse-scale transport equations. A modified convection term and an extra diffusion term are used to capture the subgrid effects. Hou et al. [2006] derived a mathematical framework for the homogenized equations for the coupled pressure and saturation equation by projecting the fluctuation onto averages along streamlines. This method is able to remove the limitation of small fluctuations in the quantities considered by Efendiev et al. [2000a]. However, the method is still technically subject to the limitation of small variance in the permeability field, due to the requirement of scale separation in deriving the formulation.

1.3 Multiscale Methods

Multiscale methods have many similarities with upscaling, but there are also some significant differences. The objective of multiscale modeling is to obtain efficient and accurate approximation to the fine-scale solution, while the intent of upscaling is usually to generate approximate coarse-scale solutions. In some sense, multiscale methods are local-global approaches, where the local solutions are used to provide fine-scale information, while the global solutions provide global coarse-scale information.

However, the coarse-scale system in multiscale methods is constructed numerically and dynamically using current fine-scale information instead of pre-processed coarse-scale quantities. Thus, multiscale methods are usually process independent, since no prior flow scenarios are assumed. This makes multiscale methods good candidates for general-purpose reservoir simulation. Moreover, the natural coupling between local and global scales in multiscale methods avoids the inconsistency and non-physical coarse-scale properties that are often associated with many multiphase upscaling techniques. As with upscaling methods, different multiscale solution strategies have to be applied to the pressure and transport equations.

1.3.1 Dual-Grid Methods

Current multiscale approaches for reservoir simulation are designed to devise an efficient numerical algorithm using two numerical scales. There had been some early work in reservoir simulation where both coarse- and fine-scale flow information are obtained without directly solving the full fine-scale problem. Such methods are referred to as “dual-grid” methods instead of multiscale methods as some significant differences between them and multiscale methods exist.

Ram  and Killough [1991] solved the elliptic pressure equation by a high order finite-element method on a coarse grid and then projected the pressure to a fine-scale grid. Gu rillot and Verdi re [1995] further extended this approach by using a geometric averaged coarse permeability for the coarse grid and solving local flow problems to obtain the fine-scale solution in each coarse block. Gautier et al. [1999] proposed a nested dual grid approach for fast simulation of both flow and transport in heterogeneous domains. A standard flow-based upscaling method was employed to obtain the coarse-scale solutions. Then, local flow problems with Neumann boundary conditions derived from the coarse-scale fluxes are solved to reconstruct the fine-scale velocity field, in which streamline simulation was applied to solve the transport

problem.

One common drawback of these dual-grid methods is that the fine- and coarse-scale problems are not coupled properly. The coarse-scale system is nearly independent of the local fine-scale solution, and improvements in the local fine-scale solutions appear to have very limited effects on the coarse scale. On the other hand, the fine-scale solutions are quite strongly dependent on the coarse-scale approximations. Thus, when the quality of the coarse-scale solutions deteriorates, the fine-scale solutions also degrade. It has been shown that the performance of dual-grid methods degenerates for highly heterogeneous permeability fields [Audigane and Blunt, 2004].

1.3.2 Multiscale Finite-Element Methods

Recently developed multiscale methods for the flow problem have much stronger coupling between the fine and coarse scales. Since they are very closely related to the proposed approaches in this dissertation, we review them in more detail.

Hou and Wu [1997] first introduced the multiscale finite-element method (MsFEM) as an efficient algorithm to solve the following elliptic problem,

$$-\nabla \cdot \lambda(\mathbf{x}) \nabla u = f \quad \text{in } \Omega. \quad (1.1)$$

The main idea of the MsFEM is to construct basis functions that represent the local fine-scale information. Then, the finite-element space is represented by these basis functions, i.e.,

$$\mathcal{V}_h = \text{span}\{\phi_K^i; i = 1, \dots, d; K \in \mathcal{K}^h\} \subset H_0^1(\Omega), \quad (1.2)$$

where \mathcal{K}^h denotes a partition of Ω , d denotes the number of nodes of element K , ϕ_K^i is the basis functions of a local node i in element K , and $H_0^1(\Omega)$ is the Hilbert functional space defined on Ω . Hou and Wu [1997] proposed to solve the basis functions locally

in each coarse element with reduced boundary conditions, i.e.,

$$\begin{aligned} \nabla \cdot \lambda(\mathbf{x}) \nabla \phi_K^i &= 0 \quad \text{in } \Omega_K^c, \\ \frac{\partial}{\partial x_t} \left(\lambda(\mathbf{x}) \frac{\partial \phi_K^i}{\partial x_t} \right) &= 0, \end{aligned} \tag{1.3}$$

where Ω_K^c is the domain of coarse element K , superscript i denotes a node in that element, and subscript t denotes the component parallel to a coarse element boundary. In addition, the basis function should possess the interpolation property, i.e.,

$$\begin{aligned} \sum_{i=1}^d \phi_K^i(\mathbf{x}) &= 1, \\ \phi_K^i(\mathbf{x}_j) &= \delta_{ij} \quad i, j = 1, \dots, d, \end{aligned} \tag{1.4}$$

where \mathbf{x}_j is the coordinate of node j of element K .

Different from conventional finite-element methods, the basis functions of the MsFEM are usually obtained numerically using Eq. (1.3). Other than that, the MsFEM follows the same procedure as standard finite-element methods to solve for the coarse nodal variables. Then, the fine-scale information can be naturally retrieved using the basis functions, i.e.,

$$u(\mathbf{x}) = \sum_{i=1}^d \phi_K^i(\mathbf{x}) u_i \quad \text{if } \mathbf{x} \in \Omega_K^c. \tag{1.5}$$

It was pointed out by Hou and Wu [1997] that when the scale of oscillations in the coefficients (e.g., permeability) is close to the scale of the grid, there will be large errors due to “resonance” of the two scales. They found that the resonance error can be virtually eliminated by improving the boundary conditions of the basis functions. For that purpose, they proposed an oversampling method. The idea is to impose the reduced boundary condition on a sampled domain that is larger than

a coarse element. The basis functions use only information in the interior region of the computational domain. Thus, the boundary layers of the computational domain, where the resonance error is pronounced, have less influence on the basis functions.

Solutions of MsFEM are not locally conservative and cannot be applied to solve the transport equations for multiphase flow and transport problems in porous media. Later, Chen and Hou [2003] presented a multiscale formulation based on mixed finite-element methods and demonstrated clearly that a locally conservative algorithm is a necessary requirement for accurate simulations of transport problems. This multiscale mixed finite-element method (MsMFEM) gives mass conservative velocity fields for both fine and coarse grid cells, where no source term is present. Aarnes [2004] and Aarnes et al. [2006] further extended the MsMFEM to provide mass conservative velocity fields for the entire fine grid. Here, we describe the MsMFEM based on the approach of Aarnes [2004] and Aarnes et al. [2006]. The MsMFEM takes the pressure, p , and the total-velocity, \mathbf{u} , to be the main variables in the finite-element formulation of the flow equation:

$$\nabla \cdot \mathbf{u} = q, \quad \mathbf{u} = -\mathbf{k} \nabla p \quad \text{in } \Omega. \quad (1.6)$$

The weak form reads: find $(\mathbf{u}, p) \in H_0^1(\Omega) \times L^2(\Omega)$ such that,

$$\begin{aligned} (\mathbf{k}^{-1} \mathbf{u}, \mathbf{v}) - (p, \nabla \cdot \mathbf{v}) &= 0, \quad \forall \mathbf{v} \in H_0^1(\Omega), \\ (\nabla \cdot \mathbf{u}, w) &= (q, w), \quad \forall w \in L^2(\Omega), \end{aligned} \quad (1.7)$$

where $L^2(\Omega)$ is the Sobolev square integrable functional space over Ω , and (\cdot, \cdot) denotes the integration over Ω . The MsMFEM formulation seeks an approximate solution, (\mathbf{u}_h, p_h) , in the finite-dimensional space $\mathbf{V} \in H_0^1(\Omega)$ that satisfies the weak form, Eq. (1.7). The MsMFEM employs a generalization of the lowest-order Raviat-Thomas method (RT0) for the solution belonging to the spaces $(\mathbf{V}^{ms}, \mathcal{P}_0(\mathcal{T}_H))$. Here, $\mathcal{P}_0(\mathcal{T}_H)$ is piecewise constant over the coarse mesh, \mathcal{T}_H , and \mathbf{V}^{ms} consists of velocity basis

functions of the RT0 method that account for fine-scale variations. The velocity basis function in a pair of coarse blocks E_i and E_j , denoted by $\boldsymbol{\psi}_{ij}$, satisfies

$$\begin{aligned} \boldsymbol{\psi}_{ij} &= -\mathbf{k}\nabla\phi_{ij}, \\ \nabla \cdot \boldsymbol{\psi}_{ij} &= \begin{cases} w_i(x)/\int_{E_i} w_i(\xi) \, d\xi, & \text{for } x \in E_i, \\ -w_j(x)/\int_{E_j} w_j(\xi) \, d\xi, & \text{for } x \in E_j, \end{cases} \\ \boldsymbol{\psi}_{ij} \cdot \mathbf{n} &= 0, \quad \text{on } \partial(E_i \cup E_j). \end{aligned} \tag{1.8}$$

Aarnes [2004] pointed out that w_i should coincide with the source term q in elements containing source terms to ensure local mass conservation. For elements with $q = 0$, several choices for w_i exist, and the quality of the velocity basis functions were found to depend on the specific choice. Aarnes [2004] recommended using

$$w_i(x) = \begin{cases} \text{trace}(\mathbf{k}(x)), & \text{if } q(\xi) = 0, \, \forall \xi \in E_i, \\ q(x), & \text{otherwise.} \end{cases} \tag{1.9}$$

One advantage of the multiscale (mixed) finite-element method is in dealing with complex grids, such as unstructured and non-conforming grids [Aarnes et al., 2006; 2008; Gulbransen et al., 2009].

1.3.3 Variational Multiscale Methods

The variational multiscale method (VMS) was first proposed by Hughes [1995] and Hughes et al. [1998]. The idea is to split the solution space into a coarse-scale space and a family of mutually orthogonal subgrid spaces. The discrete formulation is also based on finite-element methods. That is to say, the difference between VMS and MsFEM is in the approximate solution space on which a finite-element formulation is defined.

Arbogast [2002] and Arbogast and Bryant [2002] proposed a conservative numerical subgrid upscaling approach which is essentially a multiscale mixed finite element method based on VMS. In their approach, the lowest-order Brezzi-Douglas-Marini space (BDM1) [Brezzi et al., 1985] is used for the coarse-scale functional space and RT0 is used for the subgrid (fine-scale) space. Let \mathcal{T}_h and \mathcal{T}_H denote the fine and coarse-scale meshes, respectively. Also, let (\mathbf{V}_H, W_H) be the BDM1 approximation spaces over \mathcal{T}_H . The subgrid spaces are defined on each coarse element of \mathcal{T}_H . For example, in a coarse element E_c , the fine-scale pressure space, $W_h(E_c)$, and the velocity space, $\mathbf{V}_h(E_c)$, satisfy

$$\begin{aligned} W_h(E_c) &= \{w_h \in \mathcal{P}_0(\mathcal{T}_h)|_{E_c} : (w_h, 1)|_{E_c} = 0\}, \\ \mathbf{V}_h(E_c) &= \{\mathbf{v}_h \in \mathbf{V}^{RT0}(\mathcal{T}_h)|_{E_c} : \mathbf{v}_h \cdot \mathbf{n} = 0 \text{ on } \partial E_c\}. \end{aligned} \tag{1.10}$$

The approximation spaces are then given by the following direct sums,

$$\begin{aligned} W_{H,h} &= W_H \bigoplus_{E_c \in \mathcal{T}_H} W_h(E_c), \\ \mathbf{V}_{H,h} &= \mathbf{V}_H \bigoplus_{E_c \in \mathcal{T}_H} \mathbf{V}_h(E_c). \end{aligned} \tag{1.11}$$

Note that no-flow boundary conditions are used to localize the basis function computation, which is a strong assumption. Juanes and Dub [2008] instead assumed the integral of the fluxes on the boundary of each coarse element to be zero, which helps to account for subgrid velocity variation across element interfaces. The relationship between MsMFEM and the mixed finite-element version of VMS has also been studied in Arbogast and Boyd [2006], and numerical comparisons between them were reported by Kippe et al. [2008].

1.3.4 Multiscale Finite-Volume Methods

Multiscale finite-volume methods are developed based on the finite-volume discretization of the pressure equations. They inherit many advantages of the finite-volume method, most importantly the local mass conservation.

Jenny et al. [2003] developed the first multiscale finite-volume method (MsFVM) for flow problems. Besides the primal coarse and fine grids, a dual coarse grid is constructed by connecting centers of all primal coarse blocks as shown in Fig. (1.1). The

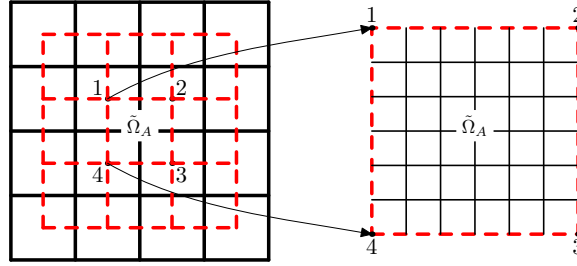


Figure 1.1: Two-dimensional multiscale grid in MsFVM. The enlarged dual control volume shows the underlying fine grid.

basic idea of the MsFVM [Jenny et al., 2003] is to construct pressure basis functions on the dual coarse grid and then use them to calculate effective transmissibility on the primal coarse grid. With the effective transmissibility field, one can construct a coarse-scale system for the pressure equation, and then project the coarse-scale solutions onto the fine grid by applying the basis functions.

The basis functions of the MsFVM [Jenny et al., 2003] are very similar to those in the MsFEM [Hou and Wu, 1997]. The basis functions are computed locally in each dual coarse block, one basis function for each vertex. Here, we consider the elliptic equation, Eq. (1.1). The flux term is defined by

$$\mathbf{v} = -\lambda(\mathbf{x})\nabla u, \quad (1.12)$$

based on Eq. (1.1). A finite-volume discretization formulation for coarse block Ω_A^c is to approximate the mass conservation equation

$$\int_{\Omega_A^c} \nabla \cdot \mathbf{v} \, d\Omega = \oint_{\partial\Omega_A^c} \mathbf{v} \cdot \mathbf{n} \, d\Gamma = - \int_{\Omega_A^c} f \, d\Omega \quad (1.13)$$

by coarse-scale variables as

$$\oint_{\partial\Omega_A^c} \mathbf{v} \cdot \mathbf{n} \, d\Gamma = \sum_{K=1}^N T^K \bar{u}^K, \quad (1.14)$$

where \bar{u}^K is the (coarse-scale) finite-volume pressure solution in coarse cell K , N is the total number of coarse cells, and T^K denotes the coarse-scale effective transmissibility. The fine-scale pressure can be written in terms of basis functions. For example, the fine-scale pressure inside dual coarse cell $\tilde{\Omega}_A$, as shown in Fig. (1.1), can be expressed as

$$u(\mathbf{x}) = \sum_{i=1}^4 \phi_A^i(\mathbf{x}) \bar{u}^{i(A)}, \quad \text{if } \mathbf{x} \in \tilde{\Omega}_A, \quad (1.15)$$

where $i(A)$ denotes the coarse node corresponding to the i -th vertex of $\tilde{\Omega}_A$. Thus, the transmissibility T^K can be expressed as a linear superposition of basis functions.

By construction (i.e., Eq. (1.13)), the mass conservation equation is satisfied on the primal coarse grid in the MsFVM. Thus, the reconstructed fine-scale pressure, Eq. (1.15), gives a velocity field that is mass conservative on the primal coarse grid. However, this velocity field is not conservative on the fine grid, and this is due to the reduced boundary conditions used for the basis functions. Specifically, the velocity field calculated from the reconstructed fine-scale pressure is usually not continuous across the interfaces of dual blocks.

Jenny et al. [2003] proposed to solve another set of basis functions on the primal coarse blocks to provide a locally conservative fine-scale velocity field. This set of basis

functions, referred to as primal basis functions, are used to construct the velocity field only. One drawback of this approach is that the number of primal basis functions associated with each coarse block is large, i.e., twenty-seven on three-dimensional Cartesian grids. Although adaptive computation can be used to reduced the cost of basis function computation [Jenny et al., 2004], a more straightforward way is to directly compute a conservative fine-scale velocity field by solving a Neumann problem for each primal coarse block [Jenny et al., 2006] as

$$\begin{aligned} \mathbf{v} &= -\lambda \nabla u, \quad \nabla \cdot \mathbf{v} = f, & \text{in } \Omega_A^c, \\ \mathbf{v} \cdot \mathbf{n} &= -\bar{q}, & \text{on } \partial\Omega_A^c, \end{aligned} \tag{1.16}$$

where \bar{q} is the flux calculated from the reconstructed fine-scale pressure on the interfaces of the primal coarse blocks. An additional advantage of this approach is that it allows for more flexibility to include additional physics such as compressibility and gravity [Lunati and Jenny, 2006; Lee et al., 2008; Tchelepi et al., 2007; Lunati and Jenny, 2008].

1.3.5 Multiscale Methods for Transport

As with upscaling, multiscale modeling of transport is more challenging than the flow problem. One difficulty is exactly the same as in upscaling: the coarsening of transport equations. The strong non-local and nonlinear effects in the transport equation make it very difficult to define basis functions that are local for the construction of the coarse-scale saturation equation. For multiscale modeling, the situation is further complicated by the requirement to reconstruct the fine-scale saturation field.

Due to these reasons, most existing multiscale methods only solve the flow problem by multiscale computation. A conservative fine-scale velocity field is first obtained, and then the transport equations are solved on the fine scale [Jenny et al., 2004; 2006;

Arbogast and Bryant, 2002; Aarnes et al., 2006].

Recently, Aarnes and Efendiev [2006] proposed two coarse-to-fine grid interpolators for the transport equations. In the local approach, the transport equation of a coarse grid is solved with a fixed velocity field and arbitrary initial saturation boundary conditions. The saturation evolution in a fine cell provides the interpolation operator. In the global approach, the local boundary conditions for the transport equation in a coarse grid are continuously updated using the global solution of the previous time-step. Their first algorithm is somewhat similar to the traditional pseudo relative permeability approach. The local boundary conditions can be quite different from the global solution and can incur significant errors in the interpolation operation. Their second algorithm is more accurate than the first one, but it is only slightly less expensive than full simulation on the fine grid. More recently, Efendiev et al. [2008] employed a flow-based coordinate system to model flow and transport using multiscale methods. In their approach, the physical grid system is transformed into a flow-based coordinate system based on global fine-scale information. Then the coarse-scale saturation equations are constructed by averaging across streamlines. Actually, the purpose of both Aarnes and Efendiev [2006] and Efendiev et al. [2008] is not to get the fine scale saturation correctly, but rather to introduce a mechanism to model transport on the coarse scale more accurately by using the multiscale solution on the flow problem.

1.4 Objectives of Work

Multiscale methods have two main advantages over upscaling: the ability to resolve fine-scale solutions efficiently and the avoidance of computing effective coarse-scale properties that are process dependent. The strong coupling between the fine and

coarse scales allows multiscale methods to construct a high-quality coarse-scale system based on current fine-scale information and then reconstruct accurate fine-scale solutions. As a result, our overall objective is to develop a multiscale framework for coupled multiphase flow and transport in porous media.

The MsFVM ensures local mass conservation, which is crucial for solving the transport equations. Violation of local mass conservation may result in unbounded and non-physical saturation solutions. Furthermore, compared with other multiscale methods (e.g., MsFEM and VMS), it is easier to extend the MsFVM to complex flow problems with additional physical mechanisms other than incompressible flow (such as compressibility, gravity and capillary pressure). So far, only the MsFVM has been applied to general multiscale flow problems describe by the black-oil model[Lee et al., 2008]. Therefore, our work here focuses on the multiscale finite-volume formulation.

The first objective of our work is to extend the MsFVM to a general algebraic multiscale framework, such that various physical mechanisms can be incorporated easily, efficiently and accurately. In the past, several approaches have been proposed to treat compressibility, gravity and capillary pressure in the MsFVM [Lunati and Jenny, 2006; 2008; Lee et al., 2008]. However, these approaches need to introduce additional models and assumptions, which complicate the implementation and limit applicability and extendibility. Note that in my master thesis [Zhou, 2006], we developed an operator-based multiscale formulation that can incorporate compressibility effects. To simplify the coupling between pressure and saturation equations, the IMPES (Implicit Pressure and Explicit Saturation) scheme was used for multiphase flow problems, which suffers from possibly severe limits on the time step. Here, the objective is to solve more general multiphase flow problems (not only compressible flow) in an algebraic multiscale framework based on a sequential fully implicit scheme.

The second objective is to develop an efficient multiscale formulation for the transport problems. As discussed in the previous sections, existing multiscale methods

solve the transport problems on the fine scale. With the efficiency of the pressure solution greatly improved by multiscale treatment, the computational cost of reconstructing the fine-scale velocity and solving the fine-scale transport becomes the bottleneck in terms of overall efficiency. Thus, we aim to further improve the efficiency of the original MsFVM by developing a multiscale treatment of the transport problems. Note that different from Aarnes and Efendiev [2006] and Efendiev et al. [2008], the purpose here is to obtain accurate fine-scale saturation fields.

Although existing multiscale finite-volume methods have shown good accuracy for a wide range of problems, it is also known that the reconstructed multiscale solution differs from the true fine-scale solution. While these errors are often small, they can become significant for problems with channelized permeability fields with severe permeability contrasts and in highly anisotropic problems. Therefore, the third objective of this work is to develop a two-stage algebraic multiscale method that guarantees error reduction to any specified tolerance and that ensures local mass conservation at any tolerance. Such a capability can be applied as either an efficient linear solver, or as a fast approximation approach with desired accuracy.

In summary, our objectives are:

1. develop a general algebraic multiscale framework that incorporates different physical mechanisms associated with flow and transport easily, efficiently and accurately;
2. develop an efficient multiscale formulation for transport problems;
3. develop a multiscale method that is able to converge to the fine-scale solution and ensure local mass conservation.

1.5 Outline

This dissertation is organized as follows. Chapter 2 presents a general algebraic multiscale framework. The main components of this framework are two algebraic multiscale operators, namely restriction and prolongation. Thus, the multiscale method developed here is referred to as operator-based multiscale method (OBMM). The construction strategies of the two operators are discussed in detail. We show that the OBMM can be easily applied to general flow problems with complex physics, such as compressibility, gravity and capillary pressure. Simplified computational complexity analysis reveals that OBMM can be much more efficient (an order of magnitude and more) than a fine-scale method. The efficiency of OBMM can be further improved by choosing appropriate coarsening ratios and thresholds for adaptive computation. We test the proposed method using several challenging cases including compressibility driven depletion and gravity segregation problems, which shows the OBMM results are in very good agreement with the reference fine-scale solutions. The effects of various computational parameters, such as the coarsening ratio and the adaptivity threshold values, are studied for general two-phase flow problems.

In Chapter 3, an adaptive multiscale formulation for transport problems is described. This multiscale formulation employs a conservative restriction operator and three adaptive prolongation operators. For the time interval of interest, the physical domain is divided into three distinct regions according to the coarse-scale saturation solution. Then, different prolongation operators are defined and used adaptively in different regions to construct the fine-scale saturation field. The multiscale computations of coupled flow and transport are more efficient than the original multiscale finite-volume method, which is already significantly more efficient than fine-scale methods. We test the adaptive multiscale formulation of transport using a series of

problems with different permeabilities (homogeneous and heterogeneous) and boundary conditions (no-flow and Dirichlet). Challenging cases with additional physical mechanisms, such as compressibility and gravity, and changing well locations are also investigated. It is demonstrated that the results obtained with the proposed method are very accurate for a wide range of problems.

In Chapter 4, we present an efficient two-stage algebraic multiscale solver (TAMS). The TAMS consists of two stages, one global and one local. In the global stage, a multiscale solution is obtained purely algebraically from the fine-scale coefficient matrix. The prolongation operator is obtained algebraically using a wirebasket order of a reduced system obtained from the original fine-scale matrix. In the second stage, a local solution is constructed using a simple block preconditioner. Spectral analysis is used to show that the two-stage method can resolve the full spectra of the fine-scale matrix and achieve fast convergence. It is also demonstrated that the TAMS allows for the reconstruction of a locally conservative fine-scale velocity field. Challenging large-scale problems with complex heterogeneous structures and high anisotropy ratios show that the TAMS is very robust and efficient with an appropriate choice of computational parameters.

In Chapter 5, we draw conclusions and suggest several future research directions.

Chapter 2

General Algebraic Multiscale Framework

2.1 Introduction

In this chapter, we describe a general multiscale framework for solving the flow problem in heterogeneous porous media in the presence of compressibility, gravity, and capillary pressure. An algebraic description of the overall algorithm is used, which makes it straightforward to implement the algorithm and extend its capabilities to problems with complex physical mechanisms and boundary conditions.

Specifically, we develop an algebraic operator based multiscale method (OBMM). The idea of OBMM was initiated in the author's master thesis [Zhou, 2006], where the OBMM was proposed to include compressibility in multiscale computation. For the incompressible (elliptic) flow problem, the OBMM is simply the algebraic form of the original MsFVM [Jenny et al., 2003]. The OBMM accounts for compressibility effects very accurately and efficiently. Here, we further extend the OBMM to more general flow problems that include compressibility, gravity and capillarity. Because the algorithm is purely algebraic, it is applicable for both structured and unstructured

grids and its implementation is simply a matter of linear algebraic operations. Moreover, since the algorithm is directly based on the fine-scale equations, it is relatively easy to develop multiscale solution strategies on top of existing fine-scale reservoir simulators.

Lunati and Jenny [2008] and Lee et al. [2008] used an operator splitting strategy to compute correction functions for gravity and capillary pressure. The correction functions capture the local effects that cannot be represented by the pressure basis functions employed in the original MsFVM [Jenny et al., 2003]. We show that it is quite straightforward to include the correction functions in the OBMM. Challenging numerical examples where gravity is dominant clearly show the accuracy of this treatment. Moreover, compared with the approaches of Lunati and Jenny [2008] and Lee et al. [2008], the OBMM is much easier to implement and allows for multiscale modeling of general problems in reservoir simulation. We present results using the OBMM for two-phase blackoil problems, which demonstrate the power of OBMM.

This chapter proceeds as follows. In Section 2.2, the flow and transport equations for a general two-phase problem are introduced. The finite-volume discretization is also presented. In Section 2.3, we introduce the operator based multiscale method for general discrete equations. Then, in Section 2.4 we discuss in detail how to incorporate different physics, such as compressibility, gravity and capillarity in the OBMM. The solution of transport problems based on the multiscale solution of the flow field is discussed in Section 2.5. Adaptive computation of the multiscale method and the computational efficiency are analyzed in Section 2.6. Numerical examples are presented in Section 2.7 to validate the ability of OBMM to model complex physics, which is followed by some sensitivity analysis of the effects of the coarsening ratio and adaptivity thresholds in Section 2.8. Section 2.9 provides a summary of the OBMM.

2.2 Model Problem and Discrete Formulation

We consider immiscible multiphase flow in porous media [Aziz and Settari, 1979]. Only two-phase flow is considered here for simplicity in illustrating the ideas. The extension from two-phase to three-phase flow is straightforward if the phases are completely immiscible with each other. Assume water and oil are the two phases. The mass conservation equations can then be written as:

$$\frac{\partial}{\partial t} (\phi S_l b_l) = \nabla \cdot (b_l \boldsymbol{\lambda}_l \cdot \nabla \Phi_l) - q_l, \quad (2.1)$$

where subscript $l = o, w$ denotes a phase; S_l , b_l , $\boldsymbol{\lambda}_l$, Φ_l and q_l are saturation, inverse of formation volume factor, mobility, potential, and volumetric flow rate of phase l , respectively. The phase mobility is defined by

$$\boldsymbol{\lambda}_l = \frac{\mathbf{k} k_{rl}}{\mu_l}, \quad (2.2)$$

where \mathbf{k} is the absolute permeability tensor, k_{rl} is the relative permeability and μ_l is viscosity. The absolute permeability, \mathbf{k} , usually plays a dominant role in subsurface flow and transport processes. The permeability is a complex function of space and reflects the multiscale heterogeneous structure of the porous formation. Consequently, a detailed description is required to resolve the large variability of \mathbf{k} , which in turn leads to a high-resolution reservoir models (e.g., more than one million cells). Efficient flow computation using highly resolved reservoir models is a significant challenge.

The phase potential is given by

$$\Phi_l = p_l - \rho_l g z, \quad (2.3)$$

where p_l is pressure in phase l , ρ_l is phase density, and z is depth. The saturation

constraint is

$$S_o + S_w = 1. \quad (2.4)$$

The phase pressures are related by

$$p_c = p_o - p_w, \quad (2.5)$$

where the capillary pressure, p_c , is in turn given by a capillary model, i.e.,

$$p_c = p_c(S_o). \quad (2.6)$$

Then, the semi-discrete form of Eq. (2.1) is written as

$$\frac{\phi^{n+1} b_l^{n+1} S_l^{n+1} - \phi^n b_l^n S_l^n}{\Delta t} = \{\nabla \cdot [b_l \boldsymbol{\lambda}_l (\nabla p_l - \rho_l g \nabla z)] - q_l\}^{n+1} \quad (l = o, w), \quad (2.7)$$

where Δt is the time step size, and superscripts n and $n + 1$ denote the previous and current time steps.

In multiscale methods, the flow (pressure and total velocity) and transport (saturation) problems are treated separately and differently. Typically, the flow and transport equations are solved sequentially using either an IMPES (Implicit Pressure Explicit Saturation) scheme [Jenny et al., 2004; Zhou, 2006] or a sequential fully implicit (SFI) scheme [Jenny et al., 2006; Tchelepi et al., 2007]. Here we adopt the SFI scheme, where an iterative procedure is used such that each iteration involves the solution of two implicit problems in sequence: one for flow and the other for transport.

Multiplying Eq. (2.7) by $\alpha_l \equiv 1/b_l^{n+1}$ and summing up the two equations, one

arrives at

$$\frac{\phi^{n+1}}{\Delta t} - \frac{\phi^n}{\Delta t} \sum_l \alpha_l^{n+1} b_l^n S_l^n = \sum_l \alpha_l^{n+1} \{ \nabla \cdot [b_l \boldsymbol{\lambda}_l (\nabla p_l - \rho_l g \nabla z)] - q_l \}^{n+1}. \quad (2.8)$$

We let $p_o = p$ and use it as a primary variable. Eq. (2.8) can be linearized using the first-order Taylor expansion. For simplicity, the coefficients in the convection terms (i.e., α_l, b_l, λ_l) are lagged by one iteration. The resulting linearized discrete pressure equation can be written as

$$C \frac{p^{\nu_p+1} - p^{\nu_p}}{\Delta t} - \sum_l \alpha_l^{\nu_p} \nabla \cdot (b_l^{\nu_p} \boldsymbol{\lambda}_l^{\nu_p} \nabla p^{\nu_p+1}) = R, \quad (2.9)$$

where ν_p and $\nu_p + 1$ denote the previous and current iteration levels of pressure, respectively. The other quantities in Eq. (2.9) are expressed as

$$\begin{aligned} \alpha_l^{\nu_p} &= 1/b_l^{\nu_p}, \quad (l = o, w), \\ C &= \left[\frac{\partial \phi}{\partial p} - \phi^n \sum_l b_l^n S_l^n \frac{\partial \alpha_l}{\partial p} + \Delta t \sum_l \frac{\partial (\alpha_l q_l)}{\partial p} \right]^{\nu_p}, \\ R &= -\frac{\phi^{\nu_p}}{\Delta t} + \frac{\phi^n}{\Delta t} \sum_l \alpha_l^{\nu_p} b_l^n S_l^n - \sum_l \alpha_l^{\nu_p} q_l^{\nu_p} - \sum_l \alpha_l^{\nu_p} \nabla \cdot (\rho_l^{\nu_p} g \boldsymbol{\lambda}_l \cdot \nabla z) \\ &\quad - \alpha_w^{\nu_p} \nabla \cdot (b_w^{\nu_p} \boldsymbol{\lambda}_w \nabla p_c). \end{aligned} \quad (2.10)$$

Once the pressure equation is solved at iteration level $\nu_p + 1$, the pressure distribution, p^{ν_p+1} , are used to obtain the total velocity, $\mathbf{u}_t^{\nu_p+1}$. The total velocity is the sum of the phase velocities, which are given by Darcy's law, i.e.,

$$\begin{aligned} \mathbf{u}_l &= -\boldsymbol{\lambda}_l (\nabla p_l - \rho_l g \nabla z) \quad (l = o, w), \\ \mathbf{u}_t &= \mathbf{u}_o + \mathbf{u}_w. \end{aligned} \quad (2.11)$$

In the SFI scheme [Jenny et al., 2006; Tchelepi et al., 2007], we fix the total velocity

and solve the nonlinear transport equation iteratively until it converges. The linearized transport equation for the oil phase at saturation iteration level ν_s can be written as

$$\begin{aligned} \frac{\phi^{\nu_p+1} b_o^{\nu_p+1} S_o^{\nu_s+1} - \phi^n b_o^n S_o^n}{\Delta t} = \nabla \cdot \left[b_l^{\nu_p+1} \left(\mathbf{u}_o|_{\mathbf{u}_t^{\nu_p+1}, S_o^{\nu_s}} + \frac{\partial \mathbf{u}_o}{\partial S_o} \Big|_{\mathbf{u}_t^{\nu_p+1}, S_o^{\nu_s}} \Delta S_o \right) \right] \\ - \left[q_o|_{p^{\nu_p+1}, S_o^{\nu_s+1}} + \frac{\partial q_o}{\partial S_o} \Big|_{p^{\nu_p+1}, S_o^{\nu_s}} \Delta S_o \right]. \end{aligned} \quad (2.12)$$

It is more convenient to express the phase velocities in terms of the total velocity to evaluate \mathbf{u}_o with fixed \mathbf{u}_t . One can define

$$\begin{aligned} \lambda_T &= \sum_{l=o,w} \lambda_l, \\ f_l &= \frac{k_{rl}/\mu_l}{\sum_l k_{rl}/\mu_l}, \end{aligned} \quad (2.13)$$

where λ_T is the total mobility, f_l is the phase fractional flow. Combining Eq. (2.11) and Eq. (2.13) gives

$$\mathbf{u}_o = f_o (\mathbf{u}_t + \lambda_w \Delta \rho g \nabla z - \lambda_w \nabla f_o p_c), \quad (2.14)$$

where $\Delta \rho = (\rho_w - \rho_o)$.

2.3 Operator Based Multiscale Method

The operator based multiscale method described here is an algebraic framework for performing multiscale computations for general problems. The main idea is to cast the multiscale scheme into algebraic operations using two multiscale operators, namely restriction and prolongation. With the two operators, a multiscale method can be easily represented. We use a notation that makes it easier to understand the similarities

and differences between multiscale and multigrid methods [Briggs et al., 2000].

2.3.1 Notations

We start with the notation used throughout the dissertation. Fig. (2.1) is a simple illustrative multiscale grid in two-dimensional space. We denote the fine-scale grid as

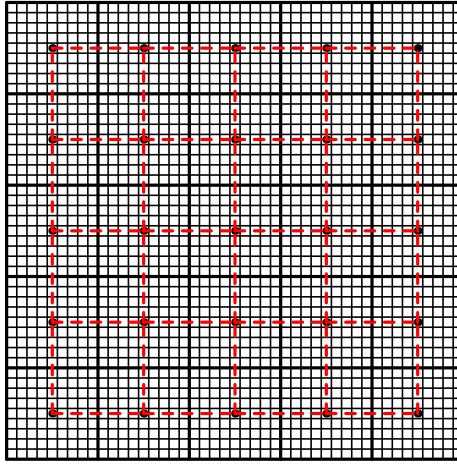


Figure 2.1: A two-dimensional multiscale grid: the bold solid and dashed lines indicate the coarse grid (Ω^c) and dual coarse grid (Ω^d), respectively; solid thin lines denotes the fine grid (Ω^f).

Ω^f and the coarse-scale grid, which is referred to as the primal coarse grid, as Ω^c . A second coarse grid, the dual coarse grid, denoted by Ω^d is constructed by connecting the centers of primal coarse cells. A cell of a grid is indicated by an indexed subscript of that grid, e.g., Ω_i^f means fine cell i in the fine-scale grid. Assume the fine grid contains n_f cells and the primal coarse grid contains n_c cells. The coarsening ratio C_r is defined as

$$C_r = \frac{n_f}{n_c}, \quad (2.15)$$

which is also referred to as upscaling ratio. It is often useful to write the coarsening ratio in terms of each dimension as $C_r = C_{r,x} \times C_{r,y} \times C_{r,z}$.

For convenience and when no confusion would be caused, Ω^f and Ω^c represent not only the numerical grids, but also the physical domains associated with them and the vector spaces defined on both grids.

2.3.2 General Framework

The fine-scale finite-volume discretization system of the pressure equation (Eq. (2.9)) and the saturation (Eq. (2.12)) can be written into a general form

$$\mathbf{A}\mathbf{u}^f = \mathbf{q} \quad \text{for } \mathbf{u}^f \in \Omega^f, \quad (2.16)$$

where \mathbf{u}^f is the solution vector in the space Ω^f , which is of dimension n_f . Direct solution of Eq. (2.16) is often too expensive. We use an algebraic multiscale method that projects the system into a coarse space by defining two multiscale operators, prolongation and restriction.

The prolongation operator defines the interpolation from the coarse space to the fine space, so that

$$\mathbf{u}^f = \mathcal{P}\mathbf{u}^c, \quad (2.17)$$

where the prolongation operator \mathcal{P} is of dimension $n_f \times n_c$. Details on how to construct the prolongation operator are discussed in the next subsection.

The restriction operator, \mathcal{R} , describes how to construct the coarse grid system from the fine-scale discrete equations. A discussion on how to construct the restriction operator is given later in this section. For now, we note that the restriction operator is applied to both sides of the fine-scale system Eq. (2.16), and a coarse grid system can thus be obtained with the help of Eq. (2.17):

$$\mathcal{R}\mathbf{A}\mathcal{P}\mathbf{u}^c = \mathcal{R}\mathbf{q} \quad \text{or} \quad \mathbf{A}^c\mathbf{u}^c = \mathbf{q}^c, \quad (2.18)$$

where the coarse grid matrix and right hand side vector are given by

$$\begin{aligned}\mathbf{A}^c &= \mathcal{R}\mathbf{A}\mathcal{P}, \\ \mathbf{q}^c &= \mathcal{R}\mathbf{q}.\end{aligned}\tag{2.19}$$

Since

$$\mathbf{u}^c = (\mathbf{A}^c)^{-1} \mathbf{q}^c,\tag{2.20}$$

the multiscale solution is constructed by

$$\mathbf{u}^{ms} = \mathcal{P} (\mathbf{A}^c)^{-1} \mathbf{q}^c \equiv \mathcal{P}(\mathcal{R}\mathbf{A}\mathcal{P})^{-1} \mathcal{R}\mathbf{q}.\tag{2.21}$$

Note that Eq. (2.21) is the multiscale solution obtained algebraically using two multiscale operators; hence, the method is referred to as an operator based multiscale method (OBMM). The OBMM is exact when a prolongation operator can be defined such that Eq. (2.17) is satisfied exactly. In most cases, the prolongation operator can only be defined as an approximation to Eq. (2.17), and the quality of the multiscale solution will depend on the choice of the prolongation and restriction operators.

The OBMM employs a simple algebraic framework that specifies how to perform multiscale computations for a general fine-scale system. The OBMM is independent of the specific details of the underlying grid, which means the same algebraic procedure can be used for Cartesian as well as complex unstructured grids. In contrast, the original MsFVM [Jenny et al., 2003; 2004] involves construction of an effective coarse-grid transmissibility field from the dual basis functions, which requires explicit use of the geometric grid information. Moreover, as discussed in the next section, incorporation of different physics (other than incompressible flow) for multiscale computation in the OBMM is much easier compared with the original MsFVM.

2.3.3 Prolongation Operator for Pressure

The OBMM describes a general framework, which is independent of the specific problems (flow or transport), or grids (structured or unstructured). However, the construction of a prolongation operator is both problem and grid dependent. We restrict our discussion to the flow equation and two-dimensional Cartesian grids in this chapter. In Chapter 3, we discuss the adaptive construction of prolongation operators for saturation. An algebraic and grid-independent procedure to construct the prolongation operator is presented in Chapter 4.

The multiscale prolongation operator for pressure, noted as \mathcal{P} , is defined as the mapping of the pressure from the coarse to fine scale, i.e.,

$$\mathbf{p}^f = \mathcal{P}\mathbf{p}^c, \quad (2.22)$$

where \mathbf{p}^c denotes the cell-center coarse-scale pressure. Hou and Wu [1997] proposed a set of specially constructed basis functions to relate the fine and coarse pressures. In their work, an oscillatory local boundary condition, which is obtained by solving a reduced problem on the local boundary, is used to localize the computation of the basis functions. They also applied an oversampling approach to reduce the error caused by the imposed reduced local boundary conditions. A dual coarse grid was employed by Jenny et al. [2003] to reduce the error caused by the imposed local boundary condition. The dual coarse grid offers significant advantages. It ensures a locally conservative operator on the primal coarse grid by extracting fluxes across the primal coarse blocks. Moreover, since these fluxes are located near the centers of the respective dual blocks, the influence of the imposed local boundary condition is reduced.

Fig. (2.2) shows a part of the multiscale grid of Fig. (2.1), which highlights a dual block. Following the idea of the reduced boundary conditions on the dual grid

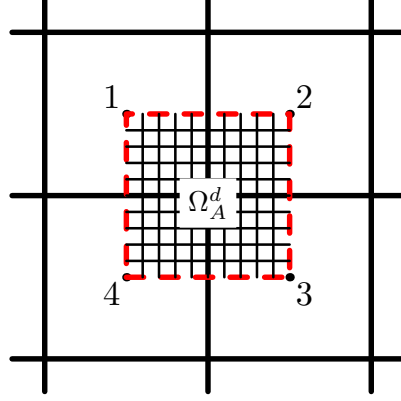


Figure 2.2: A dual block in a multiscale grid.

interfaces [Jenny et al., 2003], a basis function associated with coarse node i ($i = 1, \dots, 4$) in this dual block Ω_A^d is obtained by solving the elliptic part of Eq. (2.9),

$$\begin{cases} \sum_l \alpha_l^\nu \nabla \cdot (b_l^\nu \boldsymbol{\lambda}_l^\nu \nabla \phi_A^i) = 0 & \text{in } \Omega_A^d, \\ \sum_l \alpha_l^\nu \frac{\partial}{\partial x_t} \left(b_l^\nu \boldsymbol{\lambda}_l^\nu \frac{\partial \phi_A^i}{\partial x_t} \right) = 0 & \text{on } \partial \Omega_A^d, \\ \phi_A^i(\mathbf{x}_j) = \delta_{ij}, \end{cases} \quad (2.23)$$

where subscript t denotes the component tangential to the boundary, and j denotes any coarse node in Ω_A^d ($j = 1, \dots, 4$). Note that the basis functions in Hou and Wu [1997] and Jenny et al. [2003] are constructed for incompressible flow (i.e., $\alpha_l = 1$, $b_l = 1$), while the basis functions here are constructed for general flow problems. Particularly, the local effects of compressibility on the basis functions are reflected in Eq. (2.23). More discussion on the multiscale modeling of compressibility is in the next section.

With the basis functions, we can easily construct the prolongation operator. Let K be the global index of a coarse node, then the index of node K in dual block Ω_A^d is written as $i_{K,A}$. \mathcal{D}_K denotes the set of supporting dual blocks for node K . For a

Cartesian grid, the number of dual blocks in \mathcal{D}_K is 2^{dim} , where dim is the number of spatial dimensions. An example of a two-dimensional Cartesian grid is shown in Fig. (2.3). Using a global point of view, a basis function can be written as

$$\phi_K = \sum_{\Omega_A^d \in \mathcal{D}_K} \phi_A^{i_{K,A}}. \quad (2.24)$$

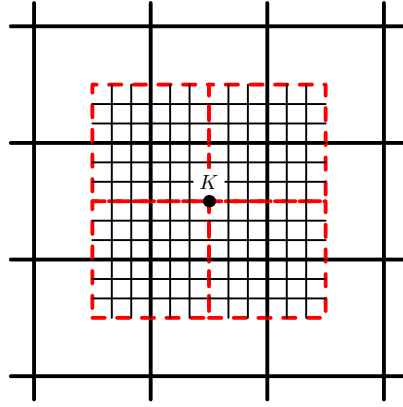


Figure 2.3: Support dual blocks (dashed lines) for primal coarse node K in a multi-scale grid

The multiscale prolongation operator, \mathcal{P} , is of dimensions $n_f \times n_c$. Let k denote a fine node and K a primal coarse node. Then one has

$$\mathcal{P}_{k,K} = \phi_K(\mathbf{x}_k). \quad (2.25)$$

Eq. (2.24) and Eq. (2.25) complete the construction of the prolongation operator with local basis functions given by Eq. (2.23).

2.3.4 Restriction Operator

The restriction operator, \mathcal{R} , defines how the coarse grid system is obtained from the discrete fine-scale equations. A natural choice is to construct the coarse-scale system

based on a discrete representation of the mass conservation equations on the coarse grid. Here, the coarse-scale equations can be directly obtained from the fine-scale equations of all the fine cells contained in a coarse cell. We denote the fine-scale mass conservation equations obtained using the finite-volume discretization by

$$E_i = 0 \quad \text{in } \Omega_i^f, i = 1, \dots, n_f. \quad (2.26)$$

The coarse-scale mass conservation equations are thus

$$\sum_{\Omega_i^f \in \Omega_K^c} E_i = 0 \quad \text{in } \Omega_K^c, k = 1, \dots, n_c. \quad (2.27)$$

Therefore, the restriction operator, which constructs Eq. (2.27) from Eq. (2.26), sums all equations in the fine cells lying in each coarse cell. This restriction operator is referred to as a finite-volume restriction operator, which satisfies

$$\mathcal{R}_{K,i} = \begin{cases} 1 & \text{if } \Omega_i^f \subset \Omega_K^c \\ 0 & \text{otherwise} \end{cases} \quad (K = 1, \dots, n_c; i = 1, \dots, n_f). \quad (2.28)$$

Note that an appealing property of the finite-volume restriction operator is that local mass conservation is satisfied on the coarse grid following Eq. (2.27).

Another choice of constructing the coarse-scale system is motivated by the Galerkin finite element method [Hughes, 1995]. Denote the linearized differential mass conservation equation by $Lu = 0$, where L denotes a linear operator and u the solution. Assume the weight function space \mathcal{V}_h is spanned by the basis functions,

$$\mathcal{V}_h = \text{span}\{\phi_K, K = 1, \dots, n_c\}. \quad (2.29)$$

The Galerkin method requires

$$\int_{\Omega_f} \phi_K Lu = 0, \quad K = 1, \dots, n_c. \quad (2.30)$$

Since ϕ_K is usually obtained as a discrete equation on the fine grid, we would calculate the integration in Eq. (2.30) by summation of piece-wise constants on the fine grid. The differential equation Lu can be approximated by finite-volume discretization on the fine grid. Thus, one can obtain a coarse-scale system from the fine-scale finite volume discretization equation as,

$$\sum_i \phi_K(x_i) E_i = 0, \quad K = 1, \dots, n_c. \quad (2.31)$$

The restriction operator that gives Eq. (2.31) is referred to as a Galerkin restriction operator and takes the form of

$$\mathcal{R} = \mathcal{P}^T. \quad (2.32)$$

We note that the mass conservation equation in a cell, E_i , can be expressed using the fine-scale system as

$$E_i = (\mathbf{A}\mathbf{u})_i \quad (2.33)$$

In the Galerkin method, the solution \mathbf{u} is also assumed to be in \mathcal{V}_h , i.e., $\mathbf{u} = \mathcal{P}\mathbf{u}_c$, with \mathcal{P} defined by Eq. (2.25). Therefore, Eq. (2.31) can also be written as

$$\mathcal{R}^T \mathbf{A} \mathcal{P} \mathbf{u}_c = 0. \quad (2.34)$$

This indicates that the solution given by Eq. (2.21) with the Galerkin restriction operator Eq. (2.32) and the prolongation operator Eq. (2.25) would be equivalent to the solution obtained by the MsFEM [Hou and Wu, 1997], if the dual grid employed here is used as the finite-element mesh, and a first-order quadrature on the fine grid

is used for performing the integration.

Note that the Galerkin restriction operator has also been used in domain decomposition methods [Smith et al., 1996; Toselli and Wildlund, 2005] to construct coarse-scale solvers. Although the Galerkin restriction operator defined by Eq. (2.32) does not ensure local mass conservation on the coarse grid, it inherits some nice property from the Galerkin method, such as the so called best approximate property whereby the Galerkin solution minimizes the energy error norm in the function space \mathcal{V}_h [Hughes, 1995].

2.4 Application of OBMM to Flow Problems

In this section, we apply the OBMM to flow problems arising from a two-phase model (Eq. (2.1)). We begin with the simplest model: incompressible flow without gravity or capillarity. Then, compressibility, gravity and capillary are in turn added into consideration.

It is worth noting that so far, only the multiscale finite-volume method has been applied to a general black-oil model [Lee et al., 2008]. The local mass conservation of the multiscale finite-volume formulation is an essential ingredient for solving coupled nonlinear flow and transport problems in the presence of complex physics. Therefore, although the OBMM can represent both multiscale finite-volume and finite-element formulations in solving general flow problems, we focus on the multiscale finite-volume formulation, i.e., only the finite-volume restriction operator is considered.

2.4.1 Simple Flow Model

We first consider the flow problem in a heterogeneous medium without compressibility, gravity or capillary pressure. The discrete pressure equation, Eq. (2.9), is reduced to this simple flow model when $b_{o,w} = 1$, $\partial\phi/\partial p = 0$, $p_c = 0$, and $g = 0$ or $\nabla z = 0$, which

Figure 2.4: 1D multiscale grid.

central-difference scheme for the fine-scale discretization, the OBMM algorithm gives three non-zeros elements for the K^{th} row of the coarse-scale transmissibility matrix,

i.e.,

$$\begin{aligned}
A_{K,K-1}^c &= -\frac{\lambda_{T^{k-3/2}}}{\Delta x} (\phi_{K-1}(x_{k-1}) - \phi_{K-1}(x_{k-2})), \\
A_{K,K}^c &= -\frac{\lambda_{T^{k-3/2}}}{\Delta x} (\phi_K(x_{k-1}) - \phi_K(x_{k-2})) \\
&\quad + \frac{\lambda_{T^{k+3/2}}}{\Delta x} (\phi_K(x_{k+2}) - \phi_{K-1}(x_{k+1})), \\
A_{K,K+1}^c &= -\frac{\lambda_{T^{k+3/2}}}{\Delta x} (\phi_{K+1}(x_{k+2}) - \phi_{K+1}(x_{k+1})).
\end{aligned} \tag{2.37}$$

$A_{K,K-1}^c$ is the flux across the interface between coarse blocks $K-1$ and K with respect to application of unit-pressure at node $K-1$, which is also how the coarse-scale effective transmissibility is defined in Jenny et al. [2003; 2004].

When the geometry of the fine and multiscale grids gets more complicated, i.e. in three-dimensional problems, the OBMM algorithm is much more straightforward to implement than the original multiscale finite-volume method. This implementation advantage will be even more significant for unstructured grids. We note that there is some overhead in constructing the coarse-scale matrix from $\mathbf{A}^c = \mathcal{R}\mathbf{A}\mathcal{P}$ compared with using the effective coarse-scale transmissibility. This is because the computation of $\mathcal{R}\mathbf{A}\mathcal{P}$ involves some interior flux integration in the primal coarse block, which cancel out for this elliptic problem, while in the MsFVM only fluxes on interfaces of the primal coarse grid are considered. However, this extra computational cost is negligible, and state-of-the-art linear algebraic libraries are quite efficient in sparse matrix multiplication. Moreover, the general flow equation, Eq. (2.8), is not in a conservative form due to compressibility, and it is necessary to calculate the interior fluxes in order to accurately account for compressibility. More discussion is in the next subsection.

2.4.2 Extension to Compressibility

When compressibility is included in black-oil models, the formation volume factors (i.e., $1/b_l$) of the fluids and the porosity of the formation are functions of pressure. For compressible systems, Eq. (2.9) is a parabolic equation. The extension of OBMM to compressible flow is very natural without any need for special modifications. The basis functions are computed according to Eq. (2.23), which takes into account the influence of compressibility on the local pressure distribution. The coarse-scale system contains contributions of compressibility to both the convection and accumulation terms.

To illustrate how OBMM incorporates the compressibility effect on the coarse scale, we first decompose the fine-scale matrix \mathbf{A} into an accumulation part and a convection part as follows

$$\mathbf{A} = \mathbf{C} - \mathbf{T}, \quad (2.38)$$

where \mathbf{C} is an accumulation matrix and \mathbf{T} is the convection matrix. The coarse-scale matrices are accordingly defined:

$$\mathbf{A}^c = \mathbf{C}^c - \mathbf{T}^c = \mathcal{R}\mathbf{C}\mathcal{P} - \mathcal{R}\mathbf{T}\mathcal{P}, \quad (2.39)$$

where \mathbf{C}^c and \mathbf{T}^c are the coarse-scale accumulation and convection matrices, respectively.

The fine-scale fluxes represented by \mathbf{T} contain compressibility effects. With the finite-volume restriction operator, \mathbf{T}^c is equivalent to the coarse-scale fluxes obtained by summing up the fine-scale fluxes calculated from basis functions in each coarse block. In the presence of compressibility, the interior fluxes in the primal coarse blocks do not cancel out, and the contribution of compressibility from every fine cell is added to the coarse-scale convection matrix, \mathbf{T}^c . Similarly, the coarse-scale accumulation matrix, \mathbf{C}^c , distributes the underlying fine-scale accumulation to the coarse cell itself

and its neighbors according to the basis functions. The effect of compressibility is thus also reflected in the accumulation matrix. Moreover, the finite-volume restriction operator guarantees mass conservation on the coarse scale. Note that both \mathbf{T}^c and \mathbf{C}^c have 3^{dim} (dim denotes dimension, $dim = 1, 2, 3$) number of non-zeros in each row (i.e., the same pattern as the convection matrix in multipoint flux approximation, c.f. Aavatsmark [2002]).

Note that in the MsFVM [Jenny et al., 2003; 2004], when more physics needs to be included, special treatment is necessary to formulate a new coarse-scale system, which was what Lunati and Jenny [2006] did to extend the original MsFVM to compressible flow. In their discrete formulation, they assumed that the coarse-scale accumulation matrix is diagonal (i.e., contribution to the coarse-scale accumulation for a coarse block is only from the block itself), and they proposed three models to compute that contribution. In their most accurate model (FSA, referring to Fine Scale Accumulation), the accumulation term is calculated on the fine scale from the dual pressure. As we have shown, in the MsFVM construction the dual pressure in one primal coarse block depends on the coarse-scale pressure in all of the neighboring coarse blocks. Consequently, to accurately compute the coarse-scale accumulation from the fine-scale dual pressure, one should have a multi-diagonal (3^{dim}) matrix instead of a diagonal one. Lunati and Jenny [2006] imposed additional constraints to get a diagonal accumulation matrix from FSA. In the OBMM, on the other hand, there is no assumption on the form of the coarse-scale system. If we choose to compute coarse-scale accumulation from the fine-scale dual pressure, we naturally obtain a 3^{dim} -diagonal accumulation matrix, which is a more accurate representation.

In addition, due to difficulties in eliminating saturation from the coarse-scale equations, the derived coarse-scale pressure system by Lunati and Jenny [2006] has dependency on saturation, which may introduce some numerical difficulties in multiphase flow problems. In the OBMM, one can easily eliminate saturation from the pressure

equation on the fine scale, and then the construction of the coarse-scale pressure system is independent of saturation as shown in Eq. (2.9).

2.4.3 Extension to Gravity and Capillary Pressure

Extension of MsFVM to multiphase flow under gravity was first performed by Lunati and Jenny [2008]. Lee et al. [2008] included both gravity and capillary pressure for multiscale computations of three-phase flow and transport. The idea there is to employ local fine-scale correction functions to account for the effects of gravity and capillary pressure. Note that gravity and capillary pressure contribute only to the right hand side of the pressure discretization equation, Eq. (2.9). Therefore, the correction functions are solutions to inhomogeneous elliptic problems defined on dual blocks, specifically,

$$\begin{cases} \sum_l \alpha_l \nabla \cdot (b_l \lambda_l \nabla \phi_A^*) = R^* & \text{in } \Omega_A^d, \\ \sum_l \alpha_l \nabla_t \cdot (b_l \lambda_l \nabla_t \phi_A^*) = R_t^* & \text{on } \partial \Omega_A^d, \\ \phi_A^i(\mathbf{x}_j) = 0, \end{cases} \quad (2.40)$$

where ϕ_A^* is the correction function defined on dual coarse cell Ω_A^d and the right hand side terms, R^* and R_t^* are given by

$$\begin{aligned} R^* &= - \sum_{l=o,w} \alpha_l \nabla \cdot (\rho_l g \boldsymbol{\lambda}_l \cdot \nabla z) - \alpha_w^{\nu_p} \nabla \cdot (b_w^{\nu_p} \boldsymbol{\lambda}_w \nabla p_c), \\ R_t^* &= - \sum_{l=o,w} \alpha_l \nabla_t \cdot (\rho_l g \boldsymbol{\lambda}_l \cdot \nabla_t z) - \alpha_w^{\nu_p} \nabla_t \cdot (b_w^{\nu_p} \boldsymbol{\lambda}_w \nabla_t p_c). \end{aligned} \quad (2.41)$$

Note that the same reduced boundary condition for the basis functions is used for the correction functions, and the correction functions are zeros on the vertices of dual coarse cells. One correction function is defined for each dual coarse block. The

fine-scale solution is then expressed as

$$p(x) = \sum_i \phi_A^i p_i^c + \phi_A^* \quad (x \in \Omega_A^d). \quad (2.42)$$

The idea of correction functions can be included in the OBMM by defining a correction vector \mathbf{p}^{corr} :

$$\mathbf{p}_i^{corr} = \phi_A^*(x_i) \quad (x_i \in \Omega_A^d). \quad (2.43)$$

Then, the fine-scale pressure vector can be expressed by the prolongation operator and the correction vector as

$$\mathbf{p}^f = \mathcal{P}\mathbf{p}^c + \mathbf{p}^{corr}. \quad (2.44)$$

Consequently, the coarse-scale system obtained through the OBMM is

$$\mathcal{R}\mathbf{A}\mathcal{P}\mathbf{p}^c = \mathcal{R}\mathbf{q} - \mathcal{R}\mathbf{A}\mathbf{p}^{corr} \equiv \tilde{\mathbf{q}}^c, \quad (2.45)$$

or

$$\mathbf{A}^c \mathbf{p}^c = \tilde{\mathbf{q}}^c. \quad (2.46)$$

So in order to incorporate gravity and capillary pressure in the OBMM, we simply replace the coarse-scale right hand side, $\mathcal{R}\mathbf{q}$, by $\mathcal{R}\mathbf{q} - \mathcal{R}\mathbf{A}\mathbf{p}^{corr}$.

2.5 Fine-scale Velocity and Saturation

The focus of this chapter is on the general algebraic multiscale framework for the flow problem (i.e., solving for pressure and total-velocity), and the multiscale modeling of transport is deferred until the next chapter. In this section, we reconstruct a locally conservative fine-scale velocity field and then solve the transport equations on the fine scale.

2.5.1 Fine-Scale Velocity Reconstruction

The fine-scale pressure obtained from OBMM can be written as

$$\mathbf{p}^d = \mathcal{P}(\mathbf{A}^c)^{-1} \tilde{\mathbf{q}}^c + \mathbf{p}^{corr}, \quad (2.47)$$

which is also referred to as the dual (fine-scale) pressure since it is reconstructed using the basis and correction functions that are defined on the dual coarse blocks. However, the fine-scale velocity calculated directly from \mathbf{p}^d may be discontinuous across the interfaces of the dual coarse blocks. This problem is the consequence of ensuring flux continuity only on the boundaries of the primal coarse blocks when computing the basis and correction functions.

To obtain a conservative fine-scale velocity field, we solve the fine-scale system, Eq. (2.9), locally for each primal coarse block with flux boundary conditions. The flux boundary conditions, as well as the pressure dependent coefficients are all obtained using \mathbf{p}^d , i.e., $p^\nu = p^d$ in the following equation:

$$\left\{ \begin{array}{ll} C \frac{p^p - p^\nu}{\Delta t} - \sum_l \alpha_l^\nu \nabla \cdot (b_l^\nu \boldsymbol{\lambda}_l^\nu \nabla p^p) = R, & \text{in } \Omega_A^c, \\ \frac{\partial p^p}{\partial n} = \frac{\partial p^\nu}{\partial n}, & \text{on } \partial\Omega_A^c. \end{array} \right. \quad (2.48)$$

Here, the fine-scale pressure computed in this manner is referred to as the primal fine-scale pressure and is denoted by \mathbf{p}^p .

Then, the fine-scale velocity in the interior of primal coarse blocks is calculated from \mathbf{p}^p , while the velocity on the boundary of a primal coarse block is calculated from \mathbf{p}^d . In this way, the computed fine-scale velocity is conservative everywhere. Also note that additional physical mechanisms (e.g., compressibility, gravity, and capillary pressure) are easy to take into account using this fine-scale velocity reconstruction process, according to Eq. (2.48).

2.5.2 Fine-scale Saturation Computation

We choose the sequential fully implicit (SFI) algorithm to solve the coupled flow and transport equations. For each timestep, in an outer loop we solve for the fine-scale pressure using the OBMM and calculate the fine-scale total velocity, \mathbf{u}_t ; in an inner loop we solve for the fine-scale saturation implicitly according to Eq. (2.12). The pseudo code for one timestep is listed in Fig. (2.5), where the superscripts n and ν denotes a timestep and iteration level, respectively.

Note that for the finite-volume based OBMM, the restriction operator needs to be constructed only once. Also note that when solving the saturation equations in the inner loops, the total velocity \mathbf{u}_t is fixed, i.e., \mathbf{u}_t is only updated once in each outer loop.

The step of solving linearized transport equations can be performed using a conventional finite-volume solution procedure. A one-level additive Schwarz method (ASM) with overlap only on boundary fluxes is used here to solve the transport system. This strategy has been adopted by Jenny et al. [2004] and Lee et al. [2008]. In this approach, the primal coarse blocks are a natural choice of the ASM blocks. Then, the transport problems are solved locally on each primal coarse block with boundary fluxes from the previous iteration. The procedure is iterated until convergence of the computed saturation field is achieved.

2.6 Computational Aspects of OBMM for Flow

2.6.1 Adaptive Computation

The efficiency of OBMM can be greatly improved if the basis and correction functions are updated infrequently. Jenny et al. [2004; 2006] proposed adaptive updating of the basis functions according to the time-change of total mobility. However, as can be


```

 $\nu_p = 1; \nu_s = 1; p^{\nu_p} = p^n; S^{\nu_s} = S^n$ 
/* outer loop */
while ( pressure equation not converged)
    calculate fine-scale operators;
    update basis and correction functions if necessary;
    assemble prolongation operator;
    calculate coarse-scale operators;
    solve for coarse-scale pressure,  $\mathbf{p}^c$ ;
    reconstruct dual fine-scale pressure,  $\mathbf{p}^d$ ;
    reconstruct primal fine-scale pressure,  $\mathbf{p}^p$ ;
     $\nu_p = \nu_p + 1; p^{\nu_p} = p^d$ ;
    update pressure dependent properties:  $b = b(p^{\nu_p})$ ;
    calculate fine-scale total velocity  $\mathbf{u}_t$  from  $\mathbf{p}^d$  and  $\mathbf{p}^p$ ;
/* inner loop */
    while (saturation equation not converged)
        solve linearized transport equation for  $S^{\nu_s+1}$ ;
         $\nu_s = \nu_s + 1$ ;
        update saturation dependent properties:
         $\Rightarrow \lambda = \lambda(S^{\nu_s})$ ;
    end
end
 $n = n + 1$ 

```

Figure 2.5: The pseudo code of OBMM with SFI scheme for one timestep.

seen from Eq. (2.23), the basis functions rely on the mobility (a function of saturation) and the pressure in general flow problems. Here we extend the adaptive computation of the basis and correction functions to general flow problems.

The adaptive updating of basis functions is performed as follows. If the condition

$$\frac{1}{1 + \epsilon_\lambda} < \frac{(\sum_l b_l \lambda_l)^\nu}{(\sum_l b_l \lambda_l)^*} < 1 + \epsilon_\lambda \quad (2.49)$$

is not satisfied for all fine cells inside a dual coarse block, the basis functions associated with that dual block should be recomputed. The superscript * here denotes the state from the last basis function update. Note that Eq. (2.49) does not contain the absolute permeability which is usually static. The parameter ϵ_λ is a user defined adaptivity threshold. The optimum value is problem dependent. Usually, $0.1 \leq \epsilon_\lambda \leq 0.5$ yields results that are in close agreement with reference fine-scale solutions and $0.5 \leq \epsilon_\lambda \leq 1$ requires even less updating, but our experience indicates that it gives reasonable accuracy for a wide range of problems. For difficult cases such as gravity segregation, where having accurate pressure is crucial, a small ϵ_λ is recommended (e.g., 0.1). Otherwise, $\epsilon_\lambda = 0.5$ is a good choice in most cases.

The adaptive computation of correction functions is controlled by Eq. (2.49) together with criteria on the change of gravity and capillary pressure terms, i.e.,

$$\frac{1}{1 + \epsilon_g} < \frac{(\sum_l \rho_l \lambda_l)^\nu}{(\sum_l \rho_l \lambda_l)^*} < 1 + \epsilon_g \quad \text{and} \quad \frac{1}{1 + \epsilon_{pc}} < \frac{(b_w \lambda_w p_c)^\nu}{(b_w \lambda_w p_c)^*} < 1 + \epsilon_{pc}, \quad (2.50)$$

which are in a similar form with Eq. (2.49). The suggested values of ϵ_g and ϵ_{pc} are in the same range as ϵ_λ .

To avoid inconsistency, both basis and correction functions should be updated whenever either one requires updating. That is, violation of either Eq. (2.49) or Eq. (2.50) triggers updating of both basis and correction functions. This strategy ensures the coefficients in Eq. (2.23) and Eq. (2.40) are the same and that the basis

and correction functions are consistent with each other.

2.6.2 Computational Complexity

We now present a brief discussion of the computational complexity of OBMM for the flow problem. The complexity is compared with a fine-scale method. A basic assumption in the complexity analysis is that the computational effort is determined by the effort to solve the linear systems. Such an assumption is reasonable since for large-scale problems, which are the target of OBMM, solving the linear system is the dominant factor in computational cost.

Assume that the time to solve a linear system of size $n \times n$ for the flow problem is given by

$$t_p(n) = \mathcal{O}(n^\alpha). \quad (2.51)$$

Then, the computational complexity for the fine-scale method is

$$t_f = t_p(n_f) = \mathcal{O}(n_f^\alpha). \quad (2.52)$$

The computational time of OBMM can be divided into three parts: construction of the prolongation operator, solving the coarse-scale system, and reconstruction of the conservative fine-scale velocity field. For the construction of the prolongation operator, solutions for the basis and correction functions take the most time, and this is expressed as

$$t_1 = f_p(2^D + 1)n_c t_p(Cr), \quad (2.53)$$

where f_p is the fraction of dual cells in which the basis and correction function need to be recomputed, D is the number of dimensions of the problem ($D = 1, 2, 3$), and C_r is the coarsening ratio defined in Eq. (2.15). The computational time for solving

the coarse-scale system is

$$t_2 = t_p(n_c). \quad (2.54)$$

Finally, the computational complexity of reconstructing the conservative fine-scale velocity is

$$t_3 = n_c t_p(Cr). \quad (2.55)$$

The overall computational time of OBMM is thus

$$t_{ms} = t_1 + t_2 + t_3 = [1 + f_p(2^D + 1)] n_c t_p(Cr) + t_p(n_c) \quad (2.56)$$

We can compute an optimal n_c that minimizes the computational time of OBMM, Eq. (2.56), i.e.,

$$\frac{dt_{ms}}{dn_c} = 0 \Rightarrow n_c = \left[\frac{1 + f_p(2^D + 1)}{\alpha/(\alpha - 1)} \right]^{1/(2\alpha-1)} n_f^{\alpha/(2\alpha-1)} \quad (2.57)$$

In realistic problems, $\alpha = 1.5$ for large-scale linear systems is commonly observed, and it is reasonable to suggest $f_p = 0.2$ for standard multiphase flow problems as shown in the numerical results by the end of this chapter. Hence, an optimal coarse-grid size based on computational complexity analysis is given by

$$n_c|_{opt} \approx \begin{cases} 0.8n_f^{2/3} & \text{for 2-D} \\ n_f^{2/3} & \text{for 3-D} \end{cases}. \quad (2.58)$$

We now take a model problem with a fine grid of $512 \times 512 \times 512$. Fig. (2.6) shows the expected speedup of OBMM over the fine-scale method for different coarse grids and updating ratios (f_p) with $\alpha = 1.5$ and $\alpha = 1.2$. An $\alpha = 1.2$ has been reported for the algebraic multigrid method (AMG) [Stüben, 2000], which is the most efficient solver for scalar elliptic problems on unstructured grids. For $\alpha = 1.5$, the multiscale

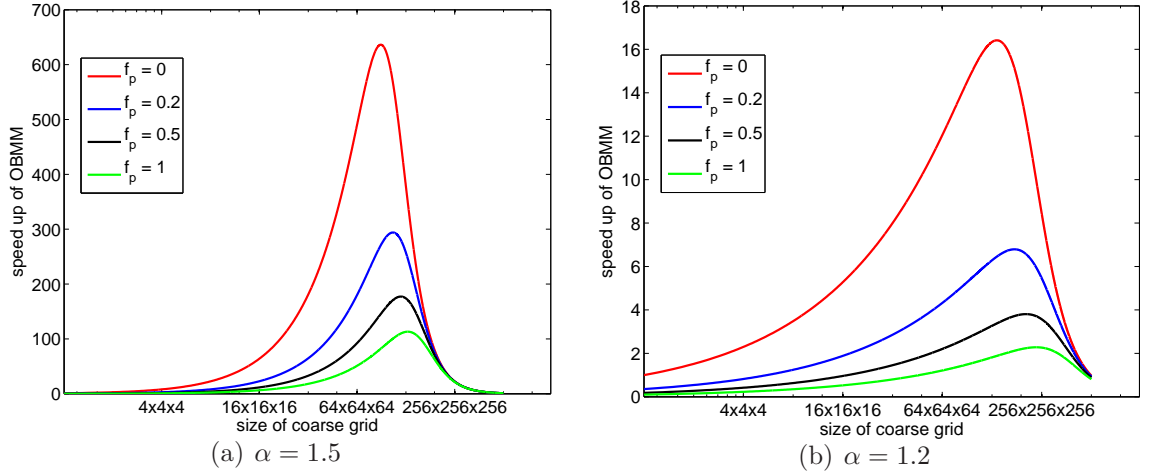


Figure 2.6: Speedup of OBMM for flow problem

method is about two orders of magnitude more efficient than the fine-scale method assuming that an appropriate coarse grid is used. Compared with the state-of-the-art linear solver for elliptic problems, where $\alpha = 1.2$, the multiscale method is still more efficient. We also observe from Fig. (2.6) that the adaptive computations of the correction and basis functions are important to achieve better efficiency in OBMM. A 20% updating of the basis and correction functions yields more than three times speedup over updating all the basis and correction functions.

2.7 OBMM for Complex Physics

We test the accuracy of OBMM by a series of numerical examples. First, we study the multiscale modeling of compressible flow by OBMM. A comparison with the approach of Lunati and Jenny [2006] is made for a one-dimensional (1D) problem. A challenging gas depletion problem in a highly heterogeneous, two-dimensional (2D) permeability field is also presented to further validate the method. As can be seen from Eq. (2.9), gravity and capillary pressure play quite similar roles in the flow equations. Moreover,

the effect of capillary pressure is usually small compared with gravity in practical large-scale reservoir simulations. Thus, we focus on the gravity effect only. A vertical gravity segregation problem in a homogeneous permeability field is first investigated, and then a 2D buoyancy-driven flow problem in a heterogeneous permeability field is studied.

2.7.1 1D Single-Phase Compressible Flow

First, we consider a simple 1D single-phase gas flow in a homogeneous permeability field. The purpose is to examine the accuracy of OBMM for compressible problems. A numerical comparison between the OBMM and the FSA model proposed by Lunati and Jenny [2006] is presented here. We have compared the OBMM and the FSA model in terms of methodology in subsection 2.4.2.

The fluid is taken to be ideal gas, and thus the PVT relation is simply

$$b = \frac{p}{p_0}, \quad (2.59)$$

where p_0 is the pressure at standard conditions. The fine grid contains 100 cells and the coarse grid has five cells. The permeability is assumed to be constant. The initial pressure is constant at 1 atm. The left and right boundaries are kept at constant pressures of 10 and 1 atm, respectively. We define a dimensionless characteristic time τ as

$$\tau = \frac{\mu \phi L^2}{k(p_l - p_r)}. \quad (2.60)$$

We compare the pressure results of the OBMM with those of the FSA model, as well as the fine-scale reference solutions. Note that in the FSA model, we use the basis functions used by Lunati and Jenny [2006], which only depend on the total mobility. The basis functions in the OBMM are computed from Eq. (2.23).

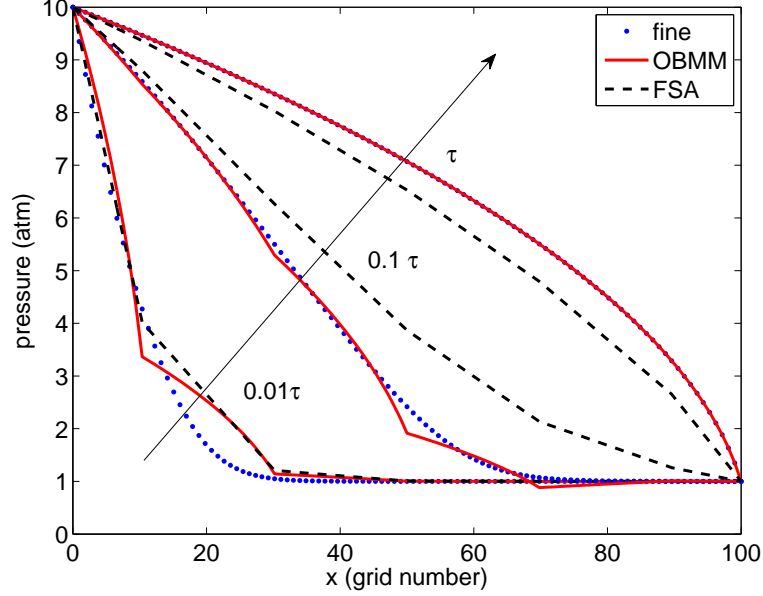


Figure 2.7: Comparison of pressure results of OBMM, FSA, and fine-scale reference solution for 1D single-phase gas flow at three times.

As can be seen in Fig. (2.7), the OBMM shows some error at early time, which is mainly due to the fact that the elliptic basis functions do not capture the fine-scale pressure distribution in the early transient period. The OBMM quickly approaches the fine-scale reference solution at later time. At $t = \tau$, the results are the same as the fine-scale solution. On the other hand, the FSA model shows somewhat larger errors at later time, which are mainly due to two reasons. One is the diagonal approximation of the coarse-scale accumulation; the other is due to computing the basis functions without dependency on pressure (or b), which gives linear basis functions in this homogeneous single-phase problem.

2.7.2 2D Two-Phase Compressible Flow

We now study 2D two-phase flow. The permeability field is extracted from the top layer of the SPE 10 model [Christie and Blunt, 2001], which is highly heterogeneous

as shown in Fig. (2.8). The variance of log-permeability of this model is $\sigma_{lnk}^2 = 5.45$. The fine-scale grid contains 220×60 cells, and the coarse-scale grid contains 20×6 blocks. The coarsening ratio (upscaling factor) is 110 (11×10).

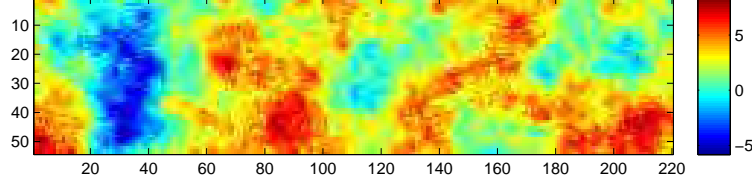


Figure 2.8: Log-permeability of the top layer of the SPE 10 model.

We study a depletion oil-gas problem. The PVT properties are represented by formation volume factors as

$$\begin{aligned} b_g &= \frac{p}{p_0}, \\ b_o &= 1 + 10^{-3}(p - p_0). \end{aligned} \tag{2.61}$$

Quadratic relative permeability curves are used. The viscosities of the two phases are $\mu_g = 1.8 \times 10^{-2}$ cp, $\mu_o = 1$ cp. The porosity is constant at 0.1. The field has an initial oil saturation of 0.5 and an initial pressure of 147 psi. The left boundary is kept at a constant pressure of 147 psi with $S_o = 0.5$, while the right boundary is brought to a constant pressure of 14.7 psi. Due to the pressure drop and compressibility differences, the gas expands much more than the oil, which causes significant changes in the field.

In Fig. (2.9 – 2.14), we show a comparison of the OBMM solution with the reference fine-scale solution for the pressure and saturation fields at three times: $5 \times 10^{-3}\tau$, 0.2τ and τ , where the dimensionless characteristic time is defined by

$$\tau = \frac{\mu_o \phi L_x^2}{k(p_l - p_r)}. \tag{2.62}$$

Here \bar{k} is the median permeability, which is 17.8 millidarcy (mD). The timestep is $5 \times 10^{-3}\tau$ for the first 10 timesteps and kept constant at 0.01τ thereafter. The adaptivity threshold ϵ in Eq. (2.49) is 0.2.

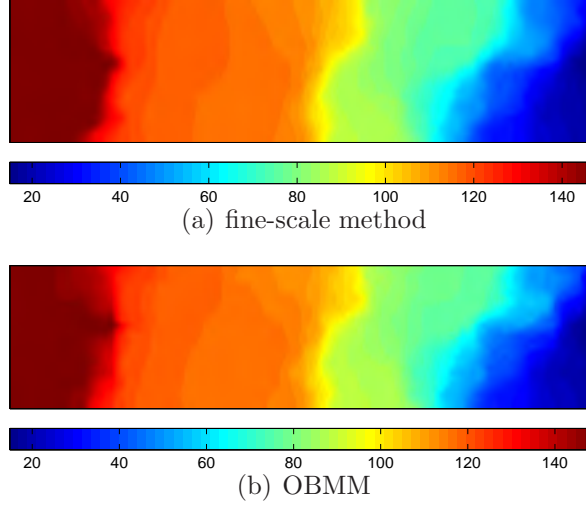


Figure 2.9: Fine-scale pressure at $t = 5 \times 10^{-3}\tau$: (a) using fine-scale method; (b) using OBMM.

As shown in Fig. (2.9 – 2.14), for the various times, good agreement between OBMM and the fine-scale reference solutions is observed.

We also report in Table (2.7.2), the error statistics and the cumulative percentage of basis functions that are recomputed. The pressure error, e_p , and the saturation error, e_s , are defined as

$$\begin{aligned} e_p &= \frac{\|p^{ms} - p^f\|_2}{\|p^f\|_2}, \\ e_s &= \|S^{ms} - S^f\|_2, \end{aligned} \tag{2.63}$$

where superscripts f and ms , denote, respectively, the reference and OBMM solutions. The cumulative percentage of basis function updating, f_p , is the total number of updating basis functions from time zero to the current time divided by the total number without adaptivity.

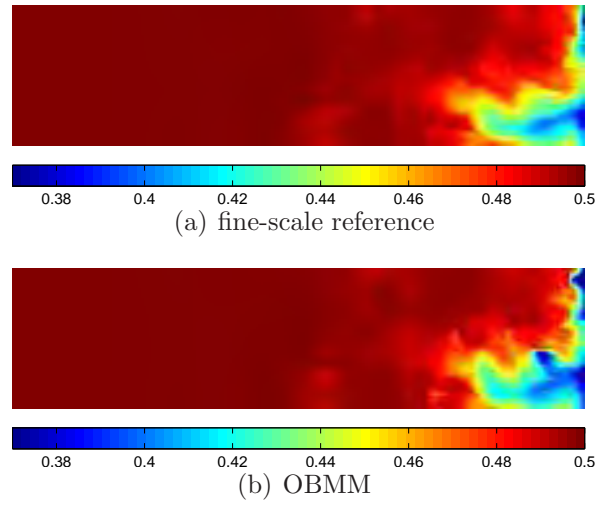


Figure 2.10: Fine-scale oil saturation at $t = 5 \times 10^{-3}\tau$: (a) using fine-scale method; (b) using OBMM.

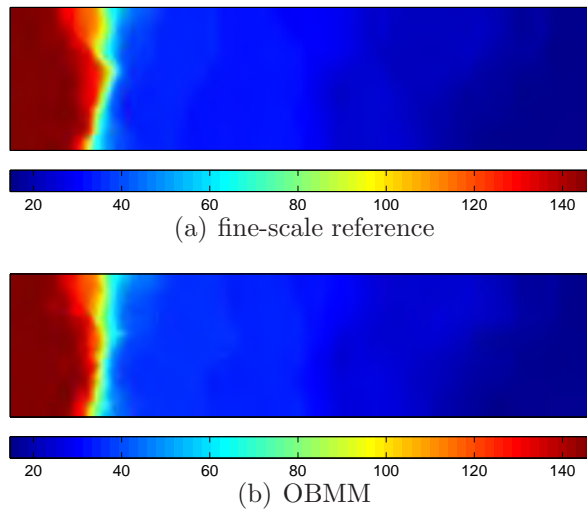


Figure 2.11: Fine-scale pressure at $t = 0.2\tau$: (a) using fine-scale method; (b) using OBMM.

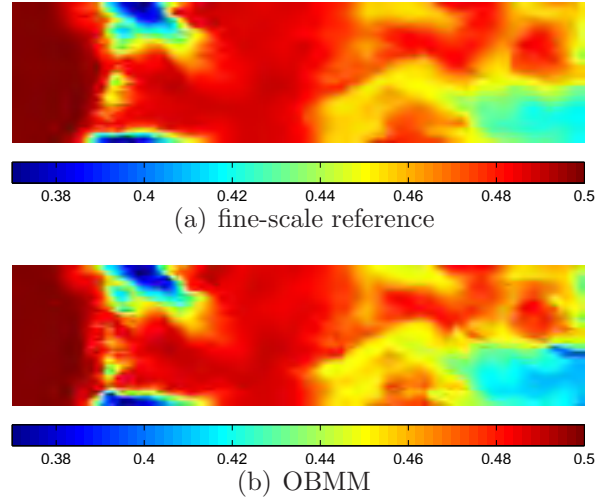


Figure 2.12: Fine-scale oil saturation at $t = 0.2\tau$: (a) using fine-scale method; (b) using OBMM.

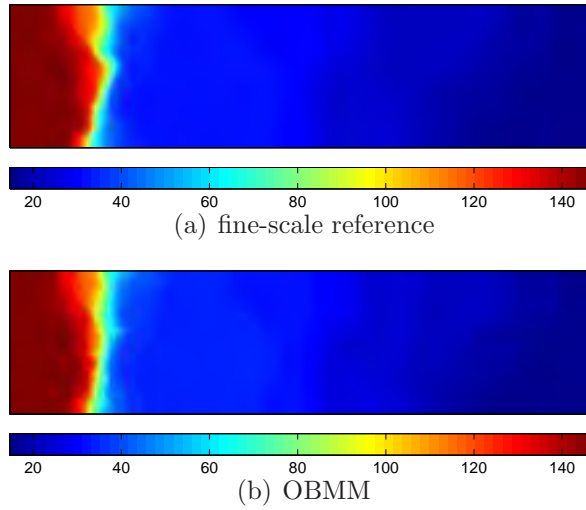


Figure 2.13: Fine-scale pressure at $t = 1\tau$: (a) using fine-scale method; (b) using OBMM.

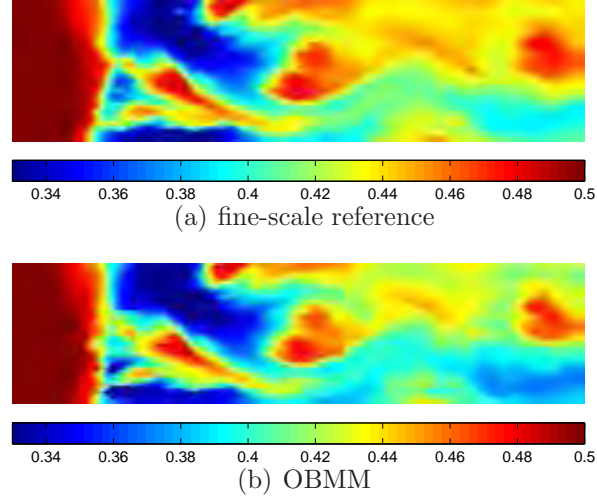


Figure 2.14: Fine-scale oil saturation at $t = 1\tau$: (a) using fine-scale method; (b) using OBMM.

t (PVI)	e_p	e_s	$f_p(\%)$
5e-3	1.13e-2	5.32e-5	12.22
0.2	1.80e-2	6.32e-5	7.96
0.8	1.64e-2	1.13e-4	8.79
1	1.62e-2	1.23e-4	7.98
1.5	1.64e-2	1.36e-4	6.50

Table 2.1: Errors and percentage of the recomputed basis functions at several timesteps for the compressible flow in SPE10 top layer

2.7.3 Gravity Segregation

Gravity segregation is an important flow problem of practical interest. It is also a challenging problem for numerical simulation as it involves strong counter-current flow of fluids. We study vertical segregation here, which happens in practical reservoir engineering when rapid displacement causes an unstable vertical arrangement of fluids with water on top of oil in communicating layers. We thus consider a model problem as shown in Fig. (2.15). A characteristic time scale for the vertical segregation is defined by

$$\tau = \frac{\phi\mu_o H}{g(\rho_w - \rho_o)k}. \quad (2.64)$$

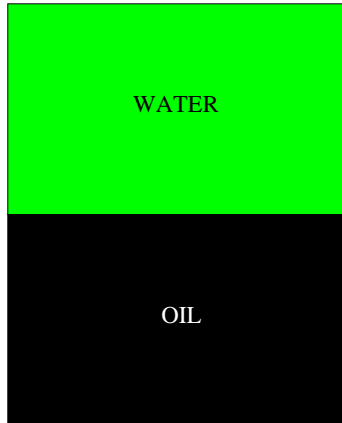


Figure 2.15: Vertical segregation problem

We start with a homogeneous reservoir, where the flow takes place in the vertical direction only. Although vertical segregation in a homogeneous reservoir is actually a 1D flow problem, in order to test our multiscale code, we model this problem in 2D. We take a fine grid of 9×90 and a coarse grid of 3×10 . Quadratic relative permeability relationships are used, and the viscosity of both water and oil is taken to be 1 cp.

The multiscale solutions of pressure and saturation at $t = 1\tau$ are shown in

Fig. (2.16), which clearly shows the one-dimensional nature of the flow. The saturation distribution is of more interest. Thus, we compare the saturation obtained using the multiscale solution strategy with the reference fine-scale solution in the vertical direction as shown in Fig. (2.17). The figure indicates that the multiscale and fine-scale solutions are particularly on top of each other. The saturation error is $\epsilon_s = 0.03\%$. The reason the multiscale solution is so accurate is due to the one-dimensional flow of this problem, where the reduced boundary condition is exact. However, due to the use of adaptive computation, the multiscale solution is not exactly the same as the fine-scale solution. In our runs, we take the adaptivity thresholds as $\epsilon_\lambda = 0.1$, $\epsilon_g = 0.1$, which results in an overall 11.2% updating of the basis and correction functions. Note that the use of correction functions is crucial to achieve an accurate pressure distribution, which is a prerequisite for a high-quality saturation result. It is also interesting to notice there are two waves traveling in the vertical direction (Fig. (2.17)), which is a characteristic feature of the gravity segregation problem.

Now we study a more complicated two-dimensional segregation problem by considering vertical segregation (Fig. (2.15)) in a heterogeneous reservoir. The permeability field is log-normally distributed. The natural logarithm of permeability has a mean value of 4, a variance of 2, and the dimensionless spatial correlation length is 0.2. The permeability is generated by the sequential Gaussian simulation method [Deutsch and Journel, 1998] and the resulting permeability field is depicted in Fig. (2.18). The fine-scale grid, 70×70 , is uniformly coarsened into a coarse-scale grid of 10×10 .

In Fig. (2.19), we compare the contour plots of the multiscale pressure and saturation field with those from reference fine-scale solutions at several times. It is clear that the multiscale and reference fine-scale pressure solutions are quite close. The saturation fields obtained from the multiscale and reference fine-scale computations are also quite close. The saturation differences are localized around the saturation

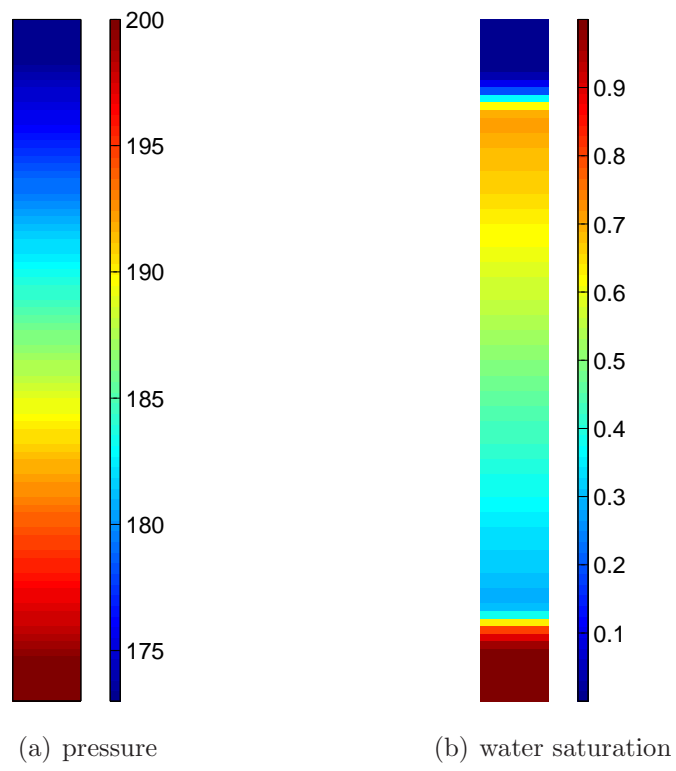


Figure 2.16: Multiscale solution for the vertical segregation in homogeneous reservoir at $t = 1\tau$

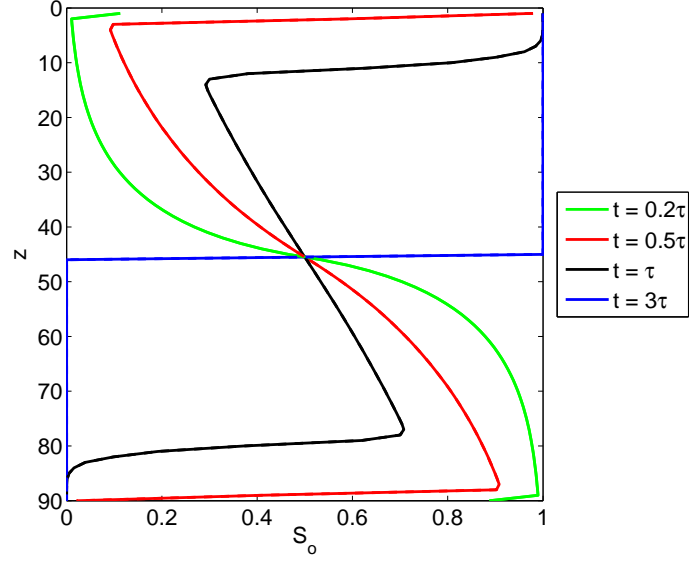


Figure 2.17: The multiscale saturation and the reference fine-scale saturation are identical for the vertical segregation in a homogeneous reservoir.

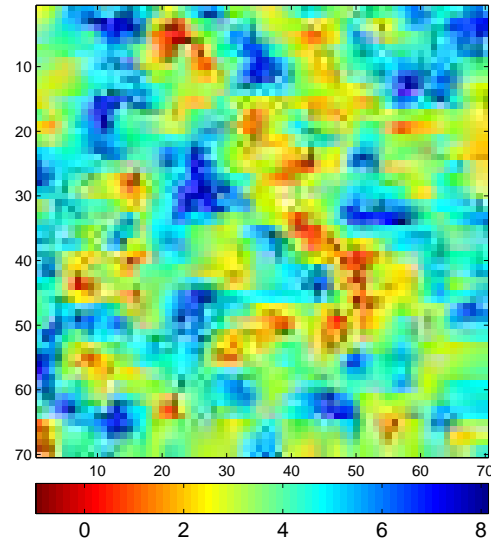


Figure 2.18: Log-normal permeability field

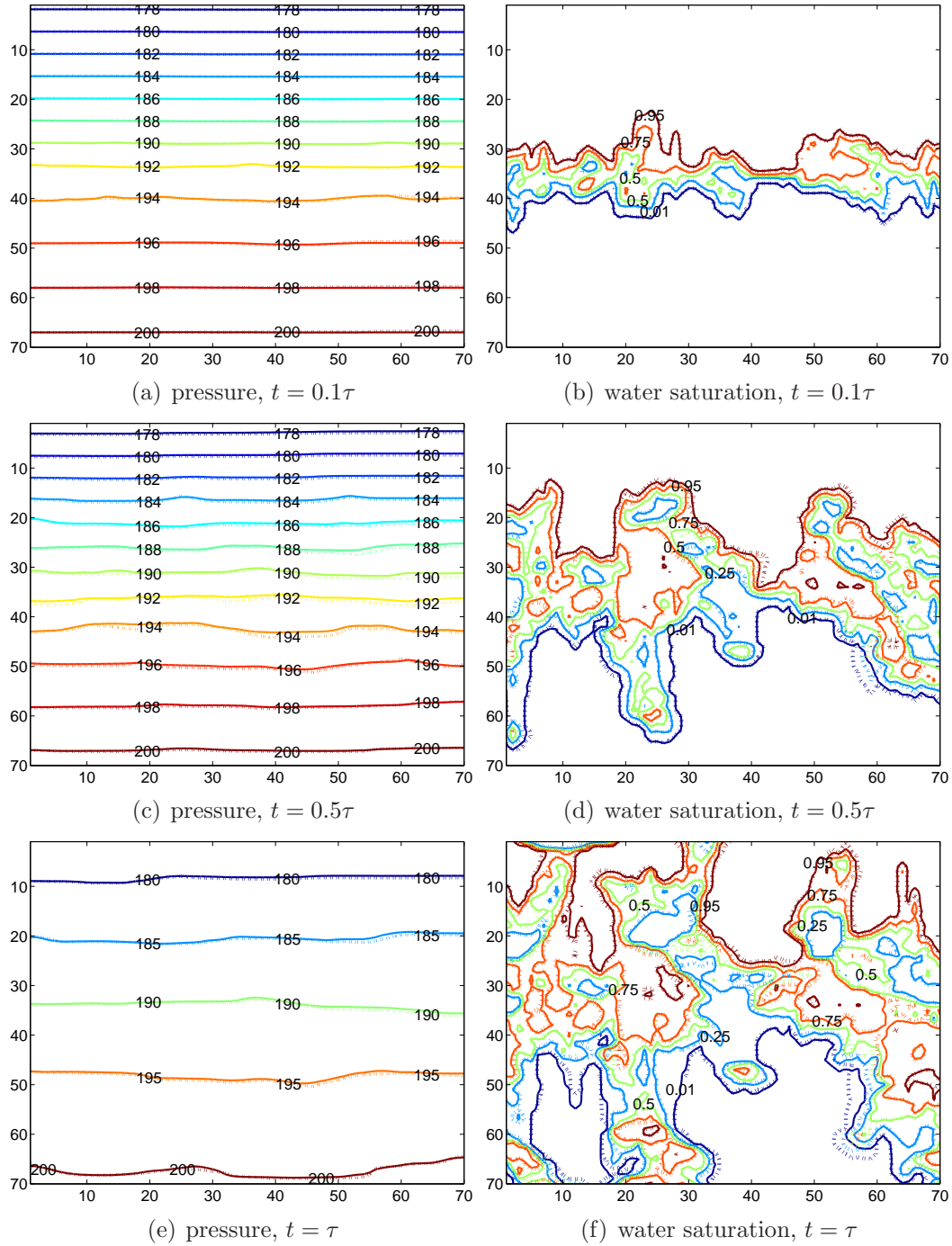


Figure 2.19: Comparison of the multiscale solutions of pressure and saturation with the fine-scale reference for the vertical segregation in a heterogeneous reservoir: solid lines denote reference solution, dotted lines denote multiscale solution.

front region. The pressure and saturation errors are listed in Table (2.7.3) as well as the adaptive updating details of the basis and correction functions. We notice that the percentage of the recomputed basis and correction functions is much larger than those of the compressible flow problem in the SPE10 top layer (Table (2.7.2)). In vertical gravity segregation, there are two waves traveling in the vertical direction, which causes significant saturation changes in a much larger region than in the compressible flow case. Moreover, gravity segregation involves strong counter-current flow of the two phases; as a result, accurate computations of the phase velocities are crucial to obtain accurate saturation fields. Therefore, a relatively small threshold is used for the adaptive computation of the basis and correction functions. Here we take $\epsilon_\lambda = \epsilon_g = 0.1$.

$t \ (\tau)$	e_p	e_s	$f_p(\%)$
0.1	1.5e-4	7.81e-3	26.03
0.5	6.8e-4	4.64e-2	39.92
0.8	4.4e-4	6.36e-2	48.72
1	6.7e-4	6.65e-2	55.79

Table 2.2: Errors and percentage of the recomputed basis functions at several times for the vertical segregation in heterogeneous reservoir

In summary, we have verified that OBMM is quite accurate for modeling compressibility and gravity in two-phase systems. We also compared the incorporation of compressibility in OBMM with the approach of Lunati and Jenny [2006]. We show that OBMM is easier to construct and gives more accurate results.

2.8 General Two-phase Flows

We now study more general two-phase flows that are closer to practical reservoir simulation applications. Both compressibility and gravity are considered in all the cases. The main objective is to study the effects of the coarsening ratio and adaptivity

threshold value on the performance of OBMM for general two-phase flow problems.

We first evaluate the effects of the coarsening ratio on the accuracy of the multi-scale results using the Dirichlet boundary conditions for the two-phase displacement problem. Then, a quarter of a five-spot injection problem is studied to explore the effects of threshold values for adaptive updating of correction and basis functions. The formation and fluid properties used here are listed in Table (2.3).

porosity, ϕ	$\phi = \phi_0 \exp(c_r(p - p_0)),$	$c_r = 10^{-5} \text{psi}^{-1},$	$\phi _{p=14.7 \text{psi}} = 0.1$
water density, ρ_w	$\rho_w = \rho_{w0} \exp(c_w(p - p_0)),$	$c_w = 10^{-6} \text{psi}^{-1},$	$\rho_w _{p=14.7 \text{psi}} = 64 \text{lbm/ft}^3$
oil density, ρ_o	$\rho_o = \rho_{o0} \exp(c_o(p - p_0)),$	$c_o = 10^{-5} \text{psi}^{-1},$	$\rho_o _{p=14.7 \text{psi}} = 32 \text{lbm/ft}^3$
k_{rw}	$k_{rw} = S_w^2$		
k_{ro}	$k_{ro} = S_o^2$		
water viscosity, μ_w	1 cp		
oil viscosity, μ_o	2 cp		

Table 2.3: Properties used for the study of general two-phase flows.

We note that in the cases studied here, the flow is either driven by boundary conditions, or source and sink terms. We do not include sophisticated well models [Peaceman, 1977] in our multiscale computations. Wolfsteiner et al. [2006] first introduced a well model with multiple completions in MsFVM, where a well basis function was constructed for each well on a local domain that contains all perforations of that well and also includes several dual blocks. Very recently, Jenny and Lunati [2009] proposed an alternative approach in MsFVM by constructing the well basis functions with the same support as the pressure dual basis functions. In this new approach, each well needs a well basis function in every dual block penetrated by that well. As with correction functions, the well basis functions can be easily integrated into the framework of OBMM. However, since the focus of this dissertation is mainly on multiscale modeling of complex physics, we leave out well modeling for future work.

2.8.1 Effects of Coarsening Ratio

For convenience, we study only uniform coarsening, i.e., each primal coarse block contains the same number of fine cells. When the coarsening ratio is increased, the influence region of the reduced boundary condition on the dual grid will be larger, and the multiscale solution will usually be less accurate. Moreover, increasing the coarsening ratio does not necessarily improve the overall computational efficiency. For a large coarsening ratio, the size of each coarse block is also large, and the solutions of the basis and correction functions become more expensive, which may reduce the efficiency of OBMM as shown in Fig. (2.6). An optimal coarsening ratio can be estimated according to the solution of Eq. (2.57), which is based on a fixed updating ratio of the basis and correction functions. Actually, for a large coarsening ratio, the time-change of the mobility in a small area triggers re-computation in larger dual blocks, which increases computational cost. Thus, in practice it may require trial and error to achieve an optimal coarsening ratio. The focus here is to evaluate the influence of the coarsening ratio on the accuracy of multiscale results.

We take a part of the permeability field as shown in Fig. (2.18). The fine grid is 55×55 , and we study two coarsening ratios: 5×5 and 11×11 . The pressure on the left and right sides is fixed at 2000 and 1000 psi, respectively. The other sides are no-flow boundaries. The characteristic time τ is defined in Eq. (2.62).

Fig. (2.20) shows the saturation results of the fine-scale method and OBMM for the two coarsening ratios. Globally, the multiscale results for both coarsening ratios are in good agreement with the fine-scale result. However, there are also noticeably larger errors for the larger coarsening ratio as indicated by the black circles in Fig. (2.20). Those errors are located around the water front. Table (2.4) gives the errors and the percentage of recomputed basis and correction functions for the two coarsening ratios. It is clear that the multiscale errors increase with the coarsening ratio. However, for the coarsening ratio 11×11 , the coarse grid is only 5×5 and thus the influence region of

each dual basis function is quite large relative to the whole domain, i.e., in this case the support region of a basis function accounts for $4/25$ (16%) of the domain. Therefore, the maximum saturation error 6.42% indicates that OBMM gives reasonable accuracy even for this aggressive coarsening ratio. We also notice that larger coarsening ratios result in larger fractions of basis and correction function re-computation, which is expected.

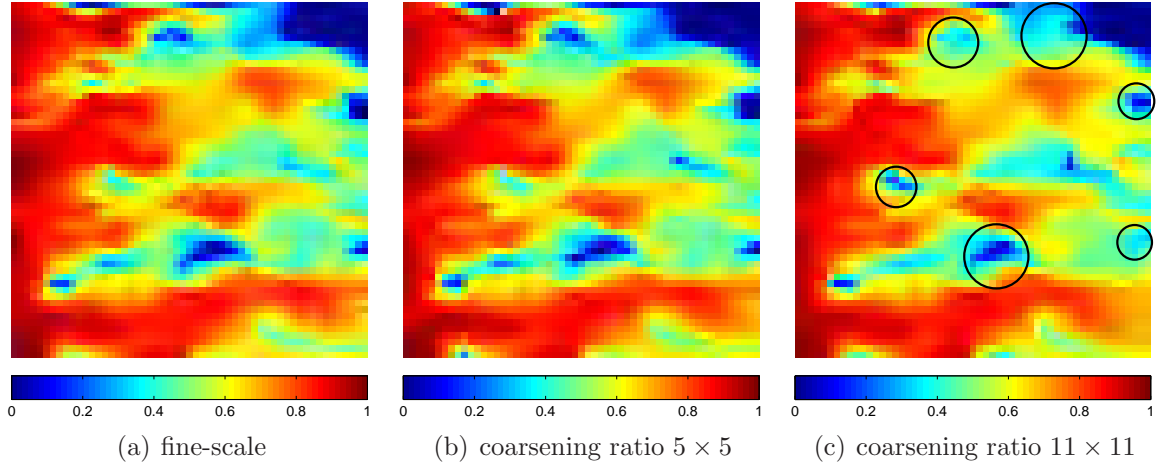


Figure 2.20: Fine-scale reference saturation and multiscale saturation for different coarsening ratios at $t = 1\tau$

	5 × 5			11 × 11		
time (τ)	e_p	e_s	f_p	e_p	e_s	f_p
0.1	6.63e-3	1.46e-2	16.96%	1.76e-2	2.45e-2	20.83%
0.2	6.51e-3	1.75e-2	17.13%	1.81e-2	3.69e-2	20.83%
0.5	6.55e-3	3.63e-2	19.10%	1.68e-2	6.00e-2	24.75%
0.8	7.09e-3	3.76e-2	19.46%	1.91e-2	6.42e-2	24.06%
1.0	7.02e-3	3.39e-2	18.13%	1.97e-2	5.49e-2	22.22%

Table 2.4: Pressure and saturation errors and percentage of recomputed basis and correction functions for different coarsening ratios

2.8.2 Effects of Threshold on Adaptive Computation

To achieve high efficiency in OBMM, we update the basis and correction functions adaptively. Since the equations for the basis and correction functions have the same left hand side as given by Eq. (2.23) and Eq. (2.40), for general flows, the basis and correction functions should be consistently updated together in a given region. Thus, the thresholds ϵ_λ and ϵ_g together control updating of both the basis and correction functions. For the study here, ϵ_λ and ϵ_g are taken to be the same in the following examples and both are denoted as ϵ . This may not be the best choice, but it is a convenient way for us to evaluate the effects of the threshold values on the accuracy of multiscale computations.

We use the permeability field shown in Fig. (2.18). The fine grid is 70×70 and the coarse grid is 10×10 . We study a quarter of five-spot injection/production pattern, i.e., inject from the left upper corner and produce from the right lower corner. Both injection and production wells have a fixed rate of 100 barrels per day. The reservoir is 700×700 ft². The characteristic time for this case is given by the pore volumes injected (PVI), which is defined as the ratio of injected fluid volume to the pore volume.

Fig. (2.21) and Fig. (2.22) show the saturation results and production histories of the fine-scale reference and the multiscale method with different adaptivity thresholds. All the multiscale results are close to the fine-scale results. An error comparison is shown in Table (2.5) together with the percentages of recomputed basis and correction functions. The error in the multiscale results increases only slightly, as a larger threshold, ϵ , is used and the fraction of recomputed basis and correction functions becomes much smaller. Thus, in this case it is effective to use $\epsilon = 1$, which improves the computational efficiency of multiscale methods while the compromise on accuracy is almost negligible.

The efficiency of OBMM is demonstrated by computational complexity analysis

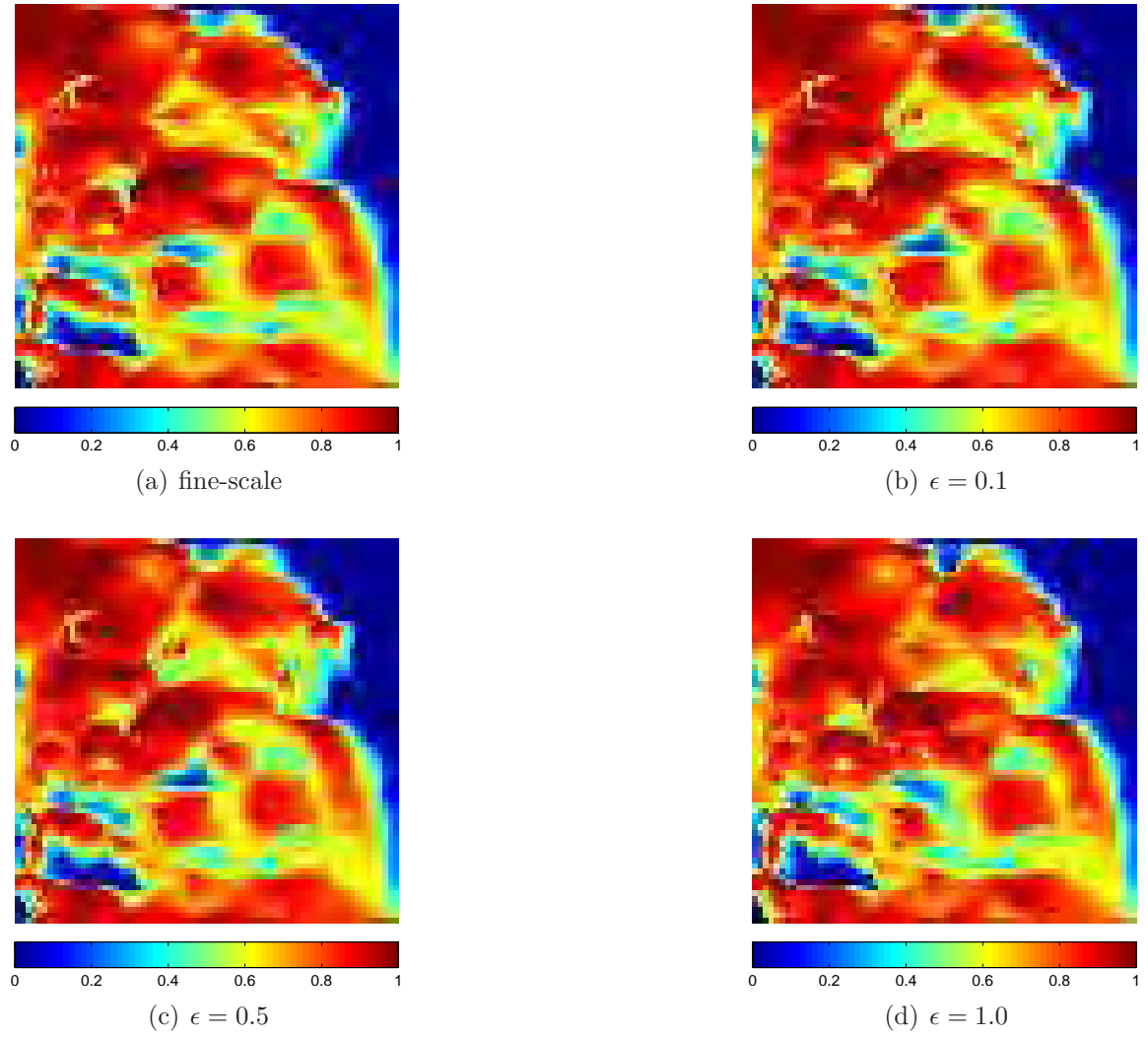


Figure 2.21: Fine-scale reference saturation and multiscale saturation for different adaptivity thresholds

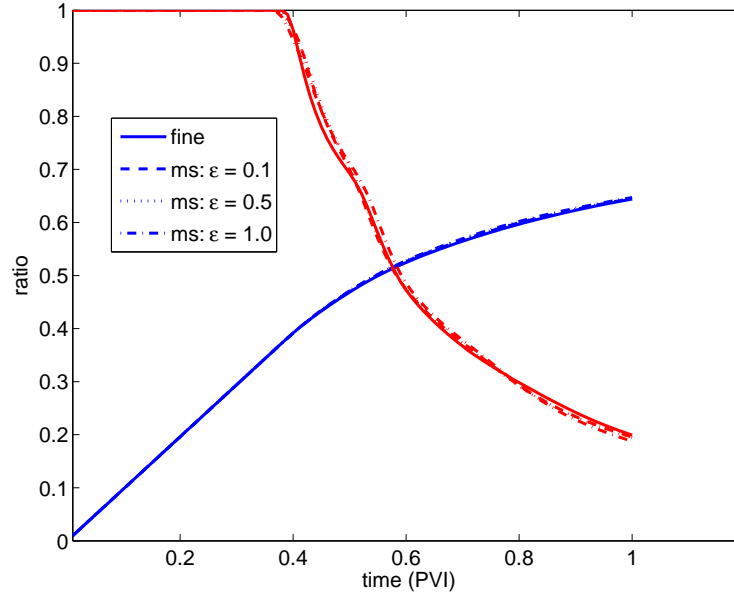


Figure 2.22: Recovery and production history of the fine-scale and the multiscale method with different adaptivity thresholds: blue lines denote the ratio of recovered oil and red lines represent the fraction of oil in the production well

	$\epsilon = 0.1$			$\epsilon = 0.5$			$\epsilon = 1.0$		
	e_p	e_s	f_p	e_p	e_s	f_p	e_p	e_s	f_p
0.1τ	4.21e-4	1.60e-2	18.64%	4.23e-4	1.59e-2	10.96%	4.22e-4	1.56e-2	8.82%
0.2τ	4.09e-4	3.55e-2	25.45%	4.11e-4	3.63e-2	12.28%	4.18e-4	5.03e-2	7.90%
0.5τ	4.40e-4	3.86e-2	43.96%	4.37e-4	4.01e-2	11.53%	4.58e-4	5.51e-2	5.39%
0.8τ	4.88e-4	3.89e-2	52.00%	4.88e-4	4.32e-2	10.59%	5.27e-4	5.67e-2	4.75%
1.0τ	4.22e-4	3.93e-2	46.91%	4.27e-4	4.29e-2	9.42%	4.49e-4	5.74e-2	4.15%

Table 2.5: Pressure and saturation errors and percentage of recomputed basis and correction functions for different adaptivity thresholds

and the percentages of adaptive local updating. We do not report CPU time because the current implementation of OBMM for general flow problems uses Matlab, which does not support highly efficient computations of large-scale problems. In Chapter 4, we develop an Algebraic Multiscale Solver (AMS) based on OBMM, which is implemented in C++. The CPU time efficiency is clearly demonstrated for large problems there. We have more work to do to combine the general multiscale flow modeling framework in this chapter and the multiscale transport modeling framework in Chapter 3 with the efficient and robust AMS. When such an implementation is completed, the efficiency of multiscale modeling for general flow and transport problems can be fully demonstrated in terms of CPU time.

2.9 Limitations of OBMM

So far, we have shown that OBMM is a general multiscale framework that can easily and accurately take into account complex physical mechanisms. It has also been demonstrated that OBMM can be applied to highly heterogeneous permeability fields. Note that to ensure mass conservation, the OBMM in this chapter is derived from MsFVM, i.e., using the finite-volume type of restriction operator. However, there exist two types of problems that pose serious difficulties for MsFVM, and, in turn, OBMM.

The two difficulties for MsFVM are channelized permeability fields with extreme permeability contrasts [Lunati and Jenny, 2004] and problems with high anisotropy mobility ratios [Kippe et al., 2008]. A well known example of a reservoir model with long and thin meandering channels is the bottom 35 layers of the SPE comparative test case 10 (referred to as SPE10) [Christie and Blunt, 2001]. The two limitations are caused by the non-monotonicity of the coarse-scale operator of MsFVM for high anisotropy and strongly channelized systems. As pointed out by Hesse et al. [2008],

the coarse-scale operator of MsFVM is identical to the construction of a certain multipoint flux approximation (MPFA) that suffers from non-monotonicity in the computed pressure fields of the elliptic flow problem. The non-monotonicity is due to the presence of anisotropy (tensor permeability or large grid aspect ratio), or severe permeability contrasts that include extremely low permeability values. For more detailed discussion, refer to Aavatsmark [2002].

Here, we show two examples where MsFVM and OBMM fail to yield accurate results. The two examples consider only incompressible flow, so we can focus on the permeability field and mobility ratio. Furthermore, as noted before, OBMM is identical to MsFVM for incompressible flow problems when the finite-volume type of restriction operator is used. Thus, we use OBMM to compute the multiscale solutions.

In the first case, the permeability field is extracted from the bottom layer of the SPE10 test case, as shown in Fig. (2.23a). The fine grid is 220×54 and the coarse grid is 22×6 (i.e., a coarsening ratio of $10 \times 9 = 90$). This case is isotropic, i.e., $k_x = k_y$ and $\Delta_x = \Delta_y$, where Δ_x and Δ_y are the cell sizes in the x and y directions, respectively. The permeability is highly heterogeneous and contains complex structures with long correlation lengths in one direction and small correlation lengths in the other direction, which is characteristic of fluvial reservoirs. This type of model is often described as “channelized” permeability. We study single-phase flow without compressibility or gravity. The pressure is fixed at 5000 psi and 1000 psi on the left and right boundaries, respectively; no-flow boundary conditions are specified on the top and bottom boundaries. In Fig. (2.23), we compare the pressure solution using the OBMM with the reference solution obtained by a conventional fine-scale method. The pressure should be bounded by the Dirichlet boundary pressure values, i.e., 1000 psi and 5000 psi. However, as shown in Fig. (2.23c), the multiscale pressure is out of bounds in a few locations, which is caused by the non-monotonicity of the OBMM coarse-scale operator. Fig. (2.23d), which is the OBMM solution plotted using the

same scale as the reference fine-scale solution in Fig. (2.23b), indicates that OBMM matches the overall pressure distribution reasonably well in most places, but that it exhibits large errors in a few isolated locations.

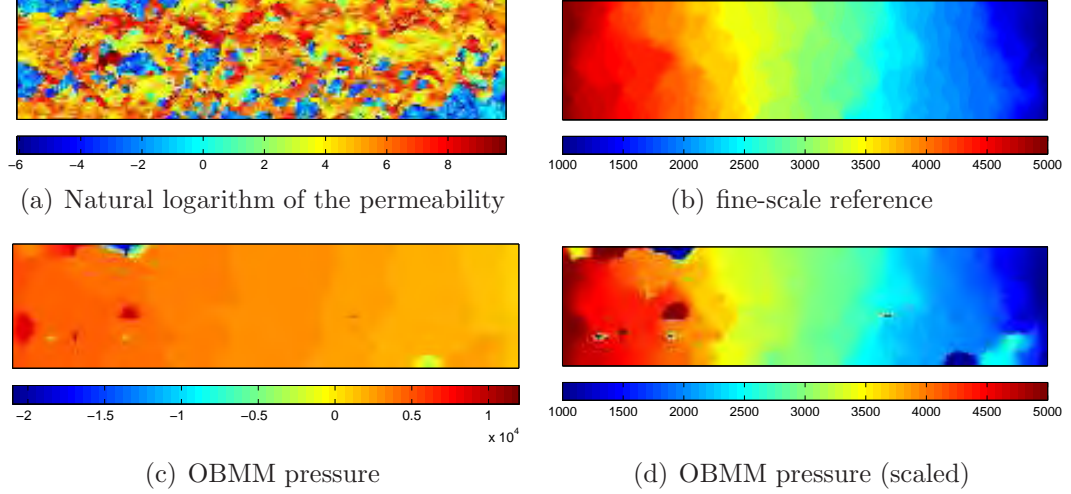


Figure 2.23: Permeability and pressure solutions for the SPE 10 bottom layer

The second example employs a mildly heterogeneous permeability field. The log-permeability distribution, which is shown in Fig. (2.24a), is generated by Sequential Gaussian Simulation [Deutsch and Journel, 1998] with a dimensionless correlation length of 0.2 in each direction. The fine grid is 70×70 and the coarse grid is 10×10 . The permeability in the x and y direction is the same, while $\Delta_y = 100\Delta_x$, which represents a highly anisotropic problem. The same boundary conditions as in the first case are specified. The pressure solutions for the OBMM and the reference are shown in Fig. (2.24). It can be seen from Fig. (2.24c) that the OBMM pressure is out of bounds (i.e., larger than 5000 psi) in some cells. Fig. (2.24d) shows that even when plotted using the same scale as the reference solution, the differences between the OBMM and reference solutions are still large.

The two examples clearly show the non-monotonicity of OBMM solutions for channelized permeability and a high mobility ratio. One possible solution may be to

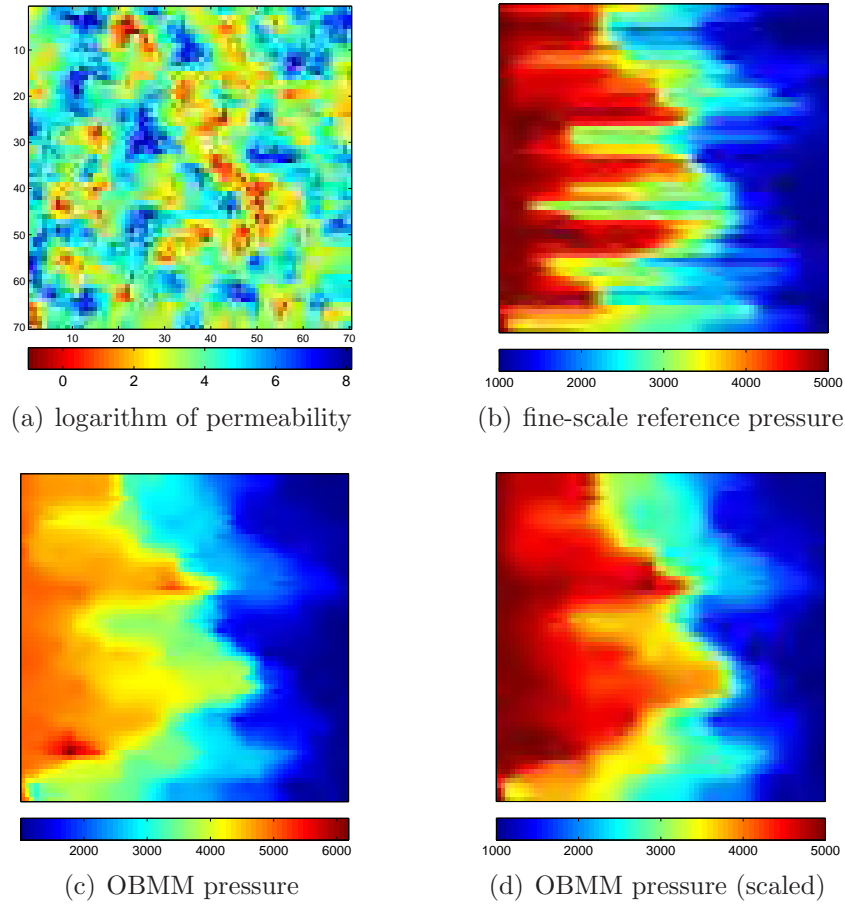


Figure 2.24: Permeability and pressure solutions for the anisotropic case

employ the Galerkin type of restriction operator instead of the finite-volume type in OBMM for problems with channelized permeability or high mobility ratios. On the other hand, the Galerkin type of restriction operator does not ensure mass conservation, which is essential to solve coupled flow and transport problems. We will tackle this dilemma in Chapter 4, where a two-stage algebraic multiscale solver (TAMS) is proposed.

2.10 Conclusions

An operator-based multiscale method (OBMM) was developed as a general algebraic multiscale framework to solve multiphase flow problems. The key ingredients of the method are two algebraic multiscale operators, prolongation and restriction, with which the multiscale solution is constructed algebraically. We focused on the application of OBMM to flow (i.e., pressure) problems. The prolongation operator for pressure is assembled from the (dual) basis functions. The restriction operator depends on the chosen discretization scheme for the coarse-scale equations. We have shown the restriction operators based on finite-volume and Galerkin finite-element methods.

OBMM is easy to implement, and since only matrix multiplication operations are involved, we can rely on state-of-the-art linear algebra libraries to achieve high efficiency. OBMM can be applied to unstructured grids, since the multiscale solution algorithm is purely algebraic. Furthermore, it is straightforward to extend OBMM to general flow problems that involve more physical mechanisms, such as compressibility, gravity and capillary pressure.

We have shown that OBMM accounts for compressibility effects in a natural way. The fine-scale equations contain the fine-scale compressibility information, and the basis functions are calculated with compressibility effects. The coarse-scale operators

constructed by OBMM account for compressibility by summing all the fine-scale accumulation terms in a coarse block and distributing the contribution to the coarse block itself and adjacent coarse blocks according to the basis functions. Gravity and capillary pressure can be incorporated into OBMM by constructing correction functions in a similar way to the computation of the basis functions, and this additional treatment is straightforward.

The efficiency of OBMM relative to standard fine-scale methods mainly lies in the fact that we do not solve a global fine-scale system. Constructing and solving the coarse-scale equations takes a relatively small computational effort compared with solving the global fine-scale system. Moreover, adaptive updating of the basis functions can lead to great efficiency gains. We analyzed the computational complexity of OBMM, in which we argue that OBMM can be significantly more efficient than a fine-scale method. The efficiency of OBMM can be further improved by choosing appropriate coarsening ratios and thresholds for adaptive computation.

For coupled flow and transport problems, a conservative fine-scale velocity field is crucial. In MsFVM, a conservative velocity field is reconstructed by solving Neumann problems locally on the primal coarse blocks. A sequential fully implicit scheme is used to solve the coupled equations.

We validated the ability of OBMM to handle compressibility and gravity using a series of challenging problems. We also studied the effect of the coarsening ratio on the performance of OBMM. In terms of computational efficiency, an appropriate coarsening ratio should be used to achieve high efficiency. Based on reasonable assumptions regarding the computational complexity for solving a linear system, we derived a formulation for the optimal coarsening ratio in OBMM. With the increase of coarsening ratio, the multiscale solution errors increase. Numerical examples show that the increase in the error is mild and that accuracy is remarkably good, even for large coarsening ratios. The effect of adaptive thresholds on updating the basis and

correction functions was also studied, which indicates that for common multiphase flow problems (i.e., slightly compressible, viscous dominated displacements), the accuracy of multiscale solutions is weakly dependent on the adaptivity thresholds, while the efficiency depends strongly on the chosen adaptivity thresholds.

We discussed some limitations of OBMM and MsFVM, i.e., problems with channelized permeability fields and high anisotropy ratios. Such limitations are due to the non-monotonicity of the MsFVM coarse-scale operator. We will address these limitations in Chapter 4.

Chapter 3

Multiscale Modeling of Multiphase Transport

3.1 Introduction

The general algebraic multiscale framework described in the previous chapter was used to solve the flow problem (pressure and total-velocity) for large-scale highly heterogeneous reservoir models. In the OBMM framework, a conservative fine-scale velocity field is reconstructed from the multiscale pressure solution, which is then used to solve the nonlinear hyperbolic transport equation for the fine-scale saturation field. An overlapping Schwarz scheme is used to solve the transport equations, where the primal coarse blocks serve as the computational blocks for the Schwarz computations. With the efficiency of the pressure solution greatly improved by the adaptive multiscale computation, the computational cost in reconstructing the fine-scale velocity and solving the fine-scale transport equations becomes the bottleneck in the overall efficiency.

Compared with the flow problem, development of coarse-scale operators for the nonlinear transport problem (saturation equations) is much more challenging. The

hyperbolic nature of the transport equation entails prolongation and restriction operators that are strongly dependent on the nonlinear evolution of the saturation field, which involves complex interactions with the flow field and the underlying heterogeneous permeability distribution. These complexities are particularly important when the correlation length of the permeability is much larger than the coarse-grid size, which is often the case in modeling natural large-scale formations. In the reservoir engineering community, the pseudo-relative permeability approach has been proposed for upscaling multi-phase flow in porous media. However, it has been documented quite clearly that pseudo-relative permeabilities depend strongly on the boundary conditions, specific flow scenarios, and saturation histories [Barker and Thibeau, 1997].

More recent research on coarsening the transport equation is quite promising. The generalized convection-diffusion model [Efendiev and Durlafsky, 2003] uses a modified convection term and an extra diffusion contribution to capture the subgrid effects. The mathematical framework proposed by Hou et al. [2006] projects the subgrid fluctuation onto averages along streamlines to obtain homogenized saturation equations. Aarnes and Efendiev [2006] proposed two algorithms for the coarse-to-fine interpolator for the transport equations using local boundary conditions, which are either presumed or obtained from the global solution of previous time steps. Efendiev et al. [2008] employed a flow-based coordinate system to model flow and transport using multiscale methods.

In this chapter, we extend the general algebraic multiscale framework to the transport. We propose adaptive prolongation operators for the transport equation based on the observation that the saturation changes in a coarse cell as a function of time can be expressed using asymptotic expansions, once the rapidly moving saturation front sweeps through the local region (e.g., Buckley-Leverett saturation front [LeVeque, 1992]). For regions with relatively slow evolution of the saturation field, linear interpolation operators are constructed and used instead of the overlapping Schwarz

method on the primal coarse grid. We propose a criterion to switch from the Schwarz-overlap method to the linearly interpolated prolongation operations for constructing the saturation field. We propose two approximate prolongation algorithms: (1) a conservative fine-scale algorithm that first interpolates the local velocity field and then updates the fine-scale saturation, and (2) a conservative coarse-scale algorithm that directly interpolates the coarse-scale saturation changes to the fine scale. The numerical efficiency and accuracy are evaluated for two-phase flow with various physical models and permeabilities. It is demonstrated that the multiscale results with the adaptive transport calculations are in excellent agreement with the fine-scale solutions. Furthermore, the adaptive multiscale computations of the flow and transport equations yield a computationally much more efficient algorithm compared with conventional fine-scale reservoir simulation.

The adaptive transport algorithm described here is designed to obtain an accurate fine-scale solution for general multiphase flow problems instead of a coarse-scale saturation field [Efendiev et al., 2000b; Efendiev and Durlofsky, 2002]. In addition, all the computations are performed on the given grid, i.e., without grid transformations (usually defined by streamlines as in Hou et al. [2006]; Efendiev et al. [2008]). Moreover, although the multiscale solutions of flow are employed by Aarnes and Efendiev [2006] and Efendiev et al. [2008], their purpose is not to resolve the fine-scale details, but rather to introduce a flexible mechanism to model the flow on the coarse scale more accurately.

This chapter is organized as follows. In Section 3.2, the restriction and three adaptive prolongation operators for the hyperbolic transport equation are described. The adaptivity criteria, which determine the choice of prolongation operator at a specific time for different regions of the domain, are presented in Section 3.3. Then in Section 3.4, we discuss several algorithmic issues, such as the coupling between flow and transport equations and the computational complexity of the adaptive multiscale

transport algorithm. In Section 3.5, various numerical examples with different permeabilities, physics, and well settings are presented to show the efficiency, accuracy, and robustness of the proposed method. Section 3.6 concludes this chapter.

3.2 Restriction and Prolongation Operators for Transport

The objective here is to solve transport equations arising from general multiphase flow problems. For the purpose of illustrating the basic ideas, we avoid the complex and somewhat tedious terms in the discrete saturation equation (Eq. (2.12)), and we focus on the transport equation for two-phase incompressible flow:

$$\phi \frac{\partial S}{\partial t} + \nabla \cdot (f \mathbf{u}_t) = -q. \quad (3.1)$$

In the saturation equation Eq. (3.1), the fractional flow, f , is usually a strong non-linear (S -shaped) function of saturation, and the total velocity, \mathbf{u}_t , is computed from the solution of the pressure equation and Darcy's law for the individual phases.

The fine-scale linearized discrete form of Eq. (3.1) for fine cell i can be written as

$$A_i^f(\mathbf{S}^f) = \sum_{j \in \mathbb{N}_i} \left(\frac{\partial f_{ij}}{\partial S_{\hat{ij}}} u_{\hat{ij}} \right) \delta S_{\hat{ij}} - \beta_i (S_i^{f,n+1} - S_i^{f,n}) = q_i - \sum_{j \in \mathbb{N}_i} f_{ij}(S_{\hat{ij}}^f). \quad (3.2)$$

Here, the subscripts and superscripts follow the same convention as in the last chapter,

$$\beta_i = \frac{\phi V(\Omega_i^f)}{\Delta t}, \quad (3.3)$$

and \mathbb{N}_i denotes the set of all the neighboring cells of cell i , and subscript \hat{ij} denotes the upwinding cell of the interface between cells i and j .

Following the algebraic multiscale framework, we first define the restriction operator for transport. Conservation is essential in solving Eq. (3.1), especially on the coarse scale. Therefore, a finite-volume restriction operator, as defined by Eq. (2.28), is used for the saturation equation. We repeat it here for convenience:

$$\mathcal{R}_{K,i} = \begin{cases} 1 & \text{if } \Omega_i^f \subset \Omega_K^c \\ 0 & \text{otherwise} \end{cases} \quad (K = 1, \dots, n_c; \ k = 1, \dots, n_f). \quad (3.4)$$

To maintain mass conservation on the coarse and fine scales, the coarse-scale saturation is naturally defined as the volume average saturation for each primal coarse cell:

$$S_K^c = \frac{1}{V(\Omega_K^c)} \sum_{\Omega_i^f \in \Omega_K^c} V(\Omega_i^f) S_i^f, \quad (3.5)$$

where $V(\Omega)$ denotes the pore volume of domain Ω .

The most challenging part is to define the prolongation operator for saturation, such that we can derive the coarse-scale saturation equation by an operator based approach and also reconstruct the fine-scale saturation distribution. One of the difficulties is that it is practically impossible to construct basis functions for saturation by solving local problems, as we do for pressure. With the propagation of the saturation field, the local saturation distribution changes dramatically as a function of time. Therefore, it is quite hard to define a general prolongation operator for saturation. The other difficulty is that the fractional flow curve $f(S_i^f)$ is a strongly nonlinear function of saturation (i.e., S -shaped) and the saturation distribution may include shocks (i.e., discontinuity in space). In addition, multi-phase flow effects interact with the underlying heterogeneous permeability field in a complex manner. As a result, we cannot derive the coarse-scale operators for saturation solely as a function of the coarse-scale saturation.

In a displacement process, the injected fluid moves from an injection well toward a production well, in which a Buckley-Leverett-like saturation distribution will be established with complex interactions of the saturation front with the underlying permeability heterogeneity. Typical saturation profiles at times t and $t + \Delta t$ for a 1D problem are shown in Fig. (3.1).

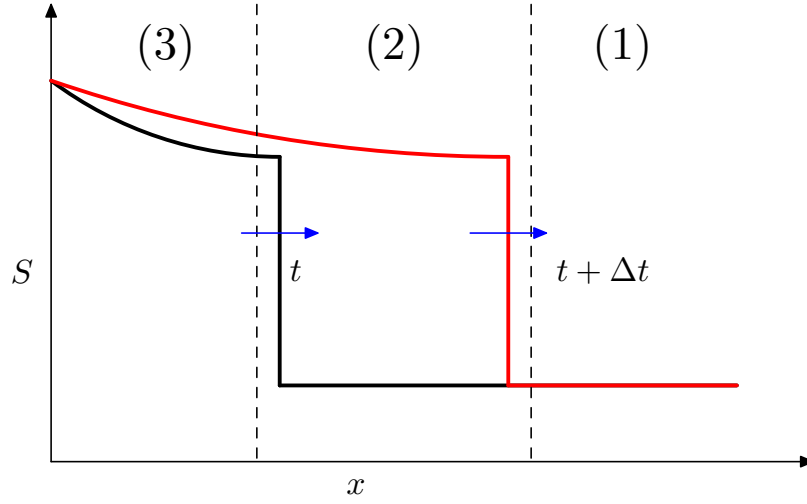


Figure 3.1: Typical Buckley-Leverett saturation profiles at time t and $t + \Delta t$ for a 1D problem divided into three regions.

The Buckley-Leverett profile motivates the design of an adaptive algorithm in which, for the time interval of interest, the domain is divided into three regions: (1) Region 1, where the injection fluid has not reached, (2) Region 2, where an injection front encroached and the saturation of the injection fluid increases rapidly, and (3) Region 3, where the saturation distribution in the fine-scale cells contained in a given coarse cell is well established after the sharp front has moved through. Therefore, the idea is to construct an approximate coarse-scale saturation solution that can be used to decompose the domain into three regions for the time interval of interest. Then, different prolongation operators are defined and used adaptively in the different regions.

If the saturation in a coarse cell increases, or decreases, monotonically after the saturation front has moved through, we can estimate the coarse-scale fractional flow curve from the saturation changes of the previous time step, or iteration. Let us express the saturation change in a fine cell as a fraction of the coarse-grid saturation change as

$$\xi_{i,K} = \frac{S_i^{f,n} - S_i^{f,n-1}}{S_K^{c,n} - S_K^{c,n-1}} \quad \text{for } \Omega_i^f \in \Omega_K^c. \quad (3.6)$$

A prolongation operator can be defined from Eq. (3.6), i.e.,

$$\mathbf{S}^f = \mathcal{P}\mathbf{S}^c + \mathbf{S}^{corr}, \quad (3.7)$$

with

$$\begin{aligned} \mathcal{P}_{i,K} &= \xi_{i,K} \quad (i = 1, \dots, n_f, K = 1, \dots, n_c), \\ \mathbf{S}^{corr} &= \mathbf{S}^{f,n-1} - \mathcal{P}\mathbf{S}^{c,n-1}. \end{aligned} \quad (3.8)$$

The coarse-scale system for saturation is then constructed as follows,

$$\begin{aligned} \mathcal{R}\mathbf{A}^f\mathcal{P}\mathbf{S}^c &= \mathbf{q} - \mathcal{R}\mathbf{A}^f\mathbf{S}^{corr}, \\ \mathbf{A}^c &= \mathcal{R}\mathbf{A}^f\mathcal{P}, \end{aligned} \quad (3.9)$$

where the fine-scale system, \mathbf{A}^f , is defined from the fine-scale equations (Eq. (3.2)). Accordingly, the coarse-scale equation for a coarse cell I obtained from Eq. (3.9) can be written as,

$$\begin{aligned} A_I^c(\mathbf{S}^c) &= \sum_{J \in \mathbb{N}_I} \delta S_{IJ}^c \sum_{\ell \in \partial \Omega_{IJ}^c} \frac{\partial f}{\partial S_\ell^f} u_\ell \xi_{\ell, IJ} - (S_I^{c,n+1} - S_I^{c,n}) \sum_{i \in \Omega_I^c} \beta_i \xi_{i,I} \\ &= \sum_{i \in \Omega_I^c} q_i - \sum_{J \in \mathbb{N}_I} \sum_{\ell \in \partial \Omega_{IJ}^c} f_\ell u_\ell \end{aligned} \quad (3.10)$$

The coarse-scale velocity, U , is naturally defined as the flux through the coarse-grid interface, i.e.,

$$U_{\widehat{IJ}} = \sum_{\ell \in \partial\Omega_{\widehat{IJ}}^c} u_\ell. \quad (3.11)$$

Then, we define the coarse-scale fractional flow, F , as

$$F_{\widehat{IJ}} = \frac{1}{U_{\widehat{IJ}}} \sum_{\ell \in \partial\Omega_{\widehat{IJ}}^c} f(S_\ell^f) u_\ell. \quad (3.12)$$

The coarse-scale equation for coarse cell i , Eq. (3.10), can then be expressed using coarse-scale quantities as follows,

$$A_I^c(\mathbf{S}^c) = \sum_{J \in \mathbb{N}_I} (F'_{\widehat{IJ}} U_{\widehat{ij}}) \delta S_{\widehat{IJ}}^c - \beta_I^c(S_I^{c,n+1} - S_I^{c,n}) = q_I^c - \sum_{J \in \mathbb{N}_I} F_{\widehat{IJ}} U_{\widehat{IJ}}, \quad (3.13)$$

where,

$$\begin{aligned} F'_{\widehat{IJ}} &= \frac{1}{U_{\widehat{IJ}}} \sum_{\ell \in \partial\Omega_{\widehat{IJ}}^c} \frac{\partial f}{\partial S_\ell^f} u_\ell \xi_{\ell, \widehat{IJ}}, \\ \beta_I^c &= \sum_{i \in \Omega_I^c} \beta_i \xi_{i, I}, \\ q_I^c &= \sum_{i \in \Omega_I^c} q_i. \end{aligned} \quad (3.14)$$

Equation 3.13 shows that the structure of the coarse-scale saturation system constructed by OBMM is quite similar to that of the fine-scale saturation system. From an implementation point of view, one can choose to construct the coarse-scale system from Eq. (3.9) as for the pressure equation, or directly from Eq. (3.13), which is also quite straightforward to implement.

The coarse-scale saturation, S^c , is then obtained from (3.9) or Eq. (3.13), and as shown in the next section, the three computational regions can be identified based

on changes in the coarse-grid saturation and velocity as a function of time. We now show how to adaptively construct the fine-grid saturation field in the three regions using the various prolongation operators.

3.2.1 Prolongation Operator I: Full Velocity-Full Saturation (FVFS)

When the invading fluid moves into a coarse cell, sharp saturation changes accompanied by complex interactions with the underlying heterogeneous permeability take place. In this situation, a conservative fine-scale velocity field has to be constructed before solving the transport problem. The construction of a conservative fine-scale velocity field is described in the previous chapter.

In regions with significant changes in saturation as a function of time, we do not have a rigorous prolongation operator that allows us to avoid solving the local fine-scale transport problem. Therefore, the fine-scale solution is computed using a one-level block-based Schwarz overlap method, which is the strategy used in the original MsFVM [Jenny et al., 2004; 2006] and in Chapter 2. Because this amounts to full reconstruction, it is an accurate, but computationally expensive prolongation scheme. As a result, we employ full-reconstruction adaptively only for regions, in which rapid saturation changes as a function of time are detected.

We reconstruct the fine-scale velocity for the domain Ω_I^c according to the primal pressure by solving Eq. (2.48). Then, we solve Eq. (3.2) for the domain Ω_I^c

$$A_i^f(\mathbf{S}^{f,\nu+1}) + \mathbf{r}^{f,\nu+1} = 0 \quad \text{for } i \text{ in } \Omega_i^H \quad (3.15)$$

with the Neumann boundary conditions:

$$S_\ell^{f,\nu+1} = S_\ell^{f,\nu}, \quad u_\ell^{\nu+1} = u_\ell^\nu \quad \text{for } \ell \in \partial\Omega_I^c. \quad (3.16)$$

The superscript ν indicates the iteration level and the approximation of (3.16) provides the localization of the problem so that the equation can be solved for each coarse cell. From (3.5), the coarse-grid saturation can be computed readily from the fine-grid saturation field.

The FVFS operator is locally conservative and accurate in constructing fine-grid saturations; however, it entails iterative implicit saturation computations on the primal coarse cells with Neumann boundary conditions to obtain a globally converged solution. Furthermore, this approach also involves an expensive process for constructing a conservative fine-scale velocity field. If the FVFS operator is applied in every coarse cell, the method is exactly the same as described in the previous chapter, i.e., the transport problem is solved on the fine grid using the multiscale solution of the flow problem.

3.2.2 Prolongation Operator II: Approximate Velocity-Full Saturation (AVFS)

Computing a conservative fine-scale velocity is an expensive process, since it requires solution of the fine-scale pressure equations. However, the total-velocity field, which usually displays significant spatial variability and structure, is typically a weak function of time. That is, the change in the total-velocity between time steps is usually small, and will be even smaller between iteration levels. This motivates the use of an approximate velocity field without solving local Neumann problems.

The proposed prolongation operator II comprises two steps: (1) reconstruction of a locally conservative fine-grid total-velocity field using direct interpolation of the coarse-grid velocity and (2) explicit computation of fine-grid saturations. This operator is referred to as the Approximate Velocity-Full Saturation (AVFS) operator, since it constructs an approximate velocity by linear interpolation while solving the

full saturation equation.

Assume that the velocity distributions at the coarse and fine grids are available from the previous time step, or the previous iteration (ν), i.e., U_I^ν for coarse cell I and u_j^ν for fine cell j ($\Omega_j^f \in \Omega_I^c$) are known. From the multiscale solution of the pressure equation Eq. (2.21), we obtain a new coarse-grid velocity: $U_I^{\nu+1}$. If the velocity does not change much, we can interpolate the coarse-grid velocity change to the fine-grid velocity at the new iteration level. For Cartesian grids, the interpolation can be expressed in a simple form:

$$\begin{aligned} u_j^{\nu+1}(\mathbf{x}) &= u_j^\nu(\mathbf{x}) + U_i^{\nu+1}(\mathbf{x}_0) - U_i^\nu(\mathbf{x}_0) \\ &+ \frac{\mathbf{x} - \mathbf{x}_0}{\mathbf{x}_1 - \mathbf{x}_0} \otimes (U_i^{\nu+1}(\mathbf{x}_1) - U_i^\nu(\mathbf{x}_1) - U_i^{\nu+1}(\mathbf{x}_0) + U_i^\nu(\mathbf{x}_0)), \end{aligned} \quad (3.17)$$

where the vector operations are defined as $\mathbf{x}/\mathbf{y} = (x_1/y_1, x_2/y_2)$, $\mathbf{x} \otimes \mathbf{y} = (x_1 y_1, x_2 y_2)$, and \mathbf{x}_0 and \mathbf{x}_1 are the coordinates of the coarse cell at the bottom-left and top-right corners of a Cartesian cell, respectively. One can quickly show that $\nabla \cdot U = 0$ if $\nabla \cdot u = 0$. This indicates if u_j^ν and $U^{\nu+1}$ are conservative, the interpolated fine-grid velocity, $u_j^{\nu+1}$, is also conservative on the fine grid. Once the fine-grid velocity is estimated, the saturation can be computed using an explicit method:

$$S_j^{f,\nu+1} = S_j^{f,\nu} + \frac{\Delta t}{V_j} \sum_{\ell} u_{\ell}^{\nu+1} f(S_j^{f,\nu}). \quad (3.18)$$

The stability of the explicit saturation calculation is governed by the CFL number:

$$CFL = u_j \frac{\partial f(S_j^f)}{\partial S_j^f} \frac{\Delta t}{\Delta x}. \quad (3.19)$$

The CFL number should be less than one for stability of the explicit calculation [LeVeque, 1992]. If this algorithm is applied in the domain where $\partial f(S_j^h)/\partial S_j^h \ll 1$

(i.e., rarefaction behind the Buckley-Leverett front), the restriction on the timestep size will be mild. If there is a timestep size restriction due to stability, we can use local time stepping, or an implicit formulation, i.e., solving the transport equation in local coarse cells as given by Eq. (3.15).

The AVFS operator is also locally conservative and is more efficient than the FVFS operator, since it avoids the process of reconstructing the fine-scale velocity. The error from interpolating the fine-scale velocity may introduce some error in the fine-scale saturation. By construction, these errors are small, since this AVFS operator ensures local mass conservation, and it is used only when the coarse-scale velocity changes as a function of time are small.

3.2.3 Prolongation Operator III: Approximate Saturation (AS)

The third operator is just the prolongation operator defined by Eq. (3.8), which is also referred as AS operator, since it directly constructs an Approximate Saturation field. The AS operator is applied algebraically to construct a coarse-scale saturation system from Eq. (3.9) and then to reconstruct the fine-scale saturation distribution based on Eq. (3.7).

The AS operator does not involve solving any differential equations and is very efficient. However, this prolongation operator does not guarantee saturation conservation on the fine grid, even though the saturation field is conservative on the coarse grid. Nevertheless, the conservation errors are expected to remain small and bounded because (1) the saturation field is conservative on the coarse grid, and (2) this prolongation operator is applied only in regions where the saturation changes are quite small for the time interval, or iteration level, of interest.

An assumption of the AS operator is that the relative saturation change (ξ_l) does not vary much from the previous iteration. It is a reasonable approximation for a coarse cell in which the saturation changes are slow behind a steep saturation front.

As will be shown in the numerical examples, we can identify regions, where this simple interpolator can be safely applied to yield high numerical efficiency and accuracy.

3.3 Adaptive Computation of Saturation

In the last section, we proposed one restriction operator and three prolongation operators for saturation, which enables us to devise an efficient algorithm without compromising numerical accuracy. The strategy is to construct a coarse-scale saturation system using the restriction and algebraic AS prolongation operators. Based on the coarse-scale solutions, we adopt a corresponding prolongation operator to reconstruct the fine-scale saturation for each coarse cell. The adaptive computation is crucial for the proposed method to maintain both accuracy and efficiency. Hence, the criteria to switch between prolongation operators are also essential components of the algorithm.

The criteria are also motivated by the Buckley-Leverett displacement process as shown in Fig. (3.1). In Region 1, we do not need to compute the fine-scale saturation because the changes in the saturation field over the time interval of interest are negligible. On the other hand, Region 2 entails the most rigorous (and costly) algorithm: prolongation operator I, the FVFS operator, which performs full local construction of velocity and saturation and does not require information regarding the saturation history. In Region 3, where the saturation change becomes relatively small and the saturation distribution is smooth, either Prolongation Operators II (the AVFS operator) or III (the AS operator) is applied depending on the details of the saturation change and distribution. As discussed earlier, the AVFS operator is more expensive than the AS operator, but the AVFS operator yields a locally conservative fine-scale saturation, whereas the AS operator is only locally conservative on the coarse scale. Thus, we need to have a good criterion to use Operator III for Region 3 in order to ensure that the conservation errors on the fine scale are bounded and small.

To identify the transitions between Regions 1, 2 and 3, we employ criteria based on changes in the coarse-scale total-velocity and saturation fields, which are readily available from the coarse-scale solutions of pressure and saturation. The transition from Regions 1 to 2 in coarse cell i is detected using the following simple condition

$$\|\Delta S_i^c\| > \Delta_1, \quad (3.20)$$

and the transition from Regions 2 to 3 is identified by the changes in both saturation and velocity :

$$\begin{aligned} \|\Delta S_i^c\| < \Delta_2 \quad \text{and} \\ \left(\left\|\frac{\Delta U_i}{U_i}\right\| < \Delta_v^1 \text{ for } \|U_i\| > \epsilon_v \text{ or } \|\Delta U_i\| < \Delta_v^2 \text{ for } \|U_i\| \leq \epsilon_v\right). \end{aligned} \quad (3.21)$$

Next, a criterion is needed to choose between Operators II and III for Region 3. If the relative saturation change ξ_l in Eq. (3.6) does not vary much, Operator III should yield small fine-scale saturation errors. A variable that measures the changes in ξ for each coarse cell is introduced:

$$\Xi_i \equiv \frac{\max\{\xi_{l,i}\}}{\min\{\xi_{l,i}\}} \quad \text{for } l \in \Omega_i^H. \quad (3.22)$$

When the condition

$$\Delta \Xi_i < \Delta_\xi \quad (3.23)$$

is satisfied in Region 3, Operator III is used.

Note that if these criteria become very restrictive, the transport equation will be solved using Prolongation Operator I, which is identical to the original full reconstruction algorithm of [Jenny et al., 2006] as shown in the previous chapter. As the

criteria get looser, computational efficiency improves, but the errors are expected to increase.

3.4 Computational Aspects of Multiscale Transport

3.4.1 Algorithm for Coupled Flow and Transport Problems

We apply a sequential implicit scheme for the coupled system of flow and transport. Both flow and transport are computed using the adaptive multiscale method. Fig. (3.2) shows the algorithm.

3.4.2 Computational Complexity

We now evaluate the computational complexity of the adaptive multiscale modeling of the transport problem and compare it with fine-scale computations of transport as in existing multiscale methods (also described and used in the previous chapter). Similarly to the complexity analysis for the flow problem in Section(2.6.2), we assume that solution of linear systems is the dominant factor in solving transport problems.

In existing multiscale finite-volume methods [Jenny et al., 2006; Lee et al., 2008; Zhou and Tchelepi, 2008], a conservative fine-scale velocity has to be reconstructed, and then a transport equation is solved in each primal coarse cell employing an additive Schwarz overlap scheme. For convenience, we refer to this existing approach as MSOM (Multiscale Schwarz Overlap Method), and the proposed method with multiscale modeling for saturation as MSAT. Thus, in MSOM, the transport related computation comprises two parts: constructing the fine-scale total-velocity and solving for the fine-scale saturation. The computational cost of the first part, as discussed

```

1:  $n = 0$ 
2: Construct the restriction operator for pressure and saturation from Eq. (2.28).
3: /* time evolving */
4: while  $n < \text{total time steps}$  do
5:    $p^f = p^{f,n}$ ,  $S^f = S^{f,n}$ 
6:
7:   do /* outer iterations */
8:      $p^{f,\nu_p} = p^f$ .
9:     Re-compute the basis and correction functions if needed.
10:    Assemble the prolongation operator and correction vector for pressure.
11:    Solve for  $\mathbf{p}^c$  from the coarse-scale pressure system.
12:    Reconstruct the fine-scale pressure  $p_f$  from Eq. (2.21).
13:    Compute the coarse-scale velocity  $U^{\nu_p+1}$ .
14:
15:    do /* inner iterations */
16:       $S^{f,\nu_s} = S^f$ .
17:      Construct the AS prolongation operator from Eq. (3.8).
18:      Solve for  $S_c$  from coarse-scale saturation system.
19:      Identify the three Buckley-Leverett transport regions.
20:      Apply a prolongation operator (AS, AVFS, or FVFS) to reconstruct the
        fine-scale saturation  $S^f$  in each coarse cell.
21:    until  $\|S^f - S^{f,\nu}\| < \epsilon_s$ 
22:
23:  until  $\|p^f - p^{f,\nu_p}\| < \epsilon_p$ 
24: end while

```

Figure 3.2: Adaptive multiscale computation of both flow and transport

in Section(2.6.2), is

$$t_1 = n_c t_p(Cr), \quad (3.24)$$

where $t_p(n) = n^\alpha$ is the same as defined in Section(2.6.2).

We assume that solving a linear system of size n for the transport problem takes a time of

$$t_s(n) = \mathcal{O}(n^\beta). \quad (3.25)$$

Then, in one iteration, solving the transport problem for all the primal coarse cells requires

$$t_2 = n_c t_s(Cr). \quad (3.26)$$

The total time spent on the transport in MSOM is thus

$$t_{s,msom} = n_c(t_p(Cr) + t_s(Cr)). \quad (3.27)$$

For MSAT, we assume that the fraction of coarse cells that use the FVFS operator (Prolongation Operator I) is f_I , and the fraction for the AVFS operator (Prolongation Operator II) is f_{II} . Thus, the computational cost of MSAT is

$$t_{s,msat} = n_c [f_I t_p(Cr) + (f_I + f_{II}) t_s(Cr)] + t_s(n_c). \quad (3.28)$$

We take an example with a fine grid of $512 \times 512 \times 512$. The speedup of MSAT over MSOM for transport is plotted for different coarse-grid sizes in Fig. (3.3) for a series of f_I and f_{II} . We take $\alpha = \beta$, and two values are considered, namely, 1.5 and 1.2.

Fig. (3.3) shows that when an appropriate coarse grid is used, i.e., the size of the coarse grid is not close to that of the fine grid, MSAT speedups over MSOM are almost linear with f_I and f_{II} . Actually, from Eq. (3.27) and (3.28), if we take $\alpha = \beta$

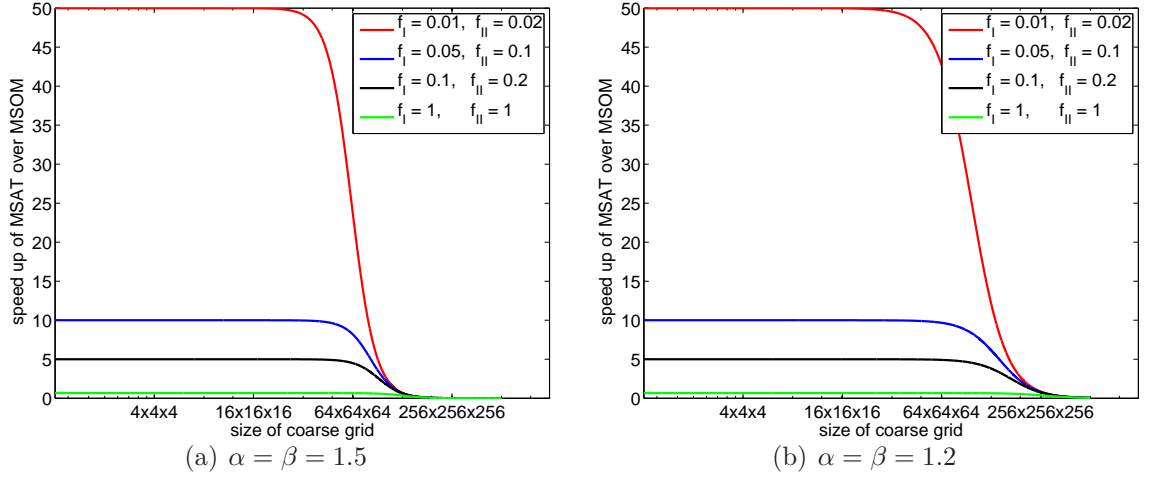


Figure 3.3: Speedup of MSAT over MSOM for transport

and assume $t_s(n_c)$ is small since n_c is much smaller than n_f , we get

$$\frac{t_{s,msom}}{t_{s,msat}} = \frac{2}{2f_I + f_{II}}, \quad (3.29)$$

which can be used as a quick estimate of the efficiency of multiscale modeling of transport.

Here, we do not directly compare the overall efficiency of the multiscale solution of both flow and transport with that of the fine-scale method. This is because it is difficult to make a priori estimates of the ratio of the computational time for transport compared to that for flow. The transport equation is usually strongly nonlinear, and it is hard to estimate the iteration numbers.

3.5 Numerical Examples

In this section, we present several numerical examples to test the accuracy and efficiency of the proposed multiscale method for both flow and transport. We start with simple physics: incompressible two-phase flow without gravity effects. Various

boundary conditions (source/sink or Dirichlet boundary conditions) are employed. Different types of permeability fields are investigated. Then, more physical mechanisms, such as compressibility and gravity are included. In the end, a large-scale 3D case is presented to demonstrate the numerical efficiency of adaptive multiscale computations of flow and transport, and the effects of the adaptivity thresholds for transport computation are also investigated.

3.5.1 Incompressible Two-Phase Flow and Transport

We first illustrate how the multiscale method for transport works using some simplified settings. The fluids are assumed to be incompressible and the quadratic relative permeability model is employed ($k_{ro} = S_o^2$ and $k_{rw} = S_w^2$). The viscosity ratio between the water and oil is 1 : 5 (unfavorable displacement). The nonlinear convergence tolerances for pressure and saturation are 1 psi and 10^{-4} , respectively. In the adaptive transport algorithm, the following transition criteria are used, $\Delta_1 = 10^{-5}$ for the transition from Region 1 (before the invasion of the injection fluid) to Region 2 (sharp saturation changes); $\Delta_2 = 10^{-2}$, $\Delta_v^1 = 0.1$, $\Delta_v^2 = 10^{-4}$, and $\epsilon_v = 10^{-4}$ are used for the transition from Regions 2 to 3 (slow saturation change after the saturation front has moved through). Slightly different thresholds for the relative saturation change (Δ_ξ) are used in different reservoir models. We find that highly heterogeneous models require a tight tolerance of Δ_ξ in order to maintain numerical accuracy. Here, we use $\Delta_\xi = 10^{-3}$ for the first two examples and $\Delta_\xi = 10^{-4}$ for the 10th SPE Comparative Model.

We take the fine-scale solution as reference, and the L_2 norms of pressure and saturation errors are defined by

$$e_p = \frac{\|p^{ms} - p^f\|_2}{\|p^{init}\|_2} \quad (3.30)$$

$$e_s = \|S^{ms} - S^f\|_2. \quad (3.31)$$

Note that the pressure error norm e_p is normalized by the initial pressure in Cases 1 and 2, but in the linear displacement process of Case 3, we employ the pressure difference between the inlet and outlet boundaries to normalize e_p .

Case 1: Homogeneous Domain

We now consider a two-dimensional reservoir model of $700 \text{ ft} \times 700 \text{ ft}$ with homogeneous permeability $k = 100 \text{ md}$. Even though the domain is two-dimensional, the model is assumed to have a unit thickness (1 ft) in the third dimension for the convenience in specifying the operating conditions. The fine-scale grid, 70×70 , is uniformly coarsened into a 10×10 coarse grid. The upscaling factor is 49 as each coarse block comprises 7×7 fine cells. The reservoir is originally saturated with oil; water is injected to displace oil. We inject water from the upper left corner and produce from the lower right corner. The initial reservoir pressure is 2000 psi. The water injection rate is constant at reservoir conditions (50 bbl/day), and the reservoir fluid is produced at the same rate. The injection and production rates are evenly distributed in the coarse cells (e.g., injection in the left upper coarse cell and production in the right lower coarse cell). Figs. (3.4 – 3.7) depict the pressure and saturation at $t = 0.2 \text{ PVI}$ and $t = 0.8 \text{ PVI}$ (pore volume injected), respectively, computed using three different methods: (1) the fine-scale method (*FM*), (2) the multiscale method without adaptivity of the transport computation (Schwarz-overlap for transport, *MSOM*), and (3) the multiscale method with adaptive transport computation (*MSAT*) proposed here. The differences in pressure and saturation computed by the three methods in Figs. (3.4 – 3.7) are quite small.

In Fig. (3.8), the saturations computed adaptively by *MSAT* are shown for three different times. The white squares indicate Region 2, in which Prolongation Operator I (Schwarz-overlap) is employed, at least once, in the iteration loop of pressure and

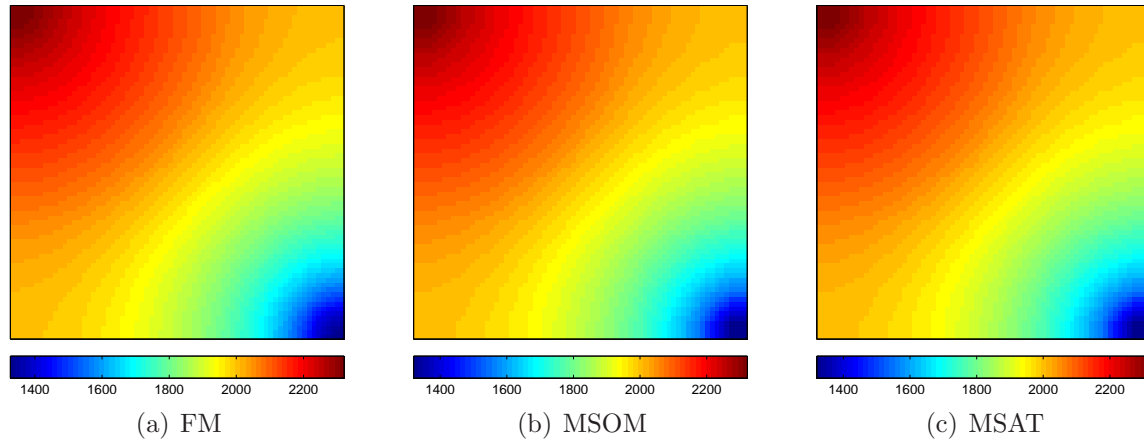


Figure 3.4: Pressure distribution at $t = 0.2$ PVI in Case 1 with homogeneous permeability

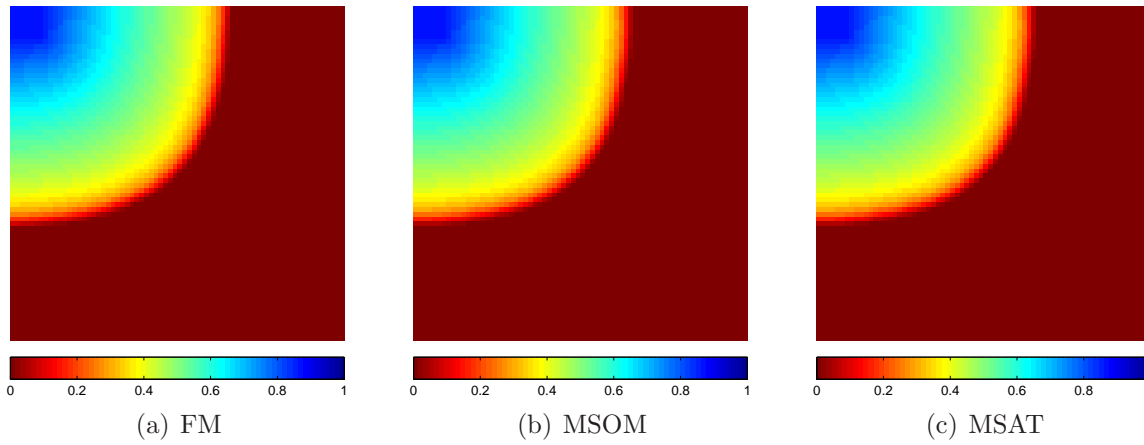


Figure 3.5: Saturation distribution at $t = 0.2$ PVI for Case 1 with homogeneous permeability

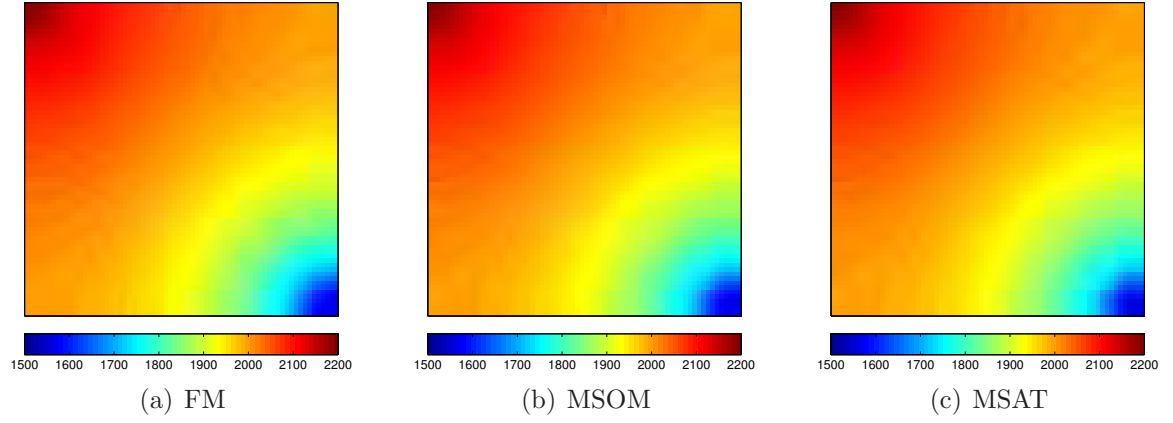


Figure 3.6: Pressure distribution at $t = 0.8$ PVI for Case 1 with homogeneous permeability

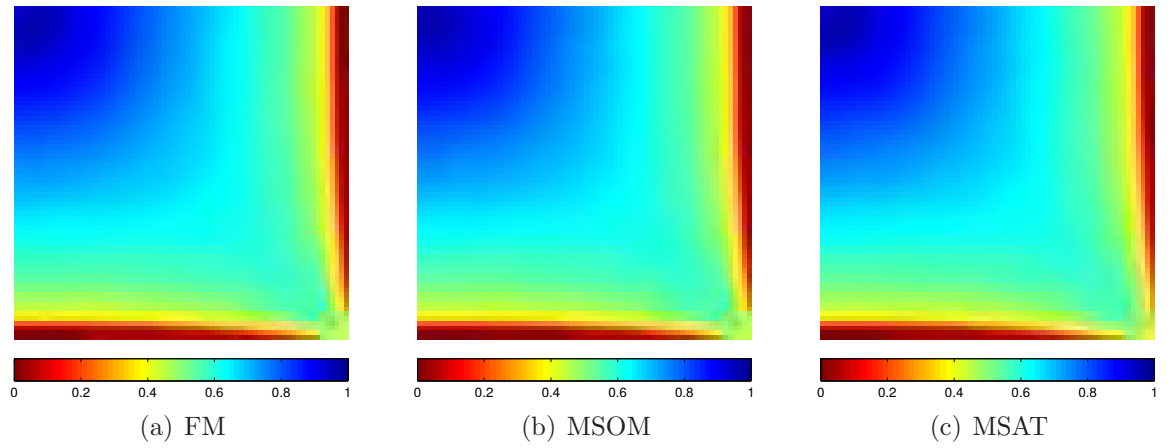


Figure 3.7: Saturation distribution at $t = 0.8$ PVI for Case 1 with homogeneous permeability

saturation calculations for the specific time step. Since the transport equation is non-linear in saturation, multiple Newton iterations are usually required. So, for a given time step, the prolongation operator can be switched from I to II during the iterative process, if the saturation change becomes smaller than the transition criterion. The black squares in Fig. (3.8)(a) indicate Region 3, where Prolongation Operator II is used at least once during the time step. Note that Prolongation Operator I is used mainly in the region around the sharp saturation front. Furthermore, Prolongation Operator II is employed if the saturation and total-velocity changes are small. Later in time, as the saturation distribution became well established in most of the domain, Prolongation Operator III is employed widely in the transport calculations. Note that determination of the Regions is performed automatically and adaptively by the simulator based on the computed transition criteria during the solution process.

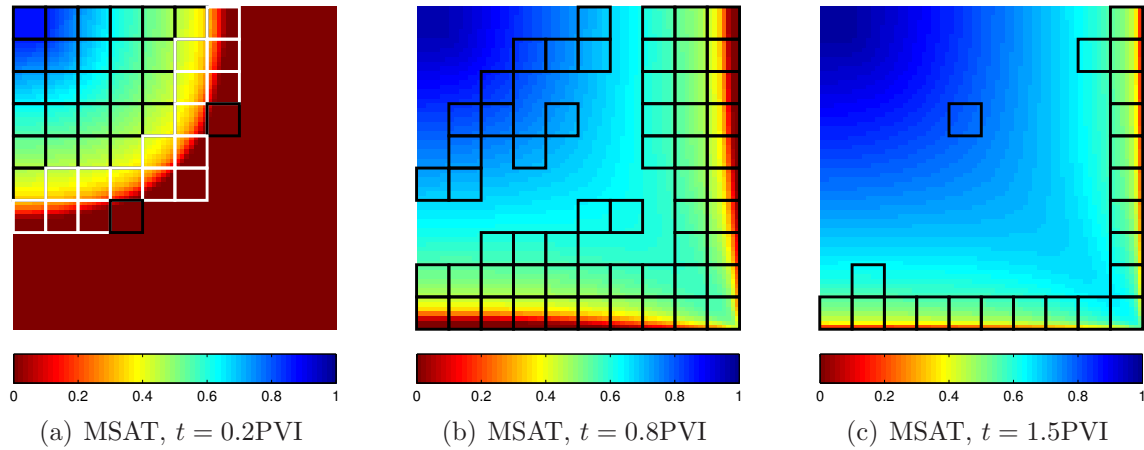


Figure 3.8: Adaptive saturation computation at three times for Case 1: the white and black squares, respectively, denote the regions where Prolongation Operators I and II are used, at least once, during the iterative saturation computation for the particular time step.

In Table (3.1) the L_2 norms of *MSOM* and *MSAT* solutions, with respect to the reference solution (*FM*), are tabulated for various times, and the adaptivity ratios in

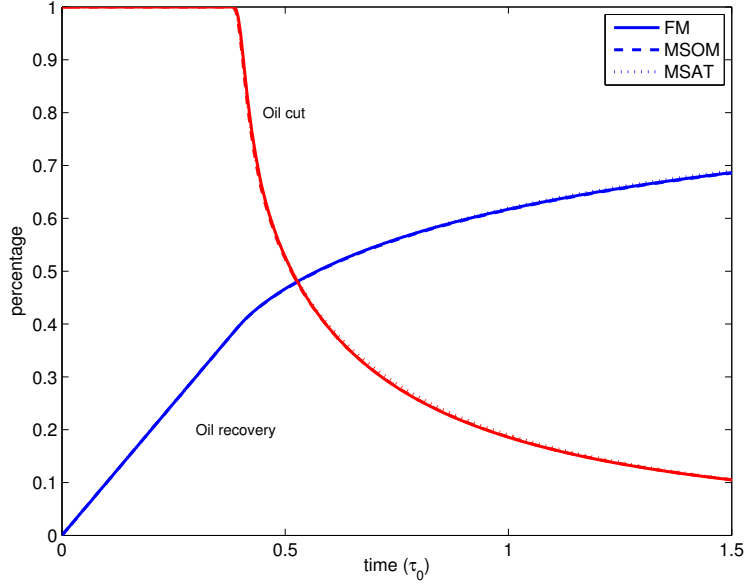


Figure 3.9: Cumulative oil recovery and oil fraction for Case 1

pressure and saturation calculations are also included. Here, f_p denotes the fraction of updated basis functions, f_I the fraction of coarse blocks that need fine-scale transport calculations using Prolongation Operator I, and f_{II} is the fraction of coarse blocks that employ Prolongation Operator II. All the adaptivity statistics are expressed as the average fraction computed from the initial condition up to the current time. For instance, the fraction of coarse cells, in which Prolongation Operator I is applied to compute the saturation field from $t = 0$ to $t = 0.8$ PVI is 6.01%. As discussed in Section (3.4.2), the speedup of MSAT over MSOM is closely related with f_I and f_{II} , and an estimation is given by Eq. (3.29). We do not report the CPU time here because it is only meaningful for large-scale problems.

From this numerical example, we first note that pressure from the adaptive transport calculation (*MSAT*) is as accurate as that from the original MSFV [Jenny et al., 2006] without transport calculation adaptivity (*MSOM*). *MSAT* yields slightly higher numerical errors in saturation computation than *MSOM*, but these errors are quite

t (PVI)	e_p		e_s		$f_p(\%)$		$f_I(\%)$	$f_{II}(\%)$
	MSOM	MSAT	MSOM	MSAT	MSOM	MSAT	MSAT	MSAT
0.2	1.46e-3	1.46e-3	3.54e-3	3.54e-3	3.31	3.88	10.67	4.55
0.6	1.24e-3	1.07e-3	3.03e-3	5.43e-3	2.89	2.85	7.56	21.42
0.8	1.03e-3	8.40e-4	2.70e-3	6.73e-3	2.50	2.24	6.01	26.00
1.0	9.17e-4	7.42e-4	2.36e-3	8.68e-3	2.17	2.16	4.85	25.38
1.2	8.40e-4	6.94e-4	2.14e-3	1.04e-2	2.05	2.06	4.15	24.15
1.5	7.70e-4	6.69e-4	1.90e-3	1.31e-2	1.95	1.95	3.44	22.13

Table 3.1: Error norms and adaptivity statistics for Case 1 with homogeneous permeability: e_p and e_s are L_2 error norms for pressure and saturation, respectively. The f_p denotes the fraction of updated pressure basis functions employed from the initial time to the current time step. The f_I and f_{II} , respectively, denote the fraction of Prolongation Operators I and II employed in the transport computations from the initial time to the current time step.

small. Numerical errors in the cumulative oil recovery and oil fraction in the production curves are barely noticeable in Fig. (3.9). Secondly, the basis function updates for pressure calculation continuously decrease as the front moves from the injection well to the production well. As the total mobility change is, in general, smaller than the saturation change, the pressure changes during the displacement process are rather small. As a result, a small percentage of basis functions is required to be updated (e.g., 1.95% in 1.5 PVI). Similarly, while the total velocity can be a strong function of location, it tends to change slowly in time, and for this example, the velocity updating during this long injection period of 1.5 PVI is only 3.44%. By comparison, the saturation front experiences a large transition region as it moves from the injection well to the production well. The fraction of the coarse grid model that requires the original fine-scale transport calculations varies between 4.55% and 26.00%. Obviously, we could consider increasing the adaptivity by relaxing the transition criteria (Δ_1 and Δ_2), but this is likely to lead to less accurate results.

Case 2: Mildly Heterogeneous Domain

In this second example, we consider a heterogeneous permeability field with small correlation lengths. We employ the same setting as in the previous case, except that the permeability field is log-normal with a mean of logarithmic permeability of 4 and a variance of 2 (i.e., the same as the permeability used in Section (2.7.3), shown in Fig. (2.18)).

In Figs. (3.10 – 3.13), the pressure and saturation distributions at $t = 0.2$ and $t = 0.8$ PVI are compared for three different methods, *FM*, *MSOM* and *MSAT*. The water saturation distribution exhibits complex structures when the permeability field has long correlation lengths and high variability (see Fig. (3.13)). Notice that the largest saturation errors are localized in the regions where the permeability is very low.

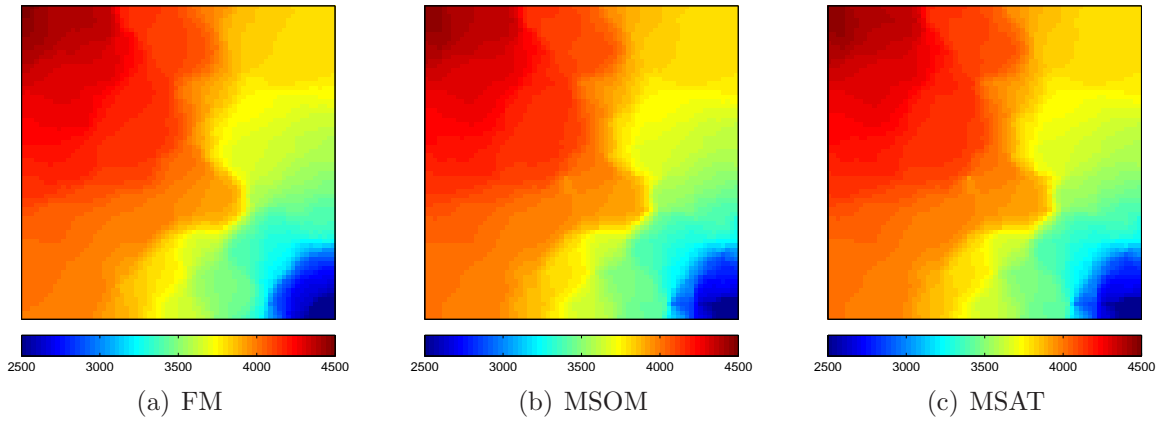


Figure 3.10: Pressure distribution at $t = 0.2$ PVI in Case 2 with log-normal permeability

The adaptive saturation calculation of *MSAT* yields numerical results that are quite close to the original multiscale method without adaptive transport (*MSOM*) [Jenny et al., 2006]. In Table (3.2), L_2 norms of *MSOM* and *MSAT*, with respect

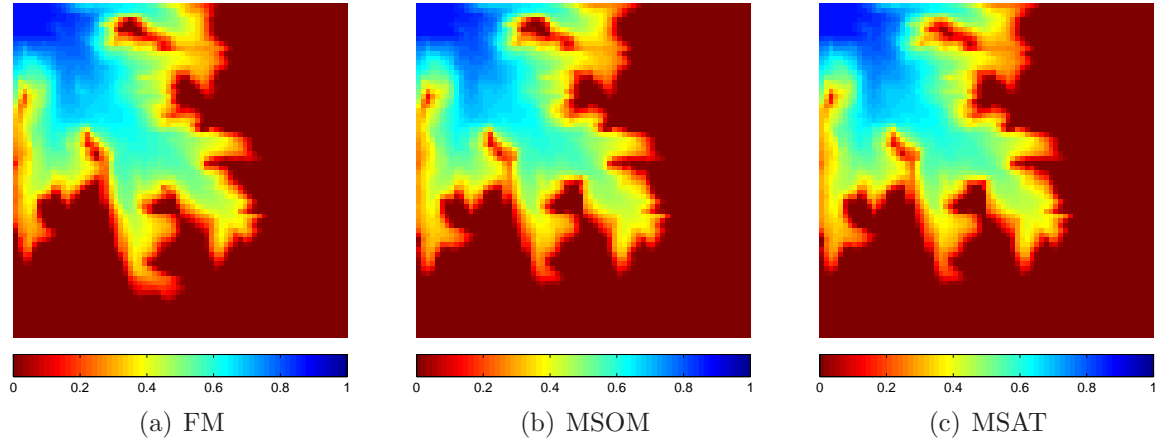


Figure 3.11: Saturation distribution at $t = 0.2$ PVI in Case 2 with log-normal permeability

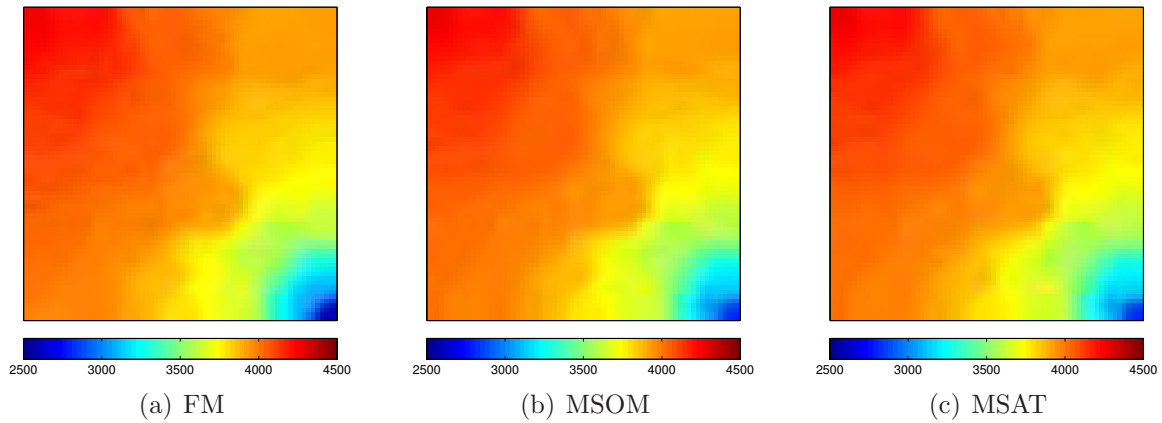


Figure 3.12: Pressure distribution at $t = 0.8$ PVI in Case 2 with log-normal permeability

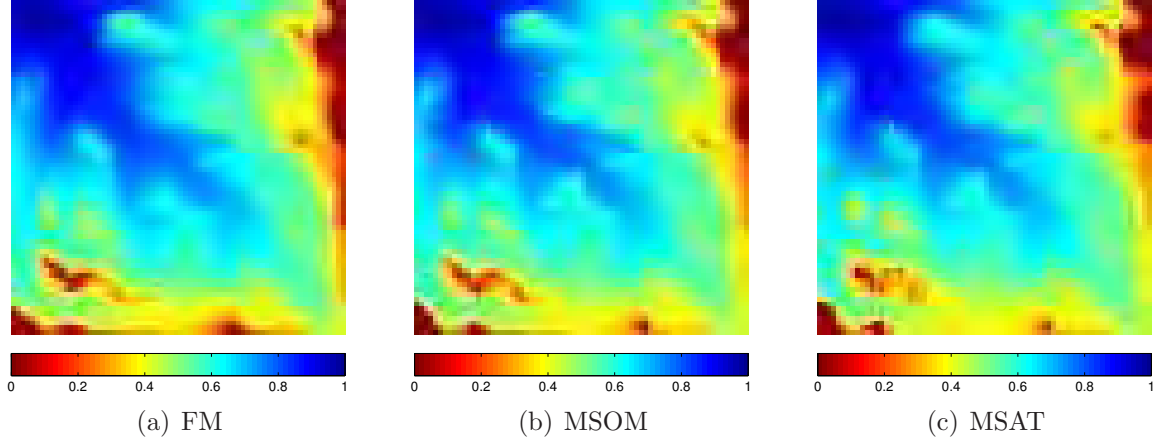


Figure 3.13: Saturation distribution at $t = 0.8$ PVI in Case 2 with log-normal permeability

to the reference solution (FM), are tabulated for various time steps, and the adaptivity ratios in pressure and saturation calculations are also presented. As shown in Fig. (3.14), the adaptivity of saturation computation is similar to that for the homogeneous case. Prolongation Operator I is employed mainly around steep saturation gradients, and Prolongation Operator II is then used until the saturation distribution becomes established.

t (PVI)	e_p		e_s		$f_p(\%)$		$f_I(\%)$	$f_{II}(\%)$
	MSOM	MSAT	MSOM	MSAT	MSOM	MSAT	MSAT	MSAT
0.2	1.01e-2	9.87e-3	3.89e-2	3.90e-2	2.30	2.19	7.72	5.34
0.6	9.38e-3	9.73e-3	3.49e-2	3.98e-2	2.35	2.32	6.36	20.59
0.8	9.10e-3	9.66e-3	2.99e-2	3.96e-2	2.11	2.10	5.23	23.69
1.0	8.12e-3	8.54e-3	2.33e-2	3.34e-2	1.94	1.92	4.40	23.91
1.2	7.00e-3	7.28e-3	2.01e-2	3.26e-2	1.75	1.74	3.86	23.05
1.5	6.15e-3	6.31e-3	1.90e-2	3.29e-2	1.55	1.54	3.29	21.49

Table 3.2: Error norms and adaptivity statistics for Case 2 with log-normal permeability: the variables are defined in the caption of Table (3.1).

The cumulative oil recovery and the produced oil fraction are plotted in Fig. (3.15). The production histories of the multiscale methods ($MSOM$ and $MSAT$) are hardly

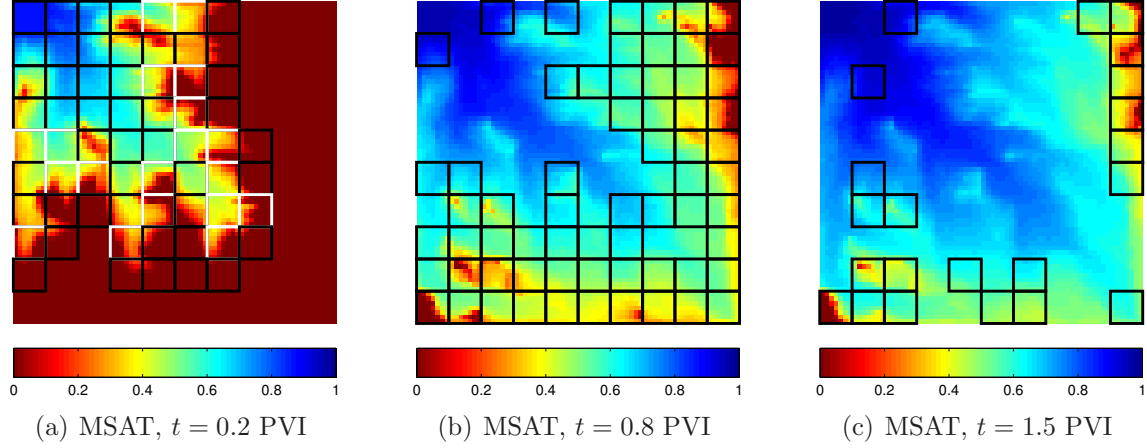


Figure 3.14: Adaptive saturation computation for three time steps in Case 2: the white and black squares respectively denote the region where Prolongation Operator I and II is applied, at least once, in iterative saturation calculation of the time step.

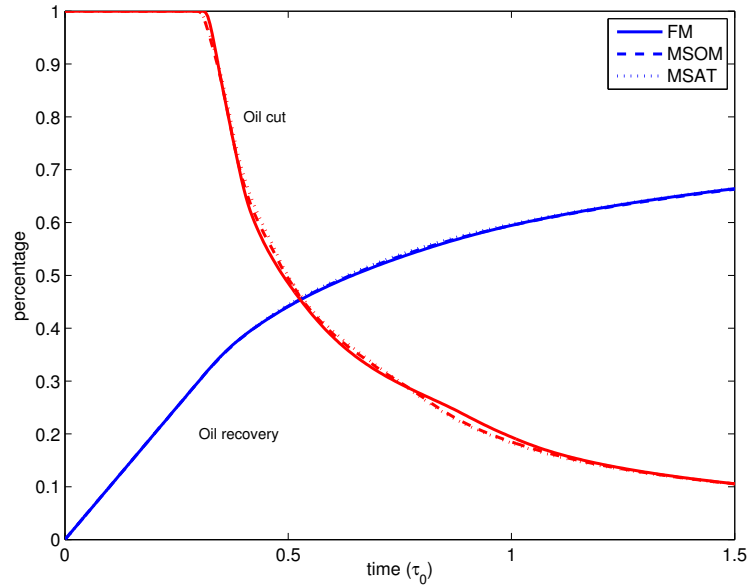


Figure 3.15: Cumulative oil recovery and oil fraction in production (oil cut) in Case 2

distinguishable from the fine-scale reference solution (*FM*). This numerical example demonstrates clearly that the adaptive transport algorithm is quite accurate with significant efficiency gains.

Case 3: Highly Heterogeneous Model

The permeability field is adapted from the top layer of the SPE 10 Problem [Christie and Blunt, 2001] with a fine grid of 220×54 . A 20×6 coarse grid (i.e., a coarsening factor of 11×9) is imposed. The log- permeability field is shown in Fig. (2.8). The initial pressure is 4000 psi. The left boundary is kept at a constant pressure of 4000 psi with water injection, and the right boundary is kept at a constant pressure of 1000 psi with reservoir fluid production. As the production and injection rates are continuously changing with time, we define a characteristic time

$$\tau_o = \frac{\phi L_x^2 \bar{\mu}}{\bar{k} |p^{left} - p^{right}|}, \quad (3.32)$$

where $\bar{\mu}$ and \bar{k} denote characteristic viscosity and permeability, respectively, and L_x is the model dimension in the x direction. The arithmetic average of water and oil viscosity is chosen as $\bar{\mu}$ and the geometric mean of permeability as \bar{k} .

The pressure and saturation distributions at $t = \tau_o$ and $t = 4\tau_o$ from the reference solution and multiscale methods are depicted in Figs. (3.16 – 3.19), respectively. Even though the permeability field is highly heterogeneous, the pressure field in Figs. (3.16) and (3.18) exhibits a relatively simple profile along the flow direction due to the Dirichlet boundary conditions and a much larger domain length compared to its width. On the other hand, the spatial total-velocity variation is significant. Consequently, the saturation distribution clearly indicates that the underlying distribution of heterogeneity results in a complex saturation field, as seen in Figs. (3.17) and (3.19). Prolongation Operator I is used in only a few areas, either around the

saturation fronts or where the total-velocity changes significantly during the timestep. This result is clearly shown in Table (3.3). The fraction of Operator I application is less than 5% in all the listed time steps; and for later times, Operator III is employed in most of the domain. The cumulative oil recovery and the produced oil fraction are plotted in Fig. (3.21). The fine-scale and multiscale results are in excellent agreement, even though the permeability field is highly variable with large correlation lengths. The results of the adaptive multiscale transport approach and the original multiscale method are nearly identical. Due to the strong heterogeneity, we observe slightly larger discrepancy between the fine-scale and multiscale results in this example. However, we believe that this level of accuracy is within acceptable limits for most engineering applications.

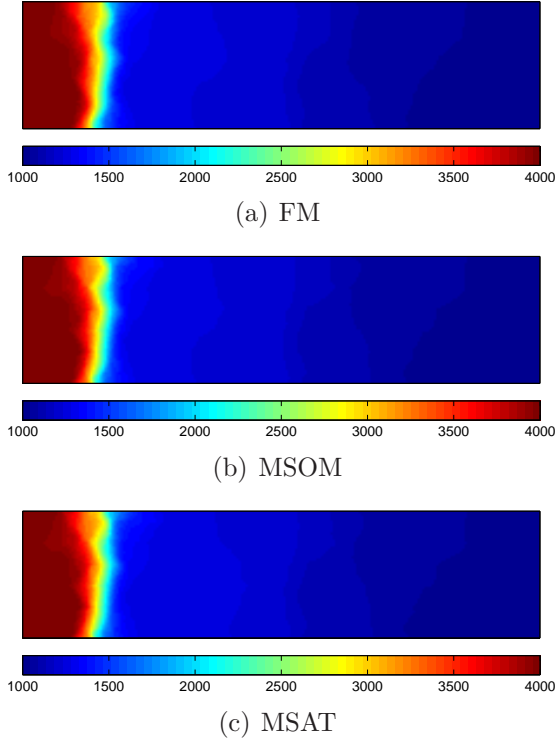


Figure 3.16: Pressure distribution at $t = \tau_o$ in Case 3 with Dirichlet boundary condition

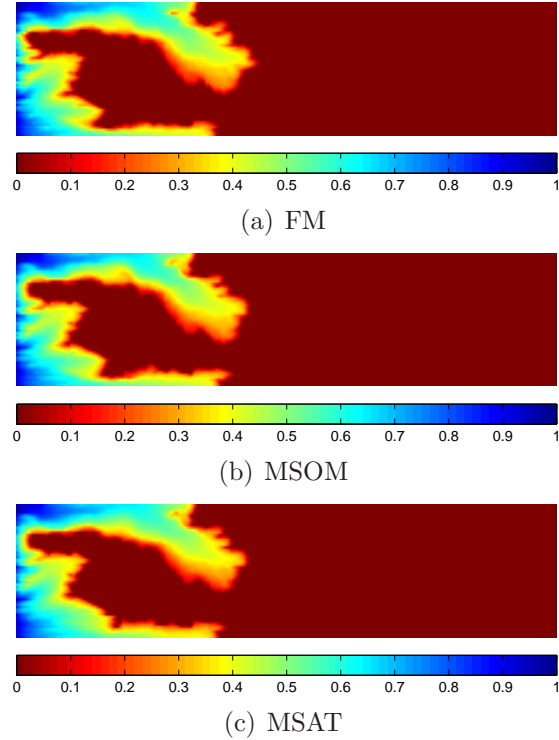


Figure 3.17: Saturation distribution at $t = \tau_o$ in Case 3 with Dirichlet boundary condition

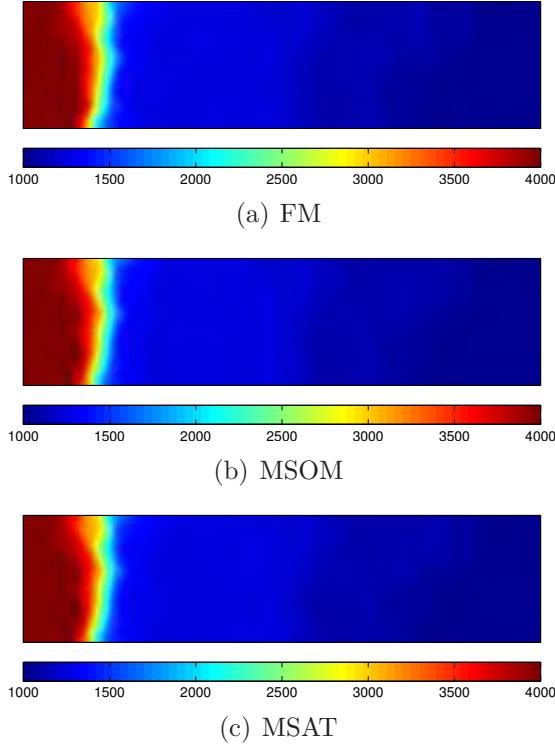


Figure 3.18: Pressure distribution at $t = 4\tau_o$ in Case 3 with Dirichlet boundary condition

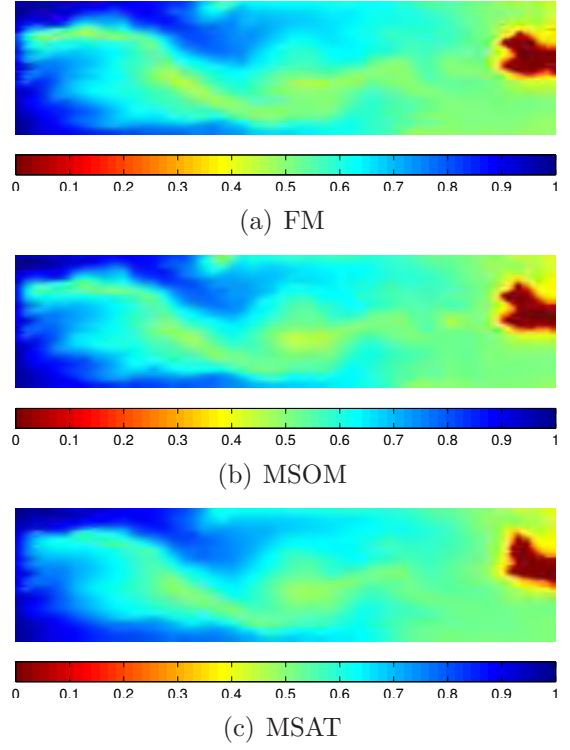


Figure 3.19: Saturation distribution at $t = 4\tau_o$ in Case 3 with Dirichlet boundary condition

t (τ_o)	e_p		e_s		$f_p(\%)$		$f_I(\%)$	$f_{II}(\%)$
	MSOM	MSAT	MSOM	MSAT	MSOM	MSAT	MSAT	MSAT
1	7.37e-3	7.88e-3	3.20e-2	3.87e-2	3.78	3.76	4.20	7.35
2	6.94e-3	7.90e-3	4.12e-2	5.07e-2	4.41	4.49	4.28	15.77
3	7.28e-3	7.85e-3	3.14e-2	4.20e-2	4.65	4.79	3.82	24.85
4	7.14e-3	7.59e-3	2.35e-2	3.54e-2	4.55	4.61	3.40	30.22
5	7.07e-3	7.26e-3	1.96e-2	3.19e-2	4.24	4.25	2.96	31.47
6	7.07e-3	7.14e-3	1.73e-2	2.99e-2	3.87	3.89	2.58	29.98

Table 3.3: Error norms and adaptivity statistics for Case 3: the variables are defined in the caption of Table (3.1).

In Table (3.3), L_2 norms of $MSOM$ and $MSAT$, with respect to the reference solution (FM), are tabulated for various times, and the adaptivity statistics in pressure

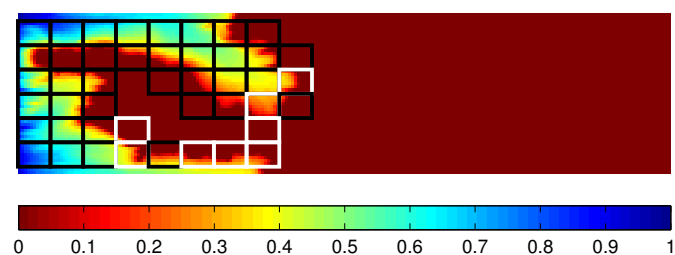
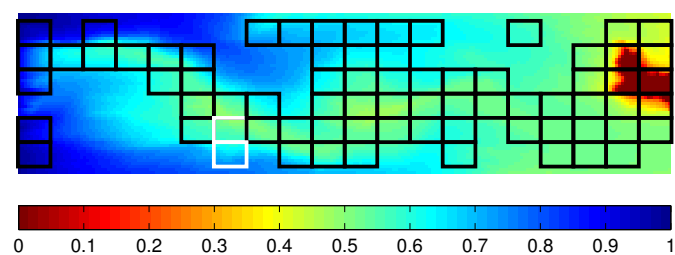
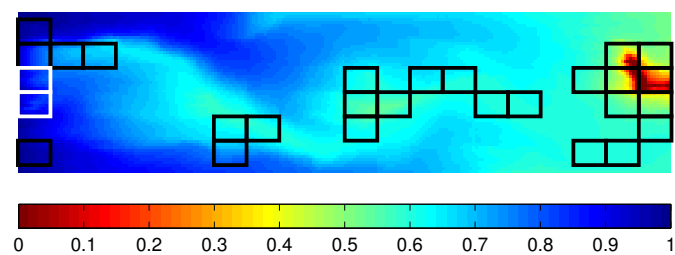
(a) MSAT, $t = \tau_o$ (b) MSAT, $t = 4\tau_o$ (c) MSAT, $t = 6\tau_o$

Figure 3.20: Adaptive saturation computation for three time steps in Case 3: the white and black squares respectively denote the region where Prolongation Operator I and II is applied respectively, at least once, in iterative saturation calculation for this time step.

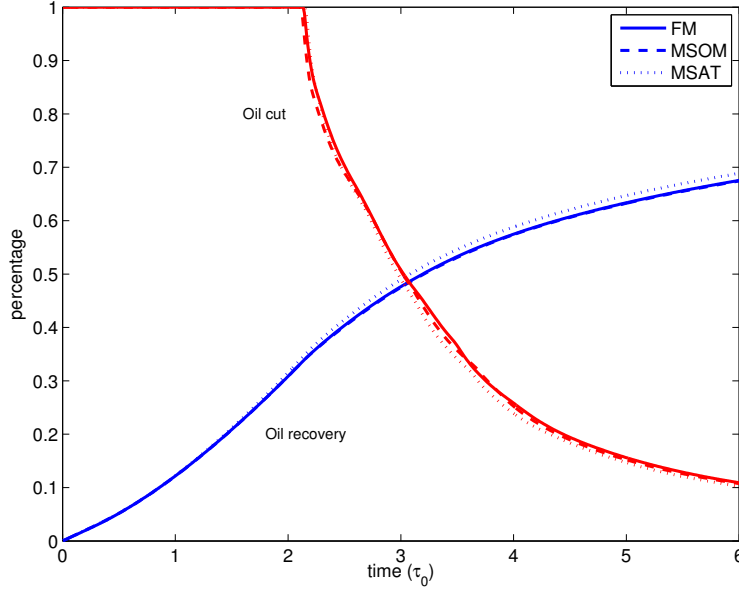


Figure 3.21: Cumulative Oil recovery and oil fraction in production (oil cut) in Case 3

and saturation calculation are presented. Even in this highly heterogeneous problem, the adaptivity ratios of pressure and saturation are not much different from the previous examples. Since the saturation adaptivity requires Prolongation Operator I (expensive Schwarz-overlap method) only for 2-5 % of the domain, the new algorithm (*MSAT*) is significantly more efficient than the original multiscale algorithm (*MSOM*).

3.5.2 More General Problems

In this section, we study more general problems to investigate the accuracy and efficiency of the adaptive multiscale computation of the saturation equations. Three cases will be considered. In the first case, a quarter of a five-spot injection model is studied, where compressibility and gravity effects are included. Similar to the study in Chapter 2, we do not include well models here. The injector and producer are

considered as simple source and sink terms. In the second case we present, the same model is used except that the injector and producer locations are switched after a certain injection period. This case is used to test the robustness of the proposed method when the flow scenario changes during simulation. In the last case, a lock-exchange problem, which is similar to the case studied by [Lunati and Jenny, 2008] is considered. This case is very challenging because the total-velocity is a strong function of the buoyancy forces and accurate computation of both pressure and saturation is crucial.

In all the three cases, the geological model of Case 2 is used, i.e., mildly heterogeneous permeability field in a model with 70×70 fine cells and 10×10 coarse cells. The density of water is 64.0 lbm/ft^3 and that of oil is 32.0 lbm/ft^3 . Both phases are compressible. We define compressibility by $c = \frac{1}{\rho_l} \frac{\partial \rho_l}{\partial p}$. Here, the compressibility of water is $1 \times 10^{-6} \text{ psi}^{-1}$ and that of oil is 5×10^{-5} . A quadratic relative permeability model is used, i.e., $k_{rl} = S_l^2$.

Case 4: Compressible Flow with Gravity

A quarter of a five-spot problem in this two dimensional reservoir model is considered. The initial reservoir pressure is 4000 psi. The injection rate of water is constant at reservoir condition (50 bbl/day) and reservoir fluids are produced at the same rate. The injection and production rates are uniformly distributed in the two corner coarse cells (i.e., injection in the left upper corner and production in the right lower corner). In this case, the two phases have the same viscosity of 1 cp. The same adaptivity thresholds as in Case 2 are used, i.e., $\Delta_1 = 10^{-5}$, $\Delta_2 = 10^{-2}$, $\Delta_v = 0.1$ and $\Delta_\xi = 10^{-3}$.

We directly compare the multiscale solutions of both flow and transport with the fine-scale references. Fig. (3.22) shows the contours of the fine-scale pressure at $t = 0.3, 0.8, 1.5$ PVI (pore volume injected), computed by the reference fine-scale method and our adaptive multiscale formulation. Fig. (3.23) shows the contours of the

fine-scale saturation computed by the reference fine-scale and multiscale approaches. The agreement between the fine-scale and multiscale results is excellent. We also show the various operators used for adaptive computation at three times in Fig. (3.24). Table (3.4) shows the pressure and saturation errors and the adaptivity ratios in the computation of pressure basis functions, total-velocity and saturation.

We notice that the pressure errors are larger than those of Case 2, which is expected, since compressibility and gravity complicate the multiscale computation and more assumptions on the localization boundary conditions are introduced as discussed in the last chapter. Overall, the quality of pressure is still quite good and the saturation errors are about the same as Case 2. Numerical errors in cumulative oil recovery and produced oil fraction are barely noticeable in Fig. (3.25). The behavior of adaptive computation here is also similar to Case 2, while the fraction of Operator I is slightly higher.

Recall that in the multiscale formulation for transport, there is no additional treatment is required for compressibility and gravity. The idea of adaptively choosing prolongation operators in different regions of a transport process is independent of the physics, such as compressibility, gravity and capillary pressure.

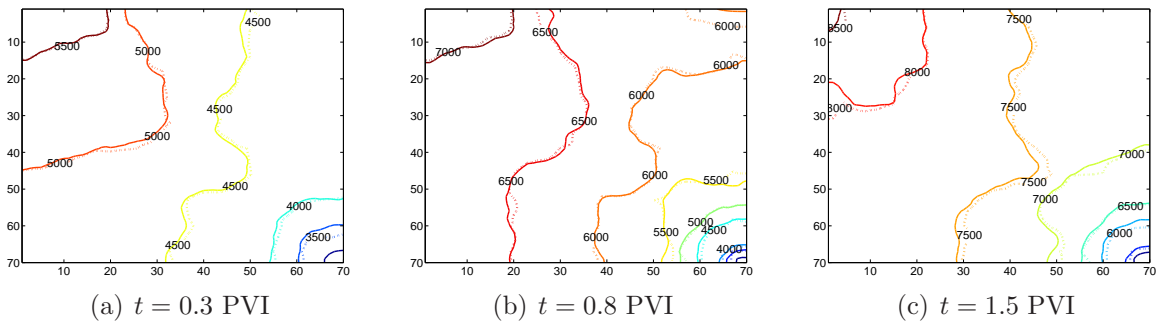


Figure 3.22: Pressure contours of fine-scale and multiscale results at 0.3, 0.8, 1.5 PVI time for a quarter of five-spot injection case. Solid lines denote fine-scale solution and dash lines denote multiscale solution.

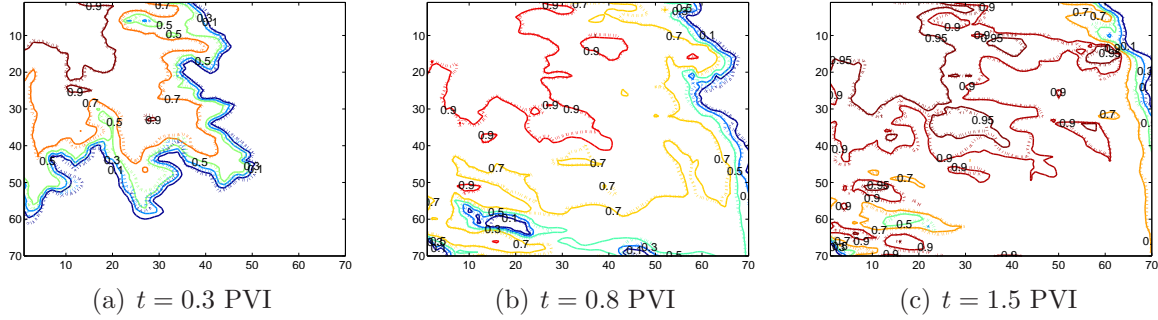


Figure 3.23: Saturation contours of fine-scale and multiscale results at 0.3, 0.8, 1.5 PVI time for a quarter of five-spot injection case. Solid lines denote fine-scale solution and dash lines denote multiscale solution.

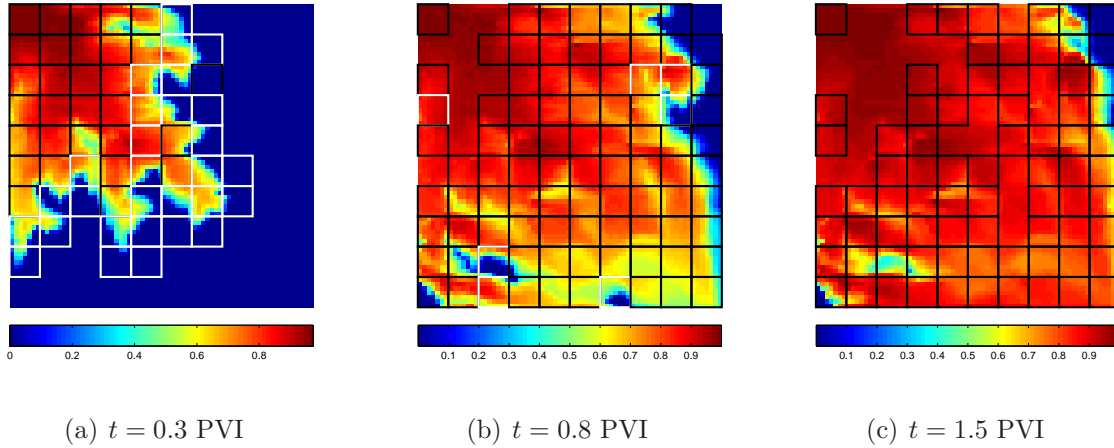


Figure 3.24: Adaptive computation of saturation at 0.3, 0.8, 1.5 PVI time for a quarter of five-spot injection case. The white squares denote the regions where full construction of velocity and saturation (FVFS) is used while the black squares denote the regions where full construction of saturation is obtained using linearly interpolated velocity (AVFS). In regions without squares, direct interpolation of saturation (AS) is applied.

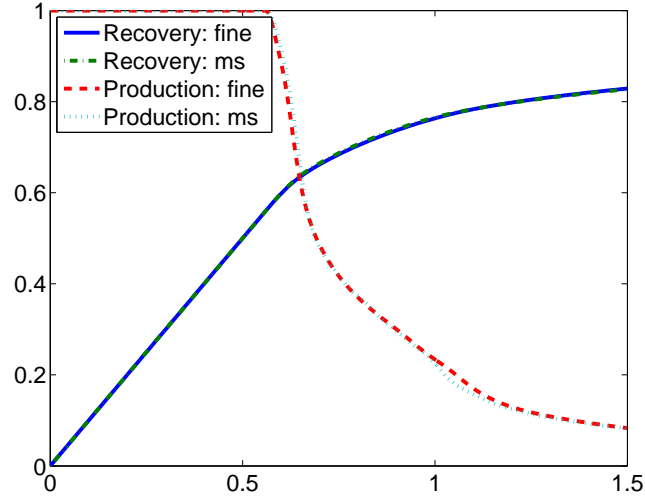


Figure 3.25: Cumulative oil recovery and oil fraction in production for Case 4

t_s (PVI)	e_p	e_s	$f_p(\%)$	$f_I(\%)$	$f_{II}(\%)$
0.1	1.00e-2	1.60e-2	2.80	4.24	2.62
0.3	2.35e-2	5.21e-2	3.02	6.14	6.07
0.5	3.79e-2	5.91e-2	2.94	7.07	10.14
0.8	6.19e-2	3.99e-2	2.48	6.02	15.96
1.0	6.59e-2	3.17e-2	2.15	5.22	18.36
1.5	6.99e-2	2.19e-2	1.56	4.13	21.79

Table 3.4: Statistics of error and ratios of full construction at various time steps for Case 4

Case 5: Switching of injector and producer

In practice, changes in the flow scenario are common due to the opening and closing of wells. When such changes take place, the saturation pattern changes dramatically and the labeling of regions for the purpose of choosing the prolongation operators changes significantly. It is very important for the algorithm to be able to detect such changes automatically and adjust the adaptive computations accordingly. We consider a case where up to 0.75 PVI everything is the same as Case 4, but where at 0.75 PVI, the injection and production wells are switched. There is no special treatment in the code, and thus it is quite interesting to see whether the algorithm can still maintain accuracy.

The pressure and saturation contours at three times after switching the wells are shown in Fig. (3.26) and Fig. (3.27), respectively. The differences between the fine-scale and multiscale results are small, which demonstrates the robustness and accuracy of the adaptive multiscale method for varying and complex flow patterns. Table (3.5) further shows that e_p and e_s are small and do not increase much compared with the previous case. The adaptive computation of saturation for this case is shown in Fig. (3.28). After the flow scenario changes, more regions are computed with full construction of velocity and saturation. However, considering this is a nonlinear problem and several Newton iterations are needed, less complicated computation may be used for the same region in the next iterations. As a result, we notice that the overall fraction of fine-scale construction does not increase much compared with the previous case as shown in Table (3.5). The cumulative oil recovery and produced oil fraction are plotted in Fig. (3.29). The match with the reference solution is excellent for this complex flow pattern.

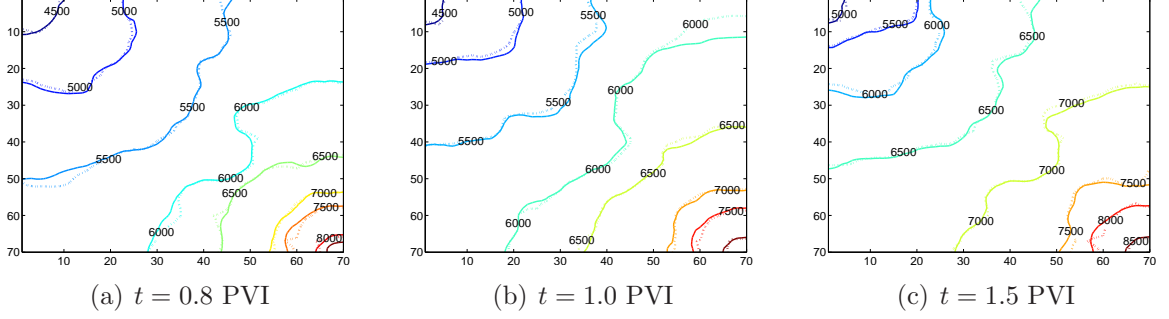


Figure 3.26: Pressure contours of fine-scale and multiscale results at 0.8, 1.0, 1.5 PVI time for a quarter of five-spot injection with switch of injector and producer at 0.75 PVI. Solid lines denote fine-scale solution and dash lines denote multiscale solution.

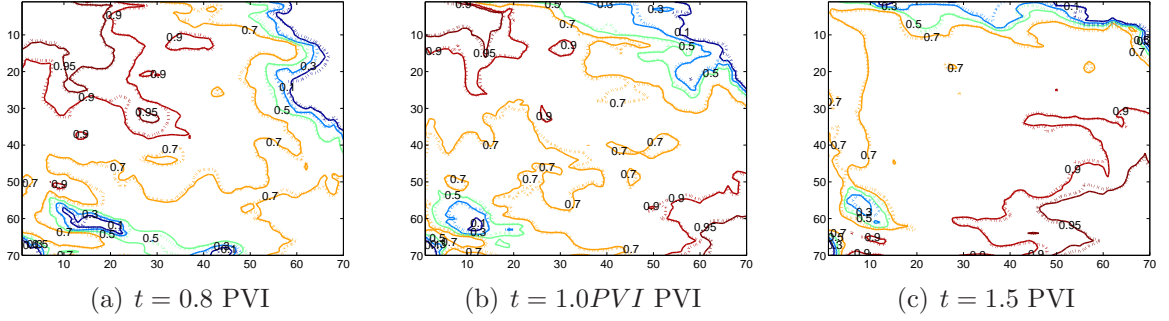


Figure 3.27: Saturation contours of fine-scale and multiscale results at 0.3, 0.8, 1.5 PVI time for a quarter of five-spot injection with switch of injector and producer at 0.75 PVI. Solid lines denote fine-scale solution and dash lines denote multiscale solution.

t_s (PVI)	e_p	e_s	$f_p(\%)$	$f_v(\%)$	$f_s(\%)$
0.1	1.00e-2	1.60e-2	2.80	4.24	2.62
0.3	2.35e-2	5.21e-2	3.02	6.14	6.07
0.5	3.79e-2	5.91e-2	2.94	7.07	10.14
0.8	6.71e-2	3.01e-2	2.56	6.42	15.13
1.0	7.06e-2	2.56e-2	2.58	6.00	16.02
1.5	7.32e-2	3.38e-2	2.46	5.42	18.54

Table 3.5: Statistics of error and fraction of full construction at various time steps for Case 5.

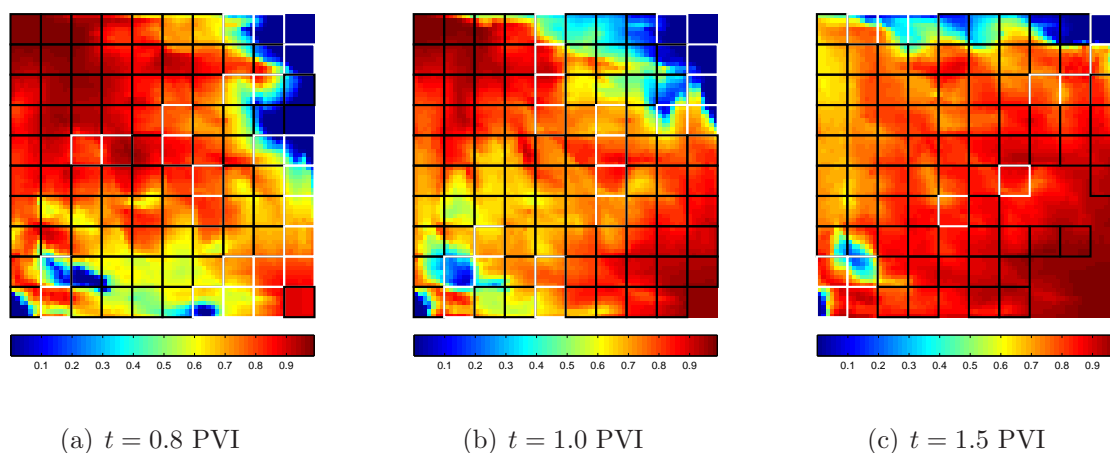


Figure 3.28: Adaptive computation of saturation at three time steps for a quarter of five-spot injection with switch of injector and producer at 0.75 PVI. The squares are defined as in Fig. (3.24).

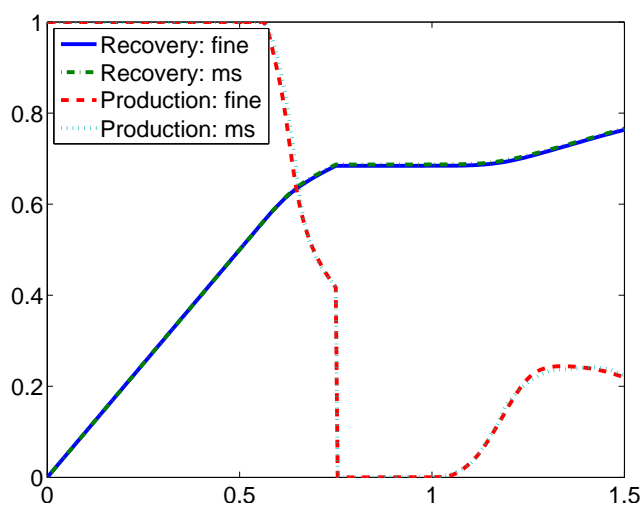


Figure 3.29: Cumulative oil recovery and oil fraction in production for a quarter of five-spot injection with switch of injector and producer at 0.75 PVI.

Case 6: Buoyancy-driven flow

We consider a lock-exchange problem as described in [Lunati and Jenny, 2008]. The left half of the domain is initially saturated with water and the right half with oil. There is no injection or production. The flow and transport are purely driven by the density and viscosity differences. Different from the previous two cases, the oil viscosity is now 5 cp. The viscosity difference results in some interesting phenomena. The displacement of oil by water is unfavorable ($\mu_o/\mu_w > 1$). On the other hand, the displacement of water by oil is favorable and the oil gravity-current is sharp.

The accuracy of the total-velocity distribution is critical in this case. Also, since the total velocity is a strong function of the density difference of the two phases, saturation changes result in total-velocity changes. Thus, a tight tolerance for the full velocity construction criterion is used, namely $\Delta_v = 10^{-3}$.

Figs. (3.30 – 3.31) are the pressure and saturation contours at three times. Adaptive multiscale computation shows good accuracy for both pressure and saturation. Both the sharp oil invasion front and the spreading water invasion front are accurately resolved. The characteristic time τ , which is cited in the figures, is defined as

$$\tau = \frac{\phi\mu_o H}{g(\rho_w - \rho_o)\bar{k}}, \quad (3.33)$$

where \bar{k} is the median value of permeability.

Adaptivity of the saturation computations is shown in Fig. (3.32). Notice that no AVFS operator is used. The reason is that the total velocity is sensitive to saturation changes. Consequently, small tolerance of Δ_v rules out the use of an approximate velocity reconstruction when full reconstruction is required for the fine-scale saturation. Table (3.6) indicates that the overall percentage of full reconstruction of both velocity and saturation is quite small. On the other hand, the fraction of pressure basis function updates increases, which is due to the strong changes in the total mobility

field.

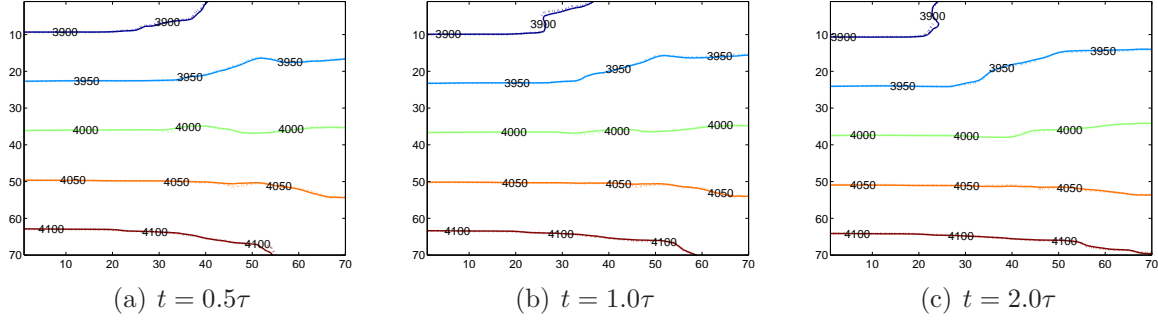


Figure 3.30: Pressure contours of fine-scale and multiscale results at $0.5\tau, 1.0\tau, 2.0\tau$ PVI time for buoyancy-driven flow. Solid lines denote fine-scale solution and dash lines denote multiscale solution.

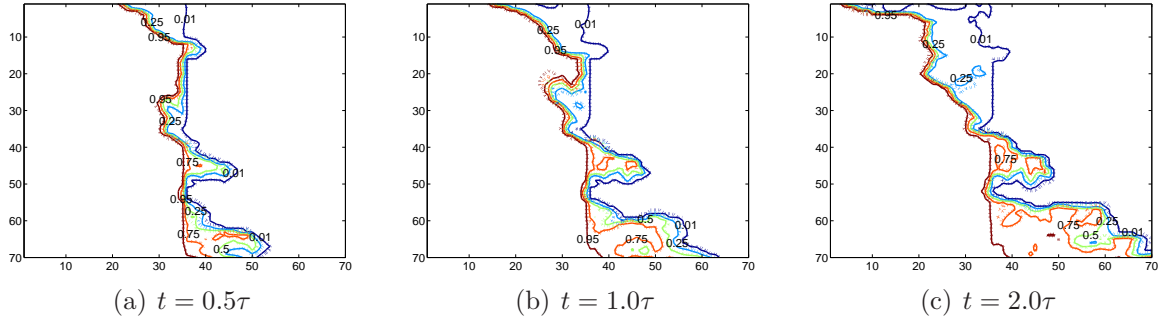


Figure 3.31: Saturation contours of fine-scale and multiscale results at $0.5\tau, 1.0\tau, 2.0\tau$ PVI time for buoyancy-driven flow. Solid lines denote fine-scale solution and dash lines denote multiscale solution.

3.5.3 Efficiency Study

3-Dimensional Models

In order to examine CPU improvement by the new adaptive transport algorithm (MSAT), we constructed two 3-dimensional models with 97,200 ($45 \times 45 \times 48$) and 995,328 cells ($144 \times 144 \times 48$). Permeability fields are generated by the sequential

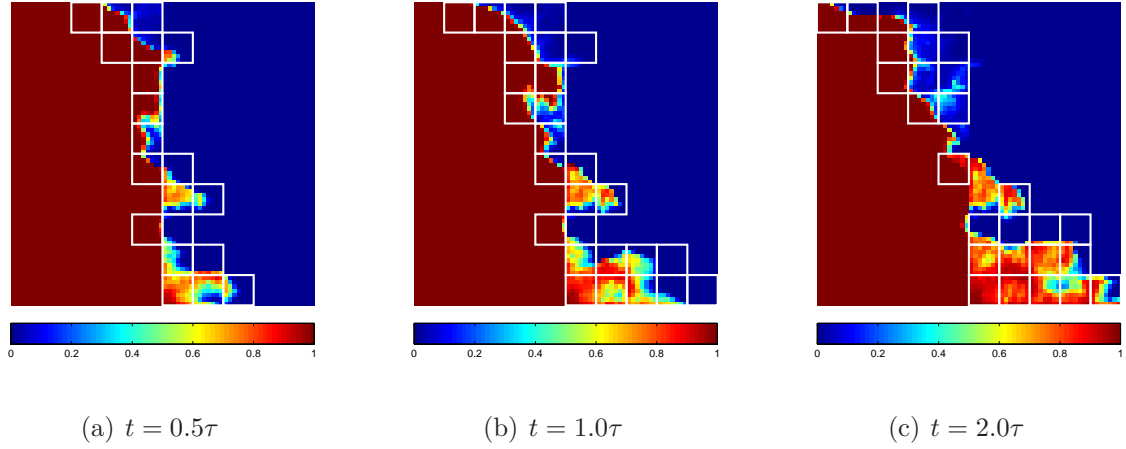


Figure 3.32: Adaptive computation of saturation at three time steps for buoyancy-driven flow. The squares are defined as in Fig. (3.24).

$t_s (\tau)$	e_p	e_s	$f_p(\%)$	$f_I(\%)$	$f_{II}(\%)$
0.2	1.62e-4	1.74e-2	11.28	9.65	0
0.5	1.63e-4	3.68e-2	12.55	7.41	0
0.8	1.49e-4	4.45e-2	11.67	8.07	0
1.0	1.61e-4	4.75e-2	11.33	8.33	0
1.5	1.44e-4	4.87e-2	11.06	8.86	0
2.0	1.46e-4	4.80e-2	11.43	8.95	0

Table 3.6: Statistics of error and fraction of full construction at various time steps for buoyancy-driven flow.

Gaussian simulation method [Deutsch and Journel, 1998]. The logarithm of permeability has a Gaussian histogram with a mean of 50 md and a standard deviation of 1.5. The permeability map for the smaller grid is shown in Fig. (3.33). The permeability for the larger grid is quite similar. The same coarse grid of $9 \times 9 \times 6$ is used for these two models. The CPU times for 0.6 PVI are shown in Table (3.5.3).

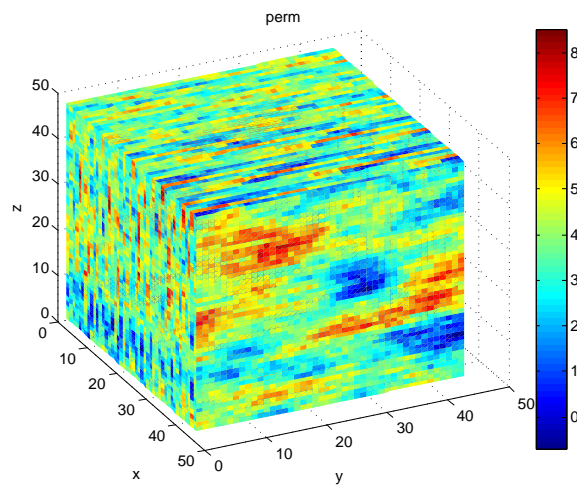


Figure 3.33: Logarithmic permeability for the fine grid of size $45 \times 45 \times 48$

For the small model with 97,200 cells, the original MSFV (MSOM) and the MSFV with adaptive transport algorithm (MSAT) reduced CPU by 48 % and 61 %, respectively, over the fine-grid simulation. Furthermore, for the large model with 995,328 cells, the CPU improvement becomes very significant; 83 % CPU reduction by MSOM and 92 % CPU reduction by MSAT. The numerical efficiency improvements by MSFV are naturally problem-dependent. As the model size becomes large, we expect MSOM and MSAT to speed up simulation runs drastically. We also note that for the large 3-D model, the multiscale computation with adaptive transport algorithm can improve numerical efficiency by a factor of two, or more, over the original multiscale method.

number of cells	97,200	995,328
fine-scale (FM) CPU (min)	25.6	1618.7
original MS (MSOM) CPU (min)	13.3	281
adaptive MS (MSAT) CPU (min)	10.1	133

Table 3.7: CPU comparisons for 3D models at $t = 0.6PVI$.

Effects of Transport Adaptivity Thresholds

As the computational complexity analysis on Section (3.4.2) shows, the efficiency of adaptive multiscale transport computation relies strongly on the fractions of the primal cells that apply FVFS and AVFS operators. The smaller the fractions of the two operators, the more efficient the adaptive multiscale transport computations are. A rough estimation of the relationship between the computational efficiency and the fractions is given by Eq. (3.29).

The fraction of an operator applied during a computation is determined by the adaptivity thresholds, such as Δ_1 , Δ_2 , Δ_v and Δ_ϵ . Larger threshold values lead to better efficiency, but the accuracy may deteriorate. Therefore, we revisit Case 4, which represents a class of problem commonly encountered in reservoir simulation practice (i.e., slightly compressible with the presence of appreciable gravity in viscous forces). We investigate the influence of transport adaptivity thresholds on the computational efficiency and accuracy.

Three groups of adaptivity threshold values are used as listed in Table (3.8). The first group represents the usage of tight tolerance. Group three, on the other hand, adopts larger threshold values. The second group uses values in between the other two groups.

The pressure and saturation errors and the fractions of Operator I and Operator II for the three groups of adaptivity thresholds are shown in Table (3.9) for several times. These results indicate that while the fraction of full construction (FVFS or

	Δ_1	Δ_2	Δ_v	Δ_ξ
Group 1 (tight)	10^{-5}	0.01	0.1	10^{-3}
Group 2 (medium)	5×10^{-4}	0.05	0.2	5×10^{-3}
Group 3 (loose)	10^{-4}	0.1	0.5	0.01

Table 3.8: Groups of transport adaptivity thresholds

AVFS) is quite sensitive to the thresholds, the three threshold groups have comparable accuracy in pressure and saturation. This implies that for this case a relatively loose adaptivity tolerance can yield quite accurate results, while achieving high efficiency.

time	Group 1				Group 2				Group 3			
PVI	e_p	e_s	f_I	f_{II}	e_p	e_s	f_I	f_{II}	e_p	e_s	f_I	f_{II}
0.1	1.00	1.60	4.24	2.62	1.27	1.63	2.78	1.39	1.28	1.83	1.55	2.70
0.5	3.79	5.91	7.07	10.14	4.55	5.99	5.14	6.67	4.56	6.04	2.98	9.14
0.8	6.19	3.99	6.02	15.96	7.14	4.04	4.93	10.78	7.59	4.14	2.99	12.45
1.0	6.59	3.17	5.22	18.36	7.13	3.27	4.41	12.37	7.23	3.22	2.85	13.41
1.5	6.99	2.19	4.13	21.79	7.26	2.23	3.74	13.79	7.35	2.54	2.53	13.75

Table 3.9: Statistics of error and ratios of full construction at various time steps for three groups of adaptivity thresholds. The values for e_p , e_s , f_I and f_{II} in the table denote percentages (i.e., 1.27 means 1.27%).

The adaptive computation of transport at $t = 0.8$ PVI is shown in Fig. (3.34) for the three groups of adaptive thresholds. The saturation results are quite close for the three threshold groups. However, the third group is very aggressive in using the most efficient AS operator. The second group adopts a strategy that lies between the first and last groups, which is also consistent with the fractions of operators as reported in Table (3.9).

Our numerical experience indicates that the proposed adaptivity criteria are quite robust for a wide range of reservoir simulation problems. For some challenging cases (e.g., gravity segregation problems), special care may be necessary and a trial and error approach may be taken. The threshold values in Table (3.8) could serve as a starting point. We can also get a reasonable initial guess of the thresholds based on

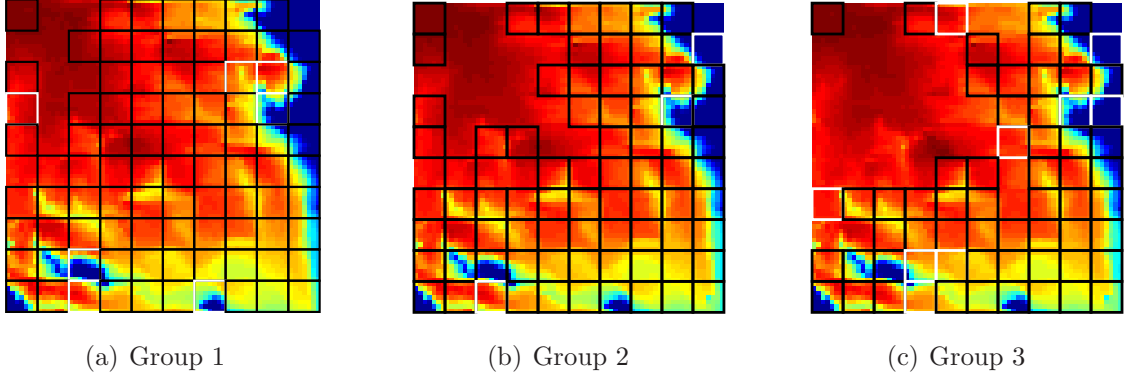


Figure 3.34: Adaptive computation of saturation at 0.8 PVI for three groups of adaptive thresholds. The white squares denote the regions where full construction of velocity and saturation (FVFS) is used while the black squares denote the regions where full construction of saturation is obtained using linearly interpolated velocity (AVFS). In regions without squares, direct interpolation of saturation (AS) is applied.

the physical behavior of a problem. For instance, in Case 6 where gravity is dominant and strong counter-current flow of the two phases exists, it would be a good idea to use a tight tolerance for interpolating velocity (i.e., small Δ_v).

3.6 Conclusions

The focus of this chapter was the development of an adaptive multiscale finite-volume formulation for solving the nonlinear multiphase transport problem (i.e., saturation equations). An algebraic formulation is used, such that both flow and transport are solved in one general multiscale framework.

The transport equations for saturation are nonlinear and hyperbolic; as a result, the prolongation operator for saturation cannot, in general, be formulated via generic basis functions as for the pressure equation. We adopted a conservative restriction operator (i.e., the finite-volume restriction operator) and proposed three adaptive prolongation operators to deal with the saturation field. At a given time, different

saturation prolongation operators are used based on the region a (primal) coarse block belongs to. Specifically, for the time interval of interest, the physical domain is divided into three distinct regions: (1) Region 1, where the injection fluid has not yet invaded the cell, (2) Region 2, where an injection front encroached and the saturation of the injection fluid increases rapidly, and (3) Region 3, where the saturation changes slowly after the sharp front has moved through. Simple threshold criteria were proposed to identify the transitions between the various regions. In Region 1, the transport computations can be completely skipped; whereas in Regions 2, the FVFS (full velocity-full saturation) operator is used, which reconstructs a conservative fine-scale velocity and solves for the fine-scale saturation. Finally for Region 3, we developed two efficient approximate prolongation operators: the AVFS (approximate velocity-full saturation) operator that approximates the fine-scale velocity and then solves for the fine-scale saturation, and the AS (approximate saturation) operator, which directly approximates the fine-scale saturation from the coarse-scale saturation. We devised a criterion for choosing between the AVFS and AV operators in Region 3.

The adaptive multiscale method for flow and transport was tested using a series of models with different permeabilities (homogeneous and heterogeneous) and boundary conditions (no-flow and Dirichlet). Challenging cases with additional physical mechanisms, such as compressibility and gravity, and changing well locations were also investigated using the multiscale formulation. It was demonstrated that the results obtained with adaptive multiscale computations of flow and transport are in excellent agreement with the reference fine-scale solutions.

Computational complexity analysis reveals that the adaptive multiscale formulation of transport is significantly more efficient than the original multiscale finite-volume method that entails full construction of both velocity and saturation fields on the fine scale. The computational times for large three-dimensional problems show

clearly that the multiscale formulation of coupled flow and transport is much more efficient than the original multiscale finite-volume method, which is already significantly more efficient than state-of-the-art fine-scale methods.

The efficiency of multiscale modeling of transport is strongly related to the adaptivity thresholds. The choice of these thresholds is problem dependent. For common flow and transport problems in reservoir simulation practice (i.e., slightly compressible, viscous dominated displacements), the accuracy of multiscale modeling is weakly dependent on the thresholds. We suggested threshold values for various transport problems.

Chapter 4

Two-Stage Algebraic Multiscale Solver

4.1 Introduction

In Chapters 2 and 3, we described a multiscale finite-volume framework for coupled flow and transport in heterogeneous porous media. The accuracy and efficiency of the proposed multiscale method have been demonstrated for a wide range of problems with strongly heterogeneous permeability and complex physics. We also showed that the MsFVM and OBMM show large errors for cases with channelized permeability and high anisotropy ratios in the transmissibility. In this chapter, we develop an efficient Two-stage Algebraic Multiscale Solver (TAMS) that overcomes these limitations. The TAMS is based on the same algebraic multiscale framework used in Chapters 2 and 3. The TAMS is purely algebraic and converges to the fine-scale solution for general elliptic flow equations.

Hajibeygi et al. [2008] proposed an iterative multiscale finite-volume (i-MSFV) method. They showed that the multiscale solution converges to the fine-scale solution iteratively when the local boundary conditions are updated with global information

in each iteration. In their approach, the global information was obtained by applying several smoothing steps (line relaxation is used) after a multiscale solution step. The global information was then used to solve local correction functions.

We use the algebraic multiscale framework as part of a preconditioning strategy to solve the elliptic flow problem in highly heterogeneous domains. A preconditioner M of a matrix A is a matrix such that $M^{-1}A$ has a smaller condition number than A and hence converges faster for an iterative linear solver than the original matrix. Among numerous preconditioners, domain decomposition is a class of methods of particular interest mainly due to its efficiency and parallelism [Smith et al., 1996; Toselli and Wildlund, 2005]. Aarnes and Hou [2002] used the multiscale finite element method as the coarse grid solver of their non-overlapping domain decomposition preconditioner. Analysis on how the condition number of the preconditioner depends on the variable coefficients was reported by Graham et al. [2007]. They showed that using the multiscale finite element method as the coarse solver results in better convergence than using linear or polynomial finite element methods. However, the multiscale finite element method does not possess the nice property of local mass conservation, which is quite important for solving subsurface transport problems. As a result, a converged solution (i.e., very small residual and error tolerances) must be achieved in solving the pressure field in order to avoid large errors and convergence problems when solving the nonlinear (hyperbolic) transport equations.

Our purpose in this chapter is twofold: 1) construct an efficient multiscale preconditioner for linear pressure systems that converges to the fine-scale solution; 2) guarantee a locally conservative solution after any iteration (i.e., before full convergence is achieved). The focus of this chapter is on the elliptic flow problem (i.e., incompressible multiphase flow).

We propose a flexible Two-stage Algebraic Multiscale Solver (TAMS). In the first stage, a multiscale solution is constructed purely algebraically from the finite-volume

approximation of the fine-scale system. This step follows the operator-based multiscale method (OBMM) [Zhou and Tchelepi, 2008], as discussed in detail in Chapter 2, which is an algebraic representation of the original multiscale finite-volume method [Jenny et al., 2003]. Here, we further extend the OBMM by constructing a prolongation operator algebraically and directly from a wirebasket ordered [Smith et al., 1996] reduced system. Spectral analysis shows that the multiscale solution step captures the low-frequency spectra of the system very well, but misses some high-frequency errors. Therefore, a second stage is required to deal with those high-frequency error components. We consider Block ILU(0) (BILU) and Additive Schwarz (AS) as second-stage local preconditioners. The TAMS represents the full spectra very well and is able to converge fast. We also show a simple process that allows for the reconstruction of a locally conservative fine-scale velocity field. Compared with the i-MSFV method in Hajibeygi et al. [2008], no correction functions are needed in the TAMS, and the second stage preconditioner is applied only once per iteration.

This chapter is organized as follows. In Section 4.2, we develop an Algebraic Multiscale Solver (AMS) that constructs the prolongation operator directly from the fine-scale matrix and can be applied as a general iterative solver. In Section 4.3, we present the Two-stage Algebraic Multiscale Solver (TAMS). Spectral analysis is used to show that the two-stage method can resolve the full spectra of the fine-scale matrix and achieve fast convergence. It is also demonstrated that the TAMS allows for the reconstruction of a locally conservative fine-scale velocity field. In Section 4.4, we first study the convergence and conservation properties of TAMS with two-dimensional numerical examples; then challenging three-dimensional problems with complex heterogeneous structures and high aspect ratios are used to investigate the efficiency and scalability of TAMS.

4.2 Algebraic Multiscale Solver(AMS)

Recall that the multiscale solution of pressure obtained from OBMM can be written as

$$\mathbf{p}^{ms} = \mathcal{P} (\mathbf{A}^c)^{-1} \mathbf{q}^c \equiv \mathcal{P}(\mathcal{R}\mathbf{A}\mathcal{P})^{-1} \mathcal{R}\mathbf{q}. \quad (4.1)$$

If we employ the multiscale method as a preconditioner for an iterative linear solver, we can write

$$M_{ms}^{-1} = \mathcal{P}(\mathcal{R}\mathbf{A}\mathcal{P})^{-1} \mathcal{R}, \quad (4.2)$$

where M_{ms} is the multiscale preconditioner. The preconditioner in Eq. (4.2) is not purely algebraic in the sense that one has to construct local systems to solve for the basis function and then construct the prolongation operator, \mathcal{P} . This approach involves assembly and solution of local systems for each dual cell and requires full access to all the physical quantities (e.g., mobilities, grid information, etc.). Moreover, when the grid gets more complex (i.e., irregular, unstructured), the construction and assembly would also get complicated.

Here, we use a purely algebraic approach to construct the prolongation operator directly from the given fine-scale coefficient matrix. The AMS can then be used in conjunction with iterative schemes, such as Krylov methods to accelerate the convergence.

Nordbotten and Bjørstad [2008] discussed the relationship between the multiscale finite-volume method and non-overlapping domain decomposition preconditioners that employ various approximations of the Schur complement of the original matrix. They showed that the multiscale finite-volume method is equivalent to the tangential component approximation [Cai et al., 1992] with no source terms. In the tangential approximation, only fluxes tangential to the interfaces are considered. Here, we construct the prolongation operator using a reduced system of the original

fine-scale system that is obtained using the tangential approximation.

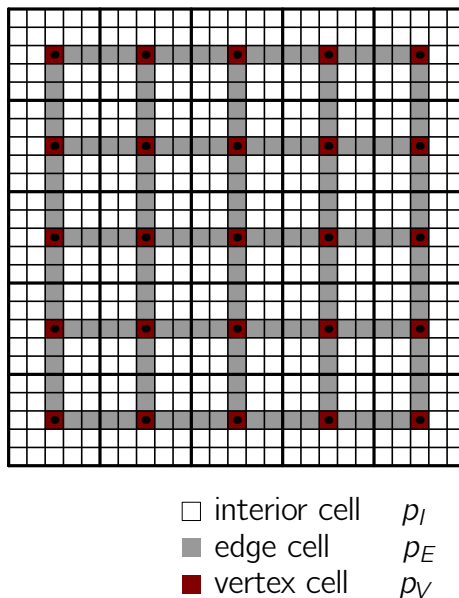


Figure 4.1: The multiscale grid with the wirebasket ordering

We proceed by first introducing a wirebasket ordering of the original system [Smith et al., 1996]. We note that Wallis and Tchelepi [2007] employed the wirebasket ordering to derive an algebraic cascading class linear solver for solving elliptic pressure equations in both structured and unstructured grids. However, their approach does not ensure mass conservation and must achieve a converged solution, as with the non-overlapping domain decomposition preconditioners by Aarnes and Hou [2002] and Graham et al. [2007]. On the other hand, our objective here is to develop an efficient solver that ensures local mass conservation.

With the wirebasket ordering, the fine cells in two-dimensional problems are grouped into three separate categories: interior, edge and vertex cells as indicated in Fig. (4.1). The labeling is with respect to the dual grid (refer to Fig. (2.1)). In three dimensional problems, we need to introduce face cells. The edge and face cells are referred to as interfaces, which are usually lumped together. In the derivation

of this section, we focus on two-dimensional problems only. The extension to three-dimensional problems is straightforward, and one only needs to substitute the edge cells by a group of edge and face cells.

The wirebasket ordered system of the original matrix can be written as

$$\begin{bmatrix} A_{II} & A_{IE} & 0 \\ A_{EI} & A_{EE} & A_{EV} \\ 0 & A_{VE} & A_{VV} \end{bmatrix} \begin{bmatrix} p_I \\ p_E \\ p_V \end{bmatrix} = \begin{bmatrix} q_I \\ q_E \\ q_V \end{bmatrix}. \quad (4.3)$$

The reduced boundary condition in Eq. (2.23) ignores flow between edge and interior cells, which is also equivalent to the tangential approximation discussed by Nordbotten and Bjørstad [2008]. Using the reduced boundary condition (Eq. (2.23)) with Eq. (4.3) leads to the following “reduced” system

$$\begin{bmatrix} A_{II} & A_{IE} & 0 \\ 0 & \tilde{A}_{EE} & A_{EV} \\ 0 & A_{VE} & A_{VV} \end{bmatrix} \begin{bmatrix} p_I \\ p_E \\ p_V \end{bmatrix} = \begin{bmatrix} 0 \\ 0 \\ q_V \end{bmatrix}, \quad (4.4)$$

where \tilde{A}_{EE} is the diagonal matrix associated with the tangential flow only, i.e., $\tilde{A}_{EE}p_E + A_{EV}p_V = 0$ describes the tangential flow equations for the edge cells. Also note that the right-hand-sides of the interior and edge equations are neglected in the reduced system (Eq. (4.4)), which is consistent with Eq. (2.23). We solve the edge equations first and then the interior equations from Eq. (4.4), i.e.,

$$\begin{aligned} p_E &= -\tilde{A}_{EE}^{-1} A_{EV} p_V, \\ p_I &= -A_{II}^{-1} A_{IE} p_E = A_{II}^{-1} A_{IE} \tilde{A}_{EE}^{-1} A_{EV} p_V, \end{aligned} \quad (4.5)$$

or,

$$\begin{bmatrix} p_I \\ p_E \\ p_V \end{bmatrix} = \begin{bmatrix} A_{II}^{-1} A_{IE} \tilde{A}_{EE}^{-1} A_{EV} \\ -\tilde{A}_{EE}^{-1} A_{EV} \\ I_{VV} \end{bmatrix} p_V, \quad (4.6)$$

where I_{VV} is an identity matrix of dimension $n_c \times n_c$, where n_c is the number of vertices. Notice that a vertex cell is also the center of a primal coarse cell, and thus p_V is equivalent to the coarse-scale pressure \mathbf{p}^c in MsFVM. We denote the permutation matrix of the wirebasket ordering as G , so that

$$\mathbf{p}^f = G \begin{bmatrix} p_I \\ p_E \\ p_V \end{bmatrix}. \quad (4.7)$$

Combining Eq. (4.6) and (4.7), one obtains

$$\mathbf{p}^f = G \begin{bmatrix} A_{II}^{-1} A_{IE} \tilde{A}_{EE}^{-1} A_{EV} \\ -\tilde{A}_{EE}^{-1} A_{EV} \\ I_{VV} \end{bmatrix} \mathbf{p}^c, \quad (4.8)$$

which defines the prolongation operator as

$$\mathcal{P} = G \begin{bmatrix} A_{II}^{-1} A_{IE} \tilde{A}_{EE}^{-1} A_{EV} \\ -\tilde{A}_{EE}^{-1} A_{EV} \\ I_{VV} \end{bmatrix}. \quad (4.9)$$

Note that in Eq. (4.9), A_{II}^{-1} and \tilde{A}_{EE}^{-1} are computed for each interior region and edge independently. In other words, the construction of the prolongation operator based on Eq. (4.9) can be perfectly localized, which is computationally efficient and amenable to parallel computation.

In summary, the AMS constructs a prolongation operator from Eq. (4.9) and then obtains the multiscale solution using Eq. (2.21) or (4.2). All the procedures are purely algebraic and only the fine-scale system and information on the wirebasket ordering are needed.

4.3 Two-Stage Algebraic Multiscale Solver

The AMS derived in the previous section is a pure algebraic representation of the multiscale finite-volume method if the finite-volume type restriction operator is used. In the AMS, one also has the flexibility to employ a Galerkin type restriction operator. Next, we investigate the convergence behavior of the AMS through spectral analysis, which motivates the two-stage algebraic multiscale solver (TAMS). We also show that the TAMS allows for the reconstruction of a locally conservative fine-scale velocity field after any iteration. This is an important property that enables us to apply the TAMS as an efficient and locally mass conservative approach to compute approximate solutions of large-scale heterogeneous problems.

4.3.1 Convergence Analysis of AMS

If we apply the AMS as a preconditioner for a Richardson iterative scheme with a damping factor of unity, the procedure can be written as

$$p^{\nu+1} = p^\nu + M_{ms}^{-1} r^\nu, \quad (4.10)$$

where ν is the iteration number, p^ν and r^ν denote the pressure and residual at iteration ν , respectively. The residual is given by

$$r^\nu = q - Ap^\nu. \quad (4.11)$$

The error vector, $\epsilon^\nu = p^\nu - p^f$, satisfies

$$\epsilon^{\nu+1} = (I - M_{ms}^{-1}A)\epsilon^\nu. \quad (4.12)$$

The iteration matrix is defined by

$$I_{ms} \equiv I - M_{ms}^{-1}A. \quad (4.13)$$

The sufficient and necessary condition for convergence is that the spectral radius of the AMS iteration matrix defined in Eq. (4.13) should be less than 1.

Lemma 1. *The iteration matrix I_{ms} of AMS has eigenvalue 1 of multiplicity no less than $n_f - n_c$.*

Proof. We know for general matrices C and D

$$\text{rank}(CD) \leq \min(\text{rank}(C), \text{rank}(D)).$$

From the construction of the restriction and prolongation operators, $\text{rank}(\mathcal{P}) = \text{rank}(\mathcal{R}) = n_c$. Therefore, based on Eq. (4.2), we immediately conclude that

$$\text{rank}(M_{ms}^{-1}) \leq n_c.$$

With the same argument

$$\text{rank}(M^{-1}A) \leq n_c,$$

which is equivalent to

$$\dim \text{Ker}(M^{-1}A) \geq n_f - n_c,$$

where $\text{Ker}(\cdot)$ denotes the kernel, or null space, of a matrix. We know $\forall x \in \text{Ker}(M^{-1}A)$, x is also an eigenvector of $M^{-1}A$ corresponding to eigenvalue 0. Therefore, $M^{-1}A$ has

eigenvalue 0 of multiplicity not less than $n_f - n_c$. In other words, I_{ms} has eigenvalue 1 of multiplicity not less than $n_f - n_c$. \square

Based on **Lemma (1)** and its proof, we see that AMS does not ensure convergence as a general linear preconditioner due to the null space of M_{ms}^{-1} . We can also understand the convergence behavior of AMS from **Lemma (2)**.

Lemma 2. *According to Eq. (4.10), $p^{\nu+1} = p^\nu$ holds for $\nu \geq 1$ and any given initial pressure $p^{(0)}$.*

Proof. Since $M_{ms}^{-1} = \mathcal{P} \mathbf{A}^c \mathcal{R}$, from Eq. (4.10), if we show $\mathcal{R}r^\nu = 0$ for $\nu = 1$, it follows that $p^{\nu+1} = p^\nu$ for $\nu \geq 1$. We start from

$$r^{(1)} = f - Ap^{(1)} = (f - Ap^{(0)}) - AM_{ms}^{-1}(f - Ap^{(0)}). \quad (4.14)$$

Note that

$$\mathcal{R}AM_{ms}^{-1} = \mathcal{R}A(\mathcal{P}(\mathbf{A}^c)^{-1}\mathcal{R}) = (\mathcal{R}A\mathcal{P})(\mathbf{A}^c)^{-1}\mathcal{R} = \mathcal{R}. \quad (4.15)$$

Thus, applying \mathcal{R} on both sides of Eq. (4.14) gives

$$\mathcal{R}r^{(1)} = 0, \quad (4.16)$$

which leads to $p^{\nu+1} = p^\nu$ for $\nu \geq 1$. \square

Lemma (2) shows that the Richardson iterative procedure with the AMS preconditioner should stop after one iteration, since no further change in the residual will take place with more iterations. Generally, a single-iteration will not converge to the fine-scale solution because the prolongation operator is constructed based on an approximate “reduced” system.

We now show an example of a simple two-dimensional flow problem without compressibility, or gravity. In this problem, the fine grid is 40×40 and the coarse grid is

4×4 , i.e., the coarsening ratio is 10×10 . The permeability is isotropic and homogeneous: $k_x = k_y = 1$ and no-flow boundary conditions are specified. Pressure is fixed in cells $(1, 2)$ and $(40, 40)$ with values of 1 and 0, respectively. The finite-volume type restriction operator is used to construct AMS. The spectra of the iteration matrix are shown in Fig. (4.2), which shows that the spectra of the AMS iteration matrix cluster around 0 and 1. Actually the eigenvalue 1 is of multiplicity $n_f - n_c$, which is caused by the rank deficiency of M_{ms}^{-1} as shown in **Lemma (1)**. However, it is quite encouraging that all the other spectra are clustered around 0, which means AMS represents the remaining part of the spectrum very well.

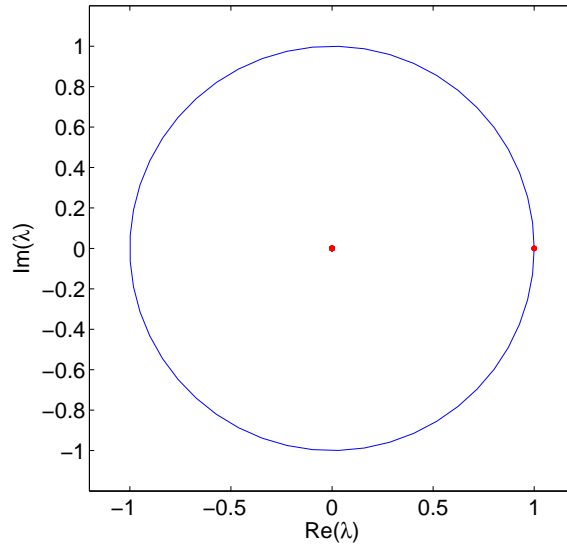


Figure 4.2: The full spectra of the iteration matrix of AMS (denoted by dots) for an isotropic homogeneous case.

We also show the eigenfunctions of the AMS iteration matrix associated with the largest (unity) and smallest (zero) eigenvalues in Fig. (4.3). Clearly, the missing spectra (associated with eigenvalue 1) represent high frequency errors. On the other hand, AMS perfectly resolves the low frequency error components (associated with eigenvalue 0).

Figures (4.4) and (4.5) compare the eigenvectors associated with the highest and

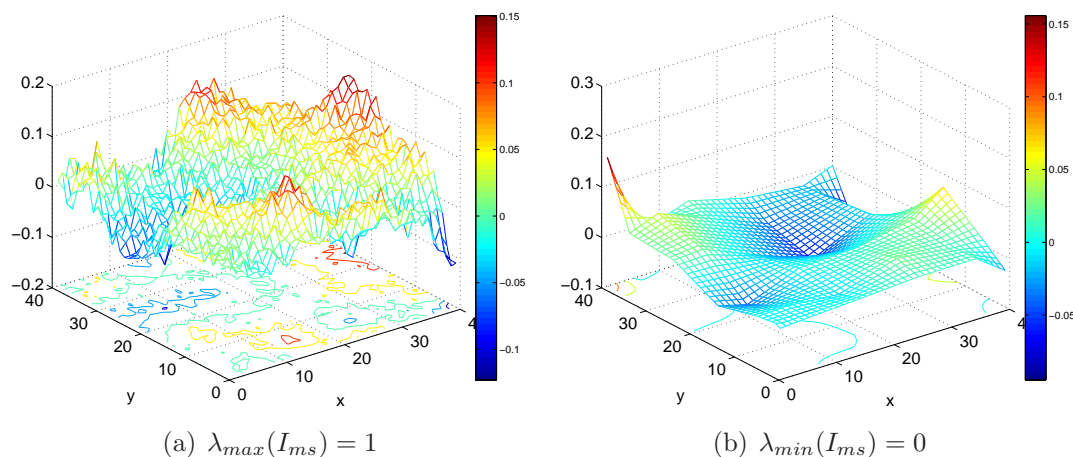


Figure 4.3: Eigenvectors of AMS iteration matrix that are associated with the largest and smallest eigenvalues (1 and 0, respectively).

lowest frequencies of A^{-1} and M_{ms}^{-1} . These figures confirm that the AMS represents the low frequency spectra of the fine-scale matrix very well, but that it misses some of the high frequency components.

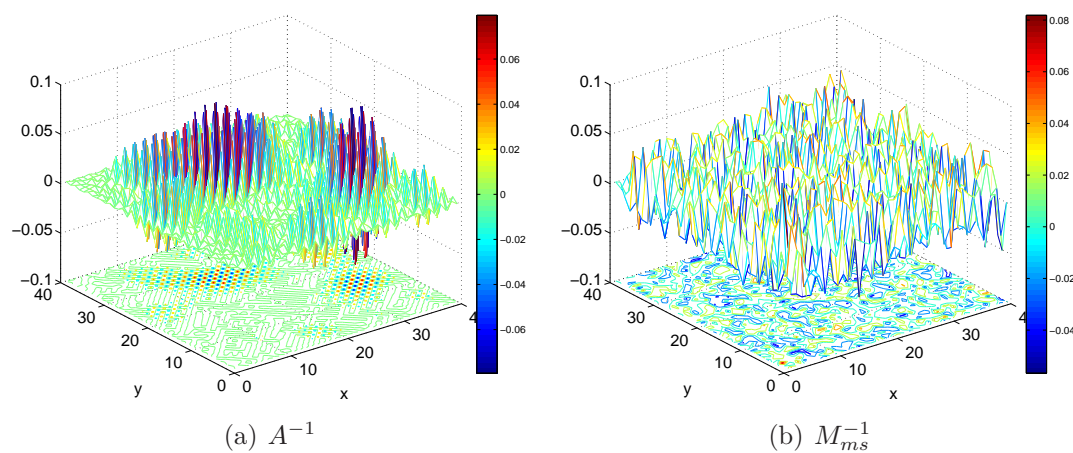


Figure 4.4: Eigenvectors of A^{-1} and M_{ms}^{-1} with the highest frequency.

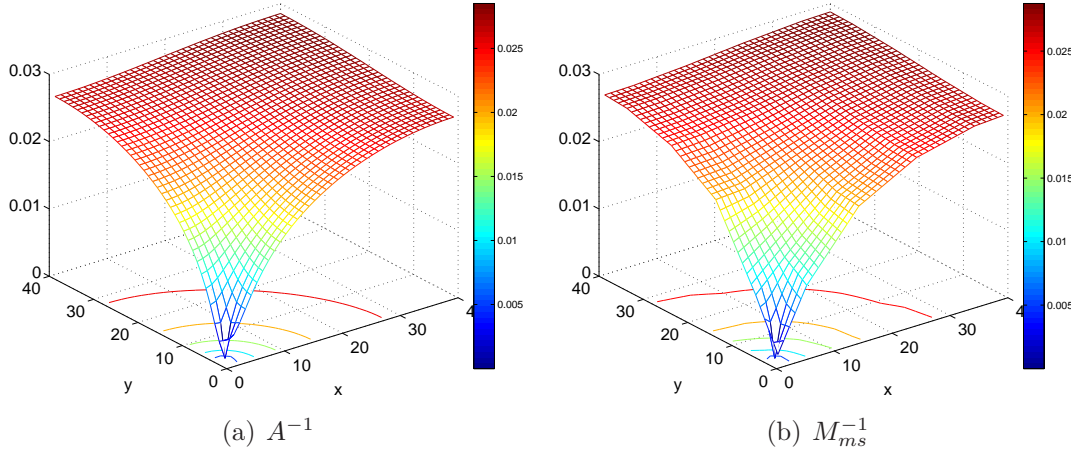


Figure 4.5: Eigenvectors of A^{-1} and M_{ms}^{-1} with the lowest frequency.

4.3.2 TAMS

The spectral analysis in the above subsection shows that AMS will not converge as a preconditioner for the Richardson iterative scheme. The crux of the problem is that AMS cannot resolve the high frequency errors in the fine-scale system. Therefore, we propose to combine the AMS operator with a local preconditioner that can resolve the high frequency errors. We refer to this approach as the two-stage algebraic multiscale solver (TAMS). The preconditioner of TAMS can be written as

$$M_{TAMS}^{-1} = M_{ms}^{-1} + M_{local}^{-1} - M_{local}^{-1} A M_{ms}^{-1}, \quad (4.17)$$

where M_{local} is the local preconditioner. Table (4.1) lists the algorithm that applies the TAMS in the Richardson iterative scheme.

As for the choice of the local preconditioner, block preconditioners are preferred because they are usually more computationally efficient and are well suited for parallel computation. Block ILU(0) (BILU) and the one-level additive Schwarz (AS) preconditioners are the two schemes considered here due to their locality, spectral properties, ease of implementation, and computational efficiency. Here, we consider

- 1: $\nu = 0$
- 2: initialize p^ν
- 3: construct the restriction operator \mathcal{R} from Eq. (2.28) or (2.32)
- 4: construct the prolongation operator \mathcal{P} from Eq. (4.9)
- 5: construct the AMS preconditioner from Eq. (4.2)
- 6: **while** ($\nu < \text{maximum iteration number} \ \&\& \text{not converged}$) **do**
- 7: update with AMS:

$$p^{\nu+1/2} = p^\nu + M_{ms}^{-1}(q - Ap^\nu)$$

- 8: update with local preconditioner:

$$p^{\nu+1} = p^{\nu+1/2} + M_{local}^{-1}(q - Ap^{\nu+1/2})$$

- 9: **end while**

Table 4.1: The TAMS algorithm for the Richardson iterative scheme.

only the BILU preconditioner. The comparison of BILU with AS is discussed in the next section.

We now take the same example as in the previous subsection. The second-stage preconditioner is BILU, which uses uniform 2×2 blocks. Fig. (4.6) shows the full spectra of the TAMS and BILU iteration matrices. All the eigenvalues of the TAMS iteration matrix are inside the unit circle, and the largest eigenvalue is significantly smaller than unity, which means the TAMS preconditioner will converge quickly when used in a Richardson iterative scheme. In contrast, the spectral radius of the BILU iteration matrix is very close to 1, which indicates that the BILU preconditioner converges, but at a much slower rate compared with the TAMS preconditioner. Recall AMS as the full preconditioner does not converge at all due to missing many high frequency errors components. Therefore, we expect that the two-stage preconditioning strategy will be superior to AMS and BILU if each is used exclusively.

Fig. (4.7) shows the histogram of the eigenvalues for TAMS and BILU iteration matrices. It is quite clear that the TAMS eigenvalues cluster around 0, which is an excellent property especially for Krylov subspace methods, as it is expected to

lead to faster convergence. On the other hand, the BILU spectra do not show such clustering behavior. More discussion on the clustering of eigenvalues and related deflation methods can be found in Cai et al. [1999] and references therein.

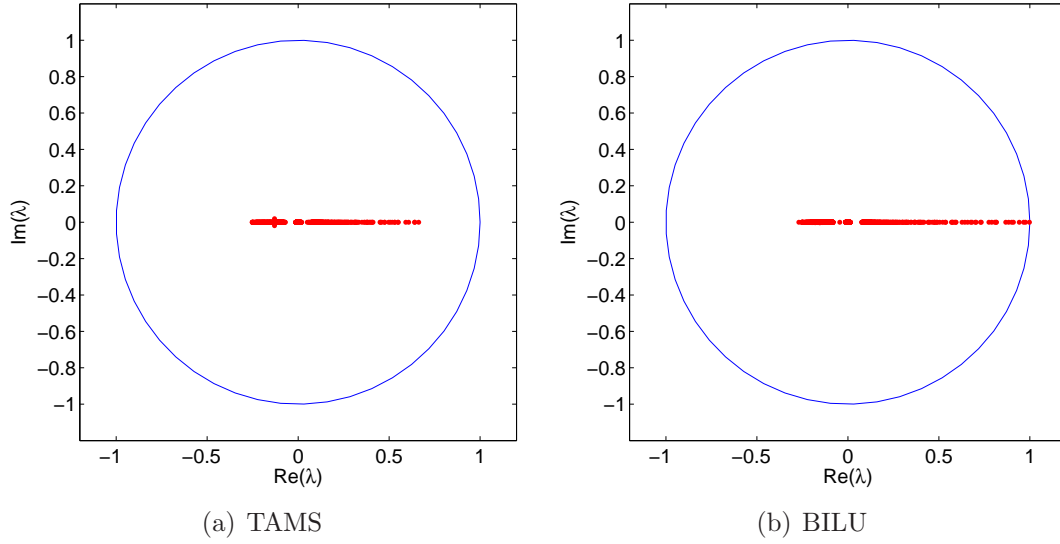


Figure 4.6: The full spectra of the iteration matrix(denoted by dots) for the isotropic homogeneous case.

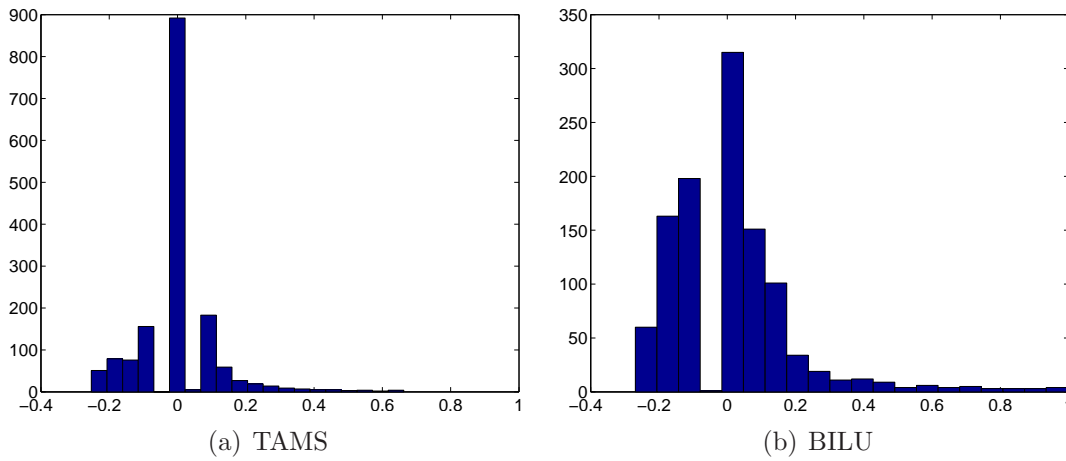


Figure 4.7: Histogram of the eigenvalues of the iteration matrix for the isotropic homogeneous case.

Fig. (4.8) shows the lowest and highest frequency eigenvectors of M_{TAMS}^{-1} . Comparison of Fig. (4.8) with the eigenvectors of the fine-scale matrix A^{-1} in Figs. (4.4) and (4.5) shows that TAMS represents both the lowest and highest frequencies very well. We also show the eigenvectors of the BILU local preconditioner (with a block size of 2×2) in Fig. (4.9), which indicates that the BILU preconditioner represents the high-frequency spectra very well and the low-frequency spectra quite poorly. The combination of AMS and BILU, i.e., the TAMS, yields a very good representation of the entire spectra of the target fine-scale matrix.

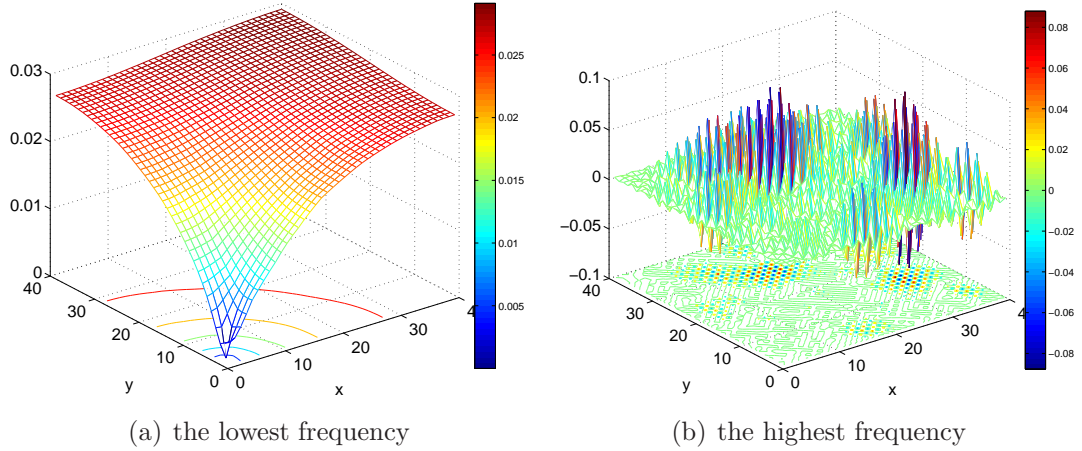


Figure 4.8: Eigenvectors of M_{TAMS}^{-1} with the highest and lowest frequencies

Figs. (4.10 – 4.11) show that when the size of the BILU blocks is increased (from 2×2 to 4×4), the spectral radius of the TAMS iteration matrix is reduced further and more eigenvalues are clustered around 0. However, the computational cost of BILU increases with the block size. More discussion on the overall computational efficiency can be found in the next section.

In realistic cases of subsurface flow, the permeability shows large heterogeneity and complex correlation structures, which is much more challenging than the simple example discussed so far. Therefore, we also show the spectra for a heterogeneous case, where the permeability field is the top layer of the SPE10 comparative case

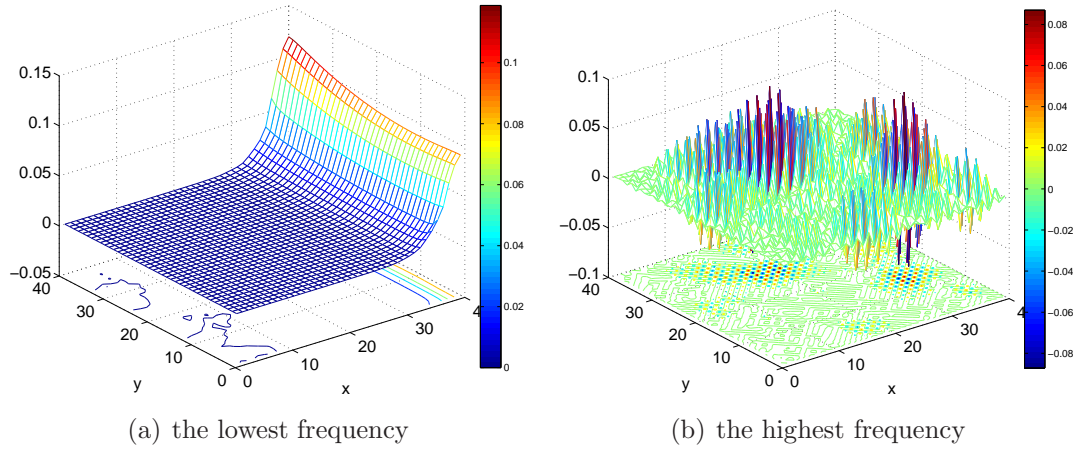


Figure 4.9: Eigenvectors of the local preconditioner M_{BILU}^{-1} with the highest and lowest frequencies

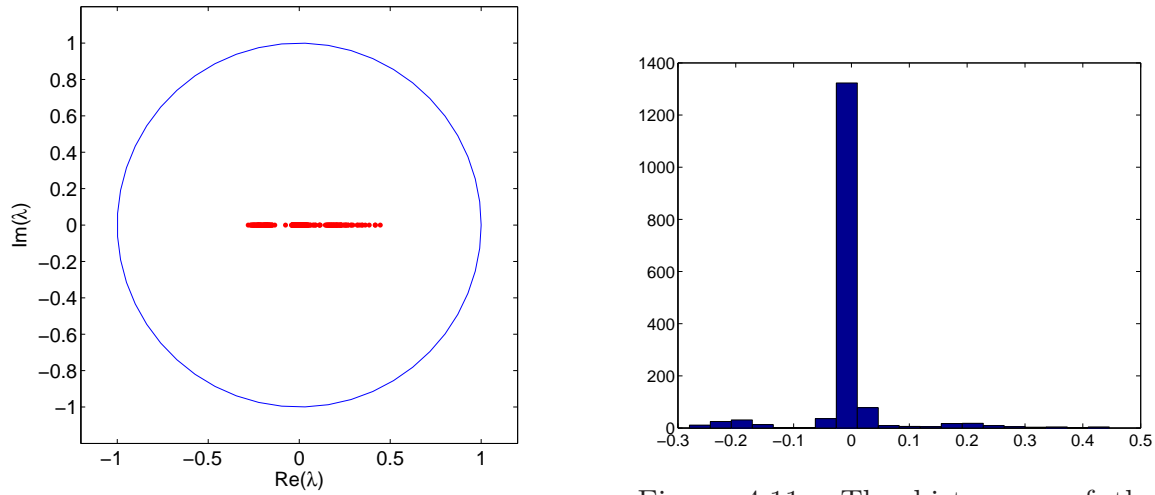


Figure 4.10: The full spectra of the iteration matrix(denoted by dots) for the isotropic homogeneous case: the block size of BILU is 4×4 .

Figure 4.11: The histogram of the spectra of the iteration matrix for the isotropic homogeneous case: the block size of BILU is 4×4 .

[Christie and Blunt, 2001] as shown in Fig. (4.12). The permeability varies by six orders of magnitude, and the variance of the natural logarithm of permeability is 5.5. The dimensions of the fine and coarse grids are 220×60 and 22×6 , respectively. No-flow boundary conditions are applied on all sides, and the pressure is fixed at fine cells $(1, 0)$ and $(80, 60)$ with values of 1 and 0, respectively. The BILU block size is chosen to be 4×4 . The spectra of the TAMS iteration matrix are shown in Fig. (4.13), which clearly indicates that the TAMS should converge rapidly for this highly heterogeneous case.

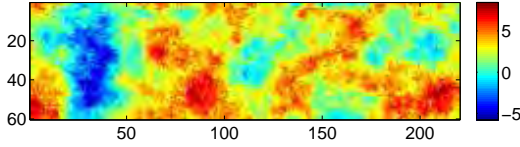


Figure 4.12: The natural logarithm of the top layer of the SPE 10 permeability.

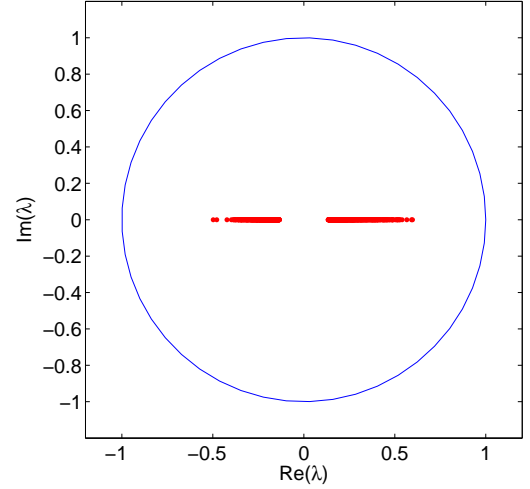


Figure 4.13: The spectra of the TAMS iteration matrix for the SPE 10 top layer permeability field.

We note that Hajibeygi et al. [2008] developed an iterative multiscale finite volume (i-MSFV) method, which was also shown to converge to the fine-scale solution. They constructed local correction functions on the dual coarse cells to improve the local errors on the dual grid. Their correction functions were updated in each iteration with global information. Line relaxation in each coordinate direction was employed as a smoother to provide the global information. The smoothing steps had to be applied several times for each iteration to ensure convergence, and the number of

smoothing steps was problem dependent. Their approach is not in an algebraic form and is quite difficult to use as a general linear preconditioner. The i-MSFV method employs additional global and local information from the smoother and the correction functions, respectively, to improve the convergence of the original multiscale finite-volume method. In contrast, the TAMS is purely algebraic and uses additional local information provided by a local preconditioner, e.g., BILU, only. Furthermore, the TAMS enjoys excellent convergence rates as shown in the next section.

4.3.3 Local Mass Conservation of TAMS

If the TAMS procedure in Table (4.1) stops when a target small convergence tolerance is achieved, we do not need to worry about mass conservation, since the fine-scale equations are satisfied with the desired accuracy everywhere. However, in many circumstances, we would like to maximize efficiency, but still maintain reasonable accuracy. In practice, one may choose a relatively large (loose) convergence tolerance and a small limit on the maximum number of iterations used to solve the system. Such a strategy involves significant risk if the computed numerical approximation does not guarantee local mass conservation. The violation of mass conservation often results in non-physical and unbounded saturation fields when solving the hyperbolic transport equations.

Recall that the prolongation operator defined by Eq. (4.9) is identical to that assembled from the basis functions solved from Eq. (2.23). If the finite-volume type restriction operator is used, the resulting multiscale solution is identical to the multiscale finite-volume method [Zhou and Tchelepi, 2008]. A nice property of the multiscale finite-volume method is that mass conservation is guaranteed on the coarse scale, which allows for the reconstruction of a locally conservative fine-scale velocity field as given by Eq. (2.48). Here we show that the TAMS guarantees local mass

conservation on the coarse scale if a single AMS step with the finite-volume type restriction operator is applied. Thus, one can also reconstruct the locally conservative fine-scale velocity from the TAMS pressure according to Eq. (2.48) (i.e., the same procedure as in the multiscale finite-volume method).

Lemma 3. *Local mass conservation is satisfied on the coarse grid if an AMS step with the finite-volume type restriction operator is applied after any iteration of the TAMS algorithm in Table (4.1).*

Proof. Denote the solution at iteration ν as p^ν , then the residual is $r = q - Ap^\nu$. Applying an AMS iteration to this residual vector, one obtains

$$\tilde{p} = p^\nu + \mathcal{P}(\mathcal{R}A\mathcal{P})^{-1}\mathcal{R}r. \quad (4.18)$$

Multiplication by $\mathcal{R}A$ on both sides of Eq. (4.18) yields

$$\mathcal{R}A\tilde{p} = \mathcal{R}Ap^\nu + (\mathcal{R}A\mathcal{P})(\mathcal{R}A\mathcal{P})^{-1}\mathcal{R}r = \mathcal{R}Ap^\nu + \mathcal{R}r = \mathcal{R}q, \quad (4.19)$$

which is equivalent to

$$\mathcal{R}(q - A\tilde{p}) = 0. \quad (4.20)$$

Note that \mathcal{R} is the finite-volume restriction operator defined in Eq. (2.28). Eq. (4.20) indicates that the coarse-grid finite-volume discretization equations are satisfied exactly everywhere in the coarse grid, i.e., mass conservation is guaranteed for each coarse cell. \square

As shown in the next section, using a Galerkin type restriction operator in TAMS is usually more robust and efficient as a general linear solver with tight convergence tolerance. However, the Galerkin type restriction operator does not ensure mass conservation. From **Lemma (3)**, we can apply an AMS step with the finite-volume

type restriction operator in the end, which fixes the conservation problem.

In summary, the TAMS offers three advantages as a preconditioner: 1) small spectral radius that ensures rapid convergence; 2) clustering of eigenvalues that allows for Krylov subspace methods to converge faster; 3) local mass conservation that permits relaxed convergence tolerances if desired.

4.4 Numerical Performance of TAMS

As discussed in the previous section, although TAMS converges for Richardson iteration, more sophisticated Krylov subspace methods can take advantage of the clustering of the eigenvalues of TAMS and obtain faster convergence. Here, we use GMRES [Saad, 1996] as the Krylov solver.

4.4.1 Convergence Study

For our convergence study, we take the same test case as in Hajibeygi et al. [2008]. A fine grid of 44×44 and a coarse grid of 4×4 are used, i.e., the coarsening ratio is 11×11 . The aspect ratio α is defined to be the ratio of the horizontal and vertical dimensions of the uniform fine grid, i.e.,

$$\alpha = \frac{\Delta x}{\Delta y}. \quad (4.21)$$

In terms of the anisotropy ratio of mobility, a case with isotropic permeability and aspect ratio α is identical to that with $\Delta x = \Delta y$ and $k_y = \alpha^2 k_x$.

Both homogeneous and heterogeneous permeability fields with different aspect ratios, α , are considered. In the homogeneous case, $k_x = k_y = 1$, and there is a source with $q = 1/(\Delta x \Delta y)$ and a sink with $q = -1/(\Delta x \Delta y)$ in fine cells (13, 13) and (32, 32), respectively. In the heterogeneous case, the permeability is shown in Fig. (4.14),

which is part of the top layer of the SPE 10 comparative case [Christie and Blunt, 2001]. The natural logarithm of the permeability has a variance of 6.66 and a mean of -0.29.

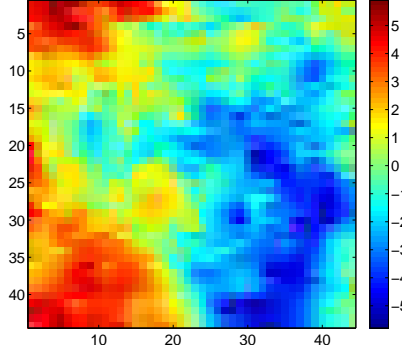


Figure 4.14: The natural logarithm of heterogeneous permeability for convergence study.

In the TAMS algorithm, the Galerkin type restriction operator is used for the AMS preconditioner, and BILU is chosen as the local preconditioner. The block size of BILU is fixed at 16 while two block shapes are used: one is a square block (i.e. 4×4) and the other is a line block (16×1). For comparison purposes, BILU as the sole preconditioner is also used. Both GMRES and Richardson solvers are considered. The error is measured by

$$\epsilon = \frac{\|p - p_f\|_\infty}{\|p_f\|_\infty}. \quad (4.22)$$

Fig. (4.15) shows the convergence histories for the test cases. BILU converges very slowly for the Richardson method, while TAMS improves the convergence rate dramatically. GMRES gives the convergence rate another boost as TAMS still converges significantly faster than BILU alone. TAMS with GMRES shows very good convergence rate for all the test cases. Compared with the convergence behaviors of the iterative multiscale finite-volume (i-MSFV) method [Hajibeygi et al., 2008], TAMS with GMRES takes several more iterations to reach the smallest error than

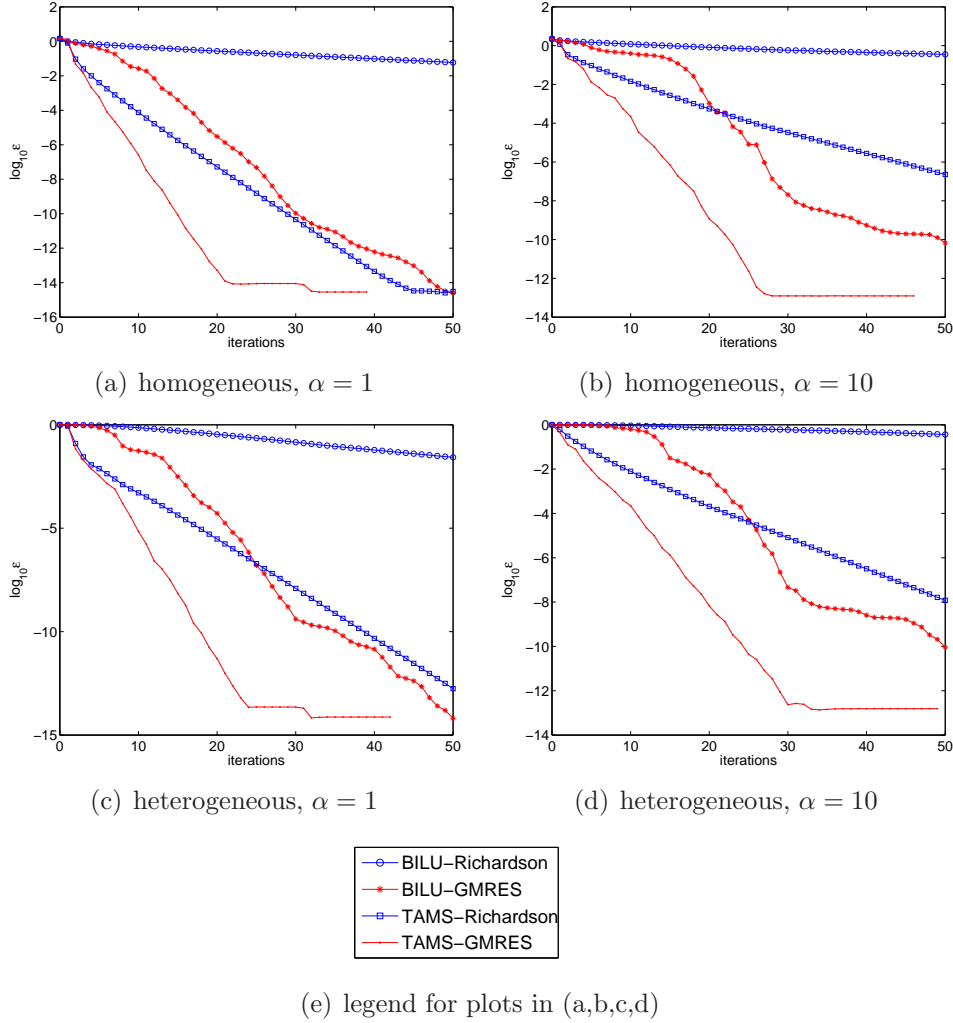


Figure 4.15: The convergence histories for homogeneous and heterogeneous cases with $\alpha = 1, 10$ (the legend of the plots shown in (e)).

the i-MSFV method with the most smoothing steps, while the former converges faster in the heterogeneous case especially for $\alpha = 10$. Actually, the performance of TAMS is largely insensitive to the heterogeneity, while it is slightly more sensitive to the aspect ratio. In contrast, the i-MSFV method is much more sensitive to the heterogeneity and aspect ratio.

4.4.2 Conservation Study

We have shown that application of a single AMS step with the finite-volume type restriction operator to the latest approximation of solution results guarantees mass conservation on the coarse scale. Then, a reconstruction procedure, Eq. (2.48), can be followed to obtain a locally conservative fine-scale velocity field. We now demonstrate this using a numerical example.

We consider a two-phase flow problem with the permeability from the SPE 10 bottom layer as shown in Fig. (2.23a). The main objective is to test the conservation of the method. Hence, we take linear relative permeability curves, i.e. $k_{rl} = S_l$, and a unit viscosity ratio, $\mu_1 = \mu_2$. No-flow boundary conditions are specified for all the boundaries of the domain. We introduce two wells in fine cells (6, 28) and (215, 28) and use the Peaceman model [Peaceman, 1977] to describe the well equation, i.e.,

$$q_{l,i}^w = WI\lambda_{l,i}(p_i - p_i^w). \quad (4.23)$$

Eq. (4.23) defines the flow rate of phase l flowing from a reservoir cell i into the well, where p_i is the pressure in cell i , p_i^w is the pressure of the well in that cell, and WI is referred as well index, which is given by

$$WI = \frac{2\pi kh}{\ln \frac{r_o}{r_w} + s}, \quad (4.24)$$

where h is the length of the well and s is the skin factor. Here we take $s = 0$. In this test case, we employ pressure control for the wells, i.e., the well pressure p^w is fixed in the two wells. We take $p_1^w = 5000$ psi for the well at (6, 28) and $p_2^w = 1000$ psi for the other well at (215, 28). A dimensionless time is employed, i.e.,

$$\tau = \frac{\phi L_x L_y \mu}{k(p_1^w - p_2^w)} \quad (4.25)$$

We choose the Galerkin type restriction operator and BILU as the local preconditioner for TAMS. The block size of BILU is 11×5 . After one TAMS iteration, the pressure error, ϵ , as computed from Eq. (4.22) is 3.04×10^{-2} . We compare the solutions of pressure for TAMS with the fine-scale reference, as well as AMS in Fig. (4.16). It is clear that the AMS shows large errors in the computed pressure field, while the TAMS yields a very accurate pressure solution in just one iteration. However, the fine-scale velocity field computed directly from the TAMS pressure does not ensure mass conservation. We define the mass conservation error in each fine cell Ω_i^f as

$$\epsilon_{con,i} = \frac{\| \oint_{\partial\Omega_i^f} \mathbf{u} \cdot \mathbf{n} d\Gamma + q \|}{q_{inj}}, \quad (4.26)$$

and the conservation error after one iteration of TAMS is shown in Fig. (4.17), where we plot the error in the range of $[0, 0.05]$. We note that the largest conservation error is 0.12. The pattern of conservation errors is nearly aligned with the dual grid, while it is also somewhat affected by the BILU preconditioner. The conservation errors will usually ruin the solution of the transport equation, i.e., resulting in unbounded saturations.

To ensure mass conservation after one iteration of TAMS, we apply an AMS step with the finite-volume type restriction operator, and then reconstruct a conservative fine-scale velocity from Eq. (2.48). The conservation error from this treatment is shown in Fig. (4.18), which is very small everywhere. In Fig. (4.19), we compare the saturation result computed using the reconstructed velocity with the fine-scale reference saturation and the saturation field computed after one iteration of TAMS without any reconstruction process. The saturation from the reconstructed velocity is close to the fine-scale reference, while the saturation directly from TAMS shows much larger errors. Actually, the saturation directly from TAMS is not bounded in $[0, 1]$, and Fig. (4.19c) is plotted in the range of $[0, 1]$ (i.e., out-of-bound values are

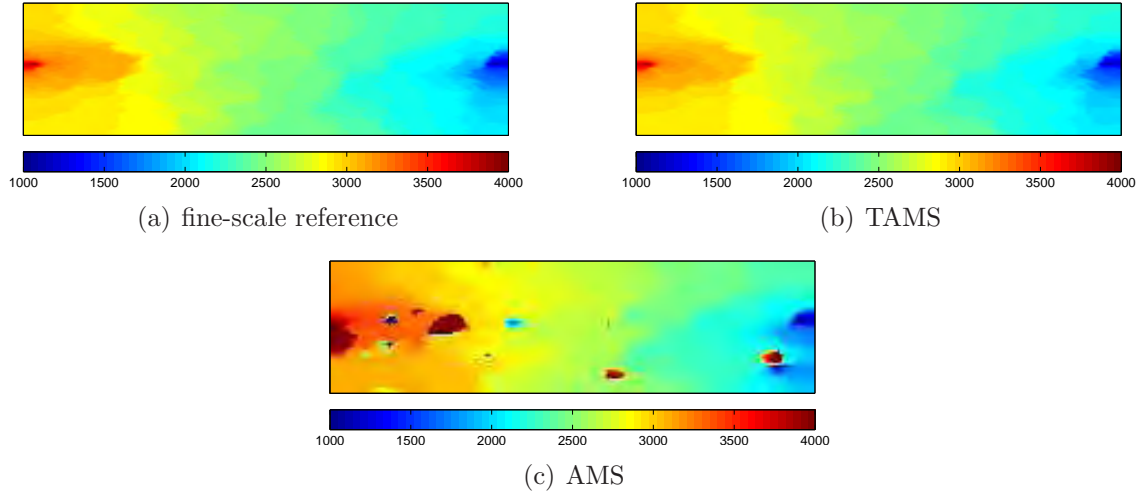


Figure 4.16: Pressure solutions of the fine-scale reference, the TAMS method (after one iteration) and the AMS in the case of conservation study

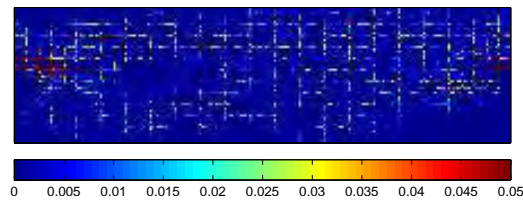


Figure 4.17: Conservation errors after one iteration of TAMS

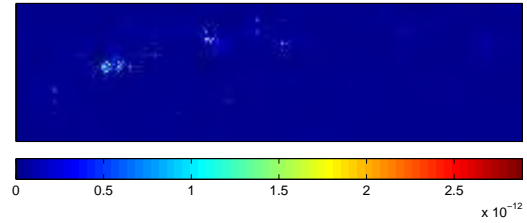


Figure 4.18: Conservation errors after one iteration of TAMS followed by applying one step of AMS with the finite-volume type restriction operator and a reconstruction process

truncated to the nearest bound). We note that the maximum value is 1.24×10^3 , which indicates the saturation solution suffers a lot from lack of mass conservation.

We measure the saturation error by the L-2 norm, i.e.,

$$e_s = \|S - S_{ref}\|_2. \quad (4.27)$$

Fig. (4.20) shows the saturation errors for different iteration steps, which are all followed by the reconstruction process. It is clear that the saturation error is quickly reduced with iterations.

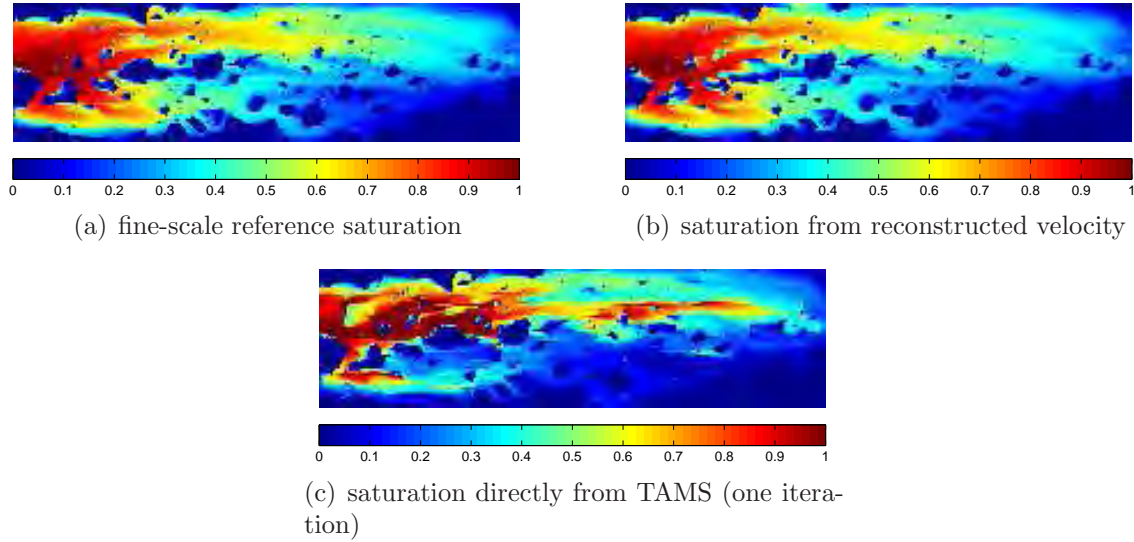


Figure 4.19: Fine-scale reference saturation and saturation computed from the reconstructed velocity or directly from TAMS

4.4.3 Efficiency Study

The TAMS is proposed to solve large-scale problems with complex permeability correlation structures and high spatial variability. Two large three-dimensional cases are considered here. The first one has a log-normally distributed permeability with

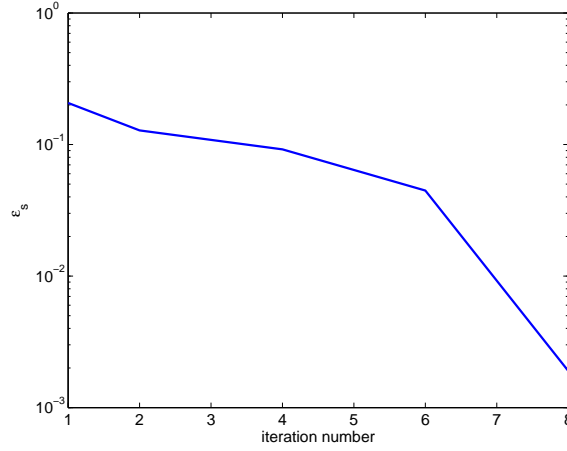


Figure 4.20: Saturation error versus the number of TAMS iterations

$128 \times 128 \times 64$ fine cells. The natural logarithmic permeability is generated by sequential Gaussian simulation [Deutsch and Journel, 1998] using a Gaussian distribution with a mean and variance of 4.0. The correlation lengths are one tenth of the physical dimensions. The permeability is shown in Fig. (4.21), where the permeability values vary by five orders of magnitudes. The second example is the 10th SPE comparative solution model [Christie and Blunt, 2001], which is known for its highly detailed complex geological description. The full permeability field is shown in Fig. (4.22). It contains $220 \times 60 \times 85$ fine cells (1.1 million). The top 35 layers are for the Tarbert formation and represent a prograding near-shore environment, while the bottom 50 layers are fluvial and contain lots of channel structures [Christie and Blunt, 2001].

In both cases, Dirichlet boundary conditions are applied on the left and right faces with dimensionless pressures of 1 and 0, respectively; no-flow boundary conditions are specified for all the other boundaries. Both isotropic and anisotropic permeability fields are studied for each case. In the isotropic problem, $\Delta x = \Delta y = \Delta z$ and $k_x = k_y = k_z$. In the anisotropic one, $\Delta x = \Delta y = \Delta z$ and $k_y = 1000k_x, k_z = 10k_x$. In the two cases, k_x is given by the permeability shown in Figs. (4.21) and (4.22), respectively.

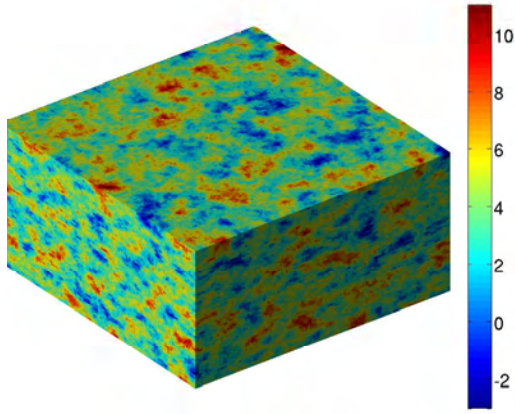


Figure 4.21: The natural logarithm of the log-normal distributed permeability field.

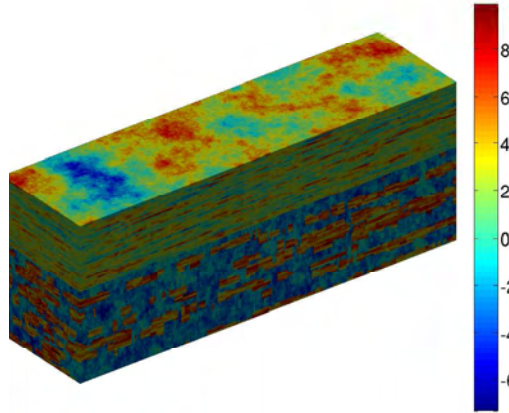


Figure 4.22: The logarithm of the SPE 10 permeability field.

The coarse grids are fixed at $16 \times 16 \times 8$ for the log-normal case (coarsening ratio $8 \times 8 \times 8$) and $22 \times 6 \times 17$ for the SPE 10 case (coarsening ratio $10 \times 10 \times 5$). Solutions given by TAMS are shown in Figs. (4.23) and (4.24) for the two cases, respectively. GMRES is used and the stopping criterion is a relative residual L-2 norm of 10^{-5} , i.e., $\|r_k\|_2 / \|r_0\|_2 \leq 10^{-5}$.

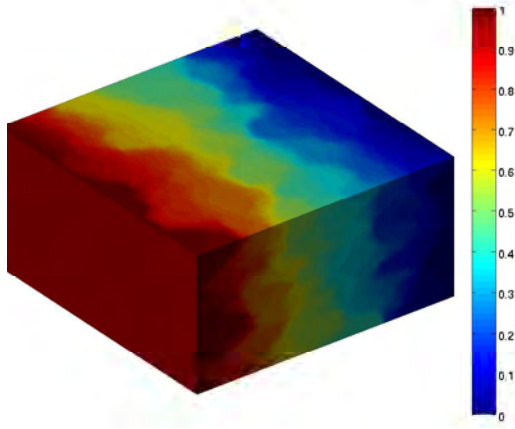


Figure 4.23: Solution of the log-normal case.

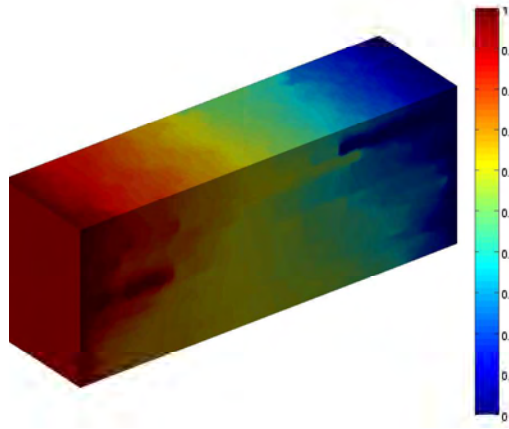


Figure 4.24: Solution of the SPE 10 case.

Our objective here is to investigate the efficiency of TAMS and evaluate various

options of the TAMS algorithm. As discussed earlier, in TAMS one can choose Galerkin or FVM type restriction operators. There are also numerous options for the local preconditioner. Here, we limit the study to BILU and Additive Schwarz (AS). There are also several choices for the parameters of the two preconditioners, for example, the dimension of the blocks of BILU, and the size of the AS blocks and amount of overlap. Two different dimensions are considered for the BILU blocks: $2 \times 2 \times 4$ and $4 \times 4 \times 4$ in the log-normal case, and $2 \times 2 \times 5$ and $4 \times 4 \times 5$ in the SPE 10 case. For AS, we choose the blocks to be the same as the primal coarse cells and overlapping sizes of 0 and 1 in each dimension are considered. Table (4.2) lists the options and parameters used here.

restriction operator of AMS	FVM or Galerkin
local preconditioner	BILU or ASM
Dimension of BILU blocks	$2 \times 2 \times 4(16)$ or $4 \times 4 \times 4(64)$ for log-normal $2 \times 2 \times 5(20)$ or $4 \times 4 \times 5(80)$ for SPE 10
Overlapping of AS blocks	0 or 1

Table 4.2: Various options and parameters for TAMS

Table (4.3) shows the GMRES iteration numbers and the solver CPU time for the two cases. The code is written in C++ and built around the PETSC [Balay et al., 2008] linear libraries. We have not done any performance tuning yet. It is quite clear from Table (4.3) that the Galerkin restriction operator is superior to the finite-volume type restriction operator. The results in the table also show that BILU is more efficient than AS. The combination of the Galerkin restriction operator and BILU yields the most efficient and robust results in all the test cases. As for BILU, larger block sizes improve the convergence rate, but each BILU iteration becomes more expensive. An optimal size would depend on the overall problem size and the specific computer used. Generally, a block size of around 16 is recommended. For AS, the overlapping of local blocks increases the convergence rate mildly, while the

CPU cost gets much more expensive. Thus overlapping AS is not recommended as the local preconditioner.

			log-normal				SPE 10			
			Isotropic		Anisotropic		Isotropic		Anisotropic	
			its.	cpu	its.	cpu	its.	cpu	its.	cpu
Galerkin	BILU	16; 20	13	8.1	30	19.2	22	14.5	43	26.5
		64; 80	11	8.4	28	22.1	16	14.8	37	29.1
	AS	0	20	16.2	86	48.5	34	27.5	> 100	-
		1	19	26.2	84	76.2	28	36.7	> 100	-
FVM	BILU	16; 20	14	8.1	30	21.0	> 100	-	> 100	-
		64; 80	11	8.3	32	23.9	> 100	-	> 100	-
	AS	0	21	15.8	> 100	-	> 100	-	> 100	-
		1	19	25.9	> 100	-	> 100	-	> 100	-

Table 4.3: GMRES iterations and solver CPU time (seconds) of TAMS with different options and parameters for the two three-dimensional cases.

With optimum options in the TAMS algorithm, i.e., Galerkin type restriction operator and BILU, the iteration numbers in the anisotropic cases increase very slightly compared with the corresponding isotropic cases. Recall that the anisotropy in the mobility is as high as 1000 in the $x - y$ plane and 100 in the $y - z$ plane. These results demonstrate that TAMS is a very powerful preconditioner even for highly anisotropic problems.

Notice that TAMS with the finite-volume type restriction operator fails to converge within 100 iterations in the SPE10 case. As we have discussed, the performance of the multiscale finite-volume method deteriorates for the channelized permeability field, in which the coarse-scale operator of MsFVM may lose its monotonicity. The Galerkin type of restriction operator, which resembles the multiscale finite element method [Hou and Wu, 1997], is more robust and efficient for permeability fields with channel-like structures.

In Table (4.4), we show a comparison of TAMS with what is considered as the

state-of-the-art preconditioner for linear elliptic systems, namely, algebraic multigrid (AMG) [Stüben, 2000]. The AMS construction time refers to the time spent on the construction of the multiscale restriction and prolongation operators and the global coarse system. The BILU construction time denotes the CPU time spent on LU factorization of the local blocks. The total time for TAMS is the sum of the solver time, the AMS construction time, and the BILU construction time. The time spent on initialization of the wirebasket system and the blocked system for BILU is not included. Table (4.4) shows that TAMS is more efficient than AMG in most test cases with an exception of the anisotropic log-normal permeability case. Moreover, the local LU factorization of BILU and construction of the prolongation operator (the most expensive part of AMS) are perfectly parallelizable. Therefore, TAMS is expected to be very efficient for large-scale massively parallel computation.

It is also worth noting that the TAMS is expected to be more efficient for time dependent multiphase problems with coupled flow and transport. Adaptive computation can be introduced to further improve the efficiency. For example, in the construction of the prolongation operator, only local regions that experience large mobility changes need to be recomputed. Furthermore, since the TAMS has the capability to ensure local mass conservation, a relatively large (loose) convergence tolerance for the pressure solution can be taken, while still maintaining good accuracy when solving the transport equations.

		log-normal		SPE 10	
		Isotropic	Anisotropic	Isotropic	Anisotropic
AMG	solver time	43.6	17.0	46.4	56.1
TAMS	AMS construction time	9.3	9.8	9.1	9.0
	BILU construction time	2.6	2.6	3.2	3.3
	solver CPU time	8.1	19.2	14.5	26.5
	total time	20.0	31.6	26.8	38.8

Table 4.4: Comparison of CPU time for TAMS and AMG in the efficiency test cases.

4.4.4 Scalability Analysis

Scalability is an important measure of the performance of an algorithm for large-scale problems. Scalability depends strongly on two issues: (1) how the iterations and computational effort depend on the problem size and (2) for the same problem, how the performance depends on the coarsening ratio.

In the first example set, the coarsest grid is $32 \times 32 \times 32$ and the logarithm permeability is generated by sequential Gaussian simulation [Deutsch and Journel, 1998] from a Gaussian distribution that has a mean and variance of 4. Then piecewise constant refinement by a factor of two is used in each direction. In total, three grids are generated with a dimension of $32 \times 32 \times 32$, $64 \times 64 \times 64$ and $128 \times 128 \times 128$, respectively. The permeability fields are shown in Fig. (4.25). Dirichlet boundary conditions are applied on the left and right faces with dimensionless pressures of 1 and 0, respectively; no-flow boundary conditions are specified for all the other boundaries. We fix the coarsening ratio to be $8 \times 8 \times 8$ for the three grids. The GMRES iteration numbers and CPU time are shown in Table (4.5). The Galerkin restriction operator and BILU with a block size $4 \times 4 \times 4$ are used for TAMS. Table (4.5) indicates that the convergence rate is largely insensitive to problem size. Actually in this case, the convergence rate is slightly better for larger problems. Fig. (4.26) shows the increase of CPU time with problem size, where the CPU time and problem sizes are all normalized by the values of the coarsest grid (i.e., the value (the CPU time or problem size) of a specific grid divided by the corresponding value of the $32 \times 32 \times 32$ grid). The CPU time increases linearly with problem size. All the results are quite close to the theoretical linear reference line that has a unit slope. The slope for the solver time is even smaller than 1. This result shows that TAMS is perfectly scalable with problem size for this case.

In the second test case, we consider the problem with $128 \times 128 \times 128$ fine cells, and we study the behavior for three coarsening ratios: $4 \times 4 \times 4$, $8 \times 8 \times 8$ and $16 \times 16 \times 16$.

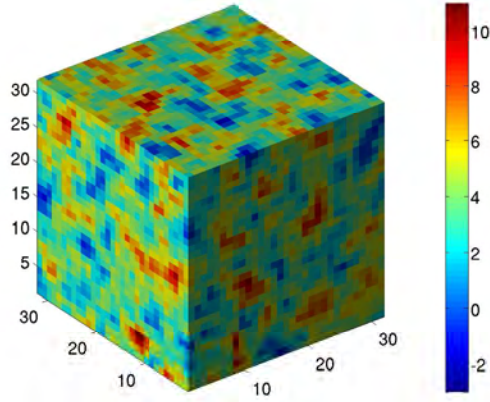


Figure 4.25: The natural logarithm of heterogeneous permeability for scalability study.

problem size	$32 \times 32 \times 32$	$64 \times 64 \times 64$	$128 \times 128 \times 128$
GMRES iterations	12	10	8
solver time	0.43	3.03	24.5
AMS construction time	0.14	1.24	11.27
BILU construction time	0.30	2.66	21.62

Table 4.5: Iteration numbers and CPU time for different sizes of problems

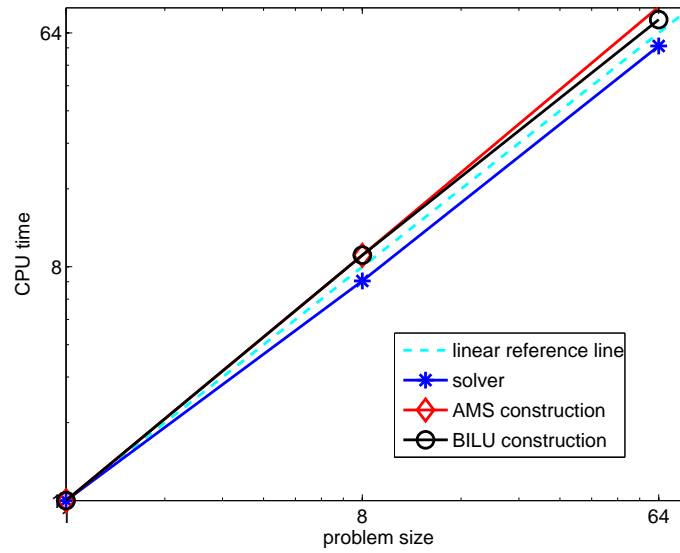


Figure 4.26: The increase of CPU time with problem sizes. The CPU time and problems size are normalized by those of the $32 \times 32 \times 32$ problem

The GMRES iteration numbers and CPU time are shown in Table (4.6). It is not surprising that increasing the coarsening ratio (i.e., smaller coarse grid) reduces the convergence rate. As we have discussed in Section 2.8.1), with larger coarsening ratios, the reduced boundary conditions on the dual grid have a larger domain of influence, which deteriorates the accuracy of the multiscale solution. Moreover, each dual block becomes larger, and the construction of AMS is thus more expensive. On the other hand, we do not want to use coarsening ratios that are too small as the global coarse system becomes larger and each iteration becomes more expensive. An optimal choice for the coarsening ratio is problem dependent, and at this stage, trial and error is recommended for practical applications. From our numerical experience, as with the coarsening ratio in OBMM (see the discussion in Section 2.8.1), it is usually a very good starting point to choose the coarsening ratio in each coordinate direction to be approximately the square root of the fine-grid dimension in that direction.

coarsening ratio	$4 \times 4 \times 4$	$8 \times 8 \times 8$	$16 \times 16 \times 16$
GMRES iterations	6	8	16
solver time	26.9	24.5	44.4
AMS construction time	8.5	11.3	34
BILU construction time	21.5	21.6	21.5

Table 4.6: Iteration numbers and CPU time for different coarsening ratios.

4.5 Conclusions

An efficient two-stage algebraic multiscale solver (TAMS) was proposed. The TAMS consists of two stages, one global and one local. In the global stage, a multiscale solution is obtained purely algebraically from the fine-scale matrix. An algebraic prolongation operator is obtained from the wirebasket ordered reduced system of the fine-scale system. Two restriction operators are defined: one is based on the finite-volume discretization and the other is based on the Galerkin scheme. In the second

stage, a local solution is constructed from a simple block preconditioner, such as Block ILU(0) (BILU), or an Additive Schwarz (AS) method.

It is demonstrated by spectral analysis that the TAMS approximates the full spectra of the original matrix very well, and that convergence to the fine-scale solution is guaranteed. Moreover, the spectra of TAMS tend to cluster, and this leads to more rapid convergence by Kryolov subspace methods, such as GMRES. The TAMS method can also preserve the favorable property of local mass conservation of the multiscale finite-volume method. This is achieved by applying a multiscale solution step with the finite-volume restriction operator to the latest approximate solution.

A convergence study that uses a test case similar to that in the i-MSFV paper of Hajibeygi et al. [2008] was investigated. The results indicate that TAMS is less sensitive to heterogeneity and anisotropy than the i-MSFV method. Moreover, i-MSFV requires several smoothing steps and needs to construct the correction functions for every dual coarse block in each iteration. In contrast, no correction function computation or global smoothing step is needed in the TAMS. As a result, we expect the TAMS to be more efficient and robust compared with the i-MSFV method.

Challenging large-scale problems with complex heterogeneous structures and high anisotropy ratios were presented for TAMS. The Galerkin type restriction operator and the BILU local preconditioner with a reasonable block size are the most robust and efficient choice for TAMS across a wide range of problems.

The performance of TAMS is comparable to the state-of-the-art algebraic multi-grid (AMG) preconditioner. The TAMS is easy to parallelize both in the construction of the multiscale operators and the factorization of the BILU blocks. Moreover, the CPU time of TAMS is almost linear with problem size, which is very important for large-scale problems. TAMS is expected to be especially efficient for time dependent problems with coupled multiphase flow and transport. This is due to adaptive computation of the prolongation operator and relaxed convergence tolerance for pressure,

since local conservation can always be achieved.

Chapter 5

Conclusions and Future Work

5.1 Summary and Conclusions

We have developed an algebraic multiscale framework. Within this framework, an operator-based multiscale method (OBMM) was proposed to solve general multiphase flow problems. The key ingredients of the method are two algebraic multiscale operators, prolongation and restriction, with which the multiscale solution can be constructed algebraically. We focused on the application of OBMM to flow problems. The prolongation operator for pressure is assembled from the pressure (dual) basis functions. The restriction operator depends on the chosen discretization scheme for the coarse-scale equations. We have shown the restriction operators based on finite volume and Galerkin finite-element methods.

We demonstrated that it is straightforward to extend OBMM to general flow problems that involve more physical mechanisms, such as compressibility, gravity and capillary pressure. OBMM was shown to be quite effective in dealing with challenging multiphase depletion problems, in which the compressibility effects associated with a highly mobile gas phase dominate both the pressure and saturation fields. OBMM was also used to solve gravity segregation problems. For homogeneous domains, the

OBMM are exact, and in heterogeneous multi-dimensional problems, the OBMM results are quite accurate.

Analysis of the computational complexity revealed that OBMM is much more efficient (at least an order-of-magnitude) than standard fine-scale methods. The efficiency of OBMM is largely due to the fact that no part of the algorithm operates on the global fine-scale problem directly. Instead, local basis functions are used to assemble a global coarse-scale system. Construction and solution of a global coarse-scale system of equations take a relatively small computational effort. Moreover, the ability to update the basis functions adaptively, when and where needed, enhances the overall efficiency of OBMM.

The efficiency of OBMM can be further improved by choosing an appropriate coarsening ratio. We studied the effect of the coarsening ratio on the performance of OBMM, and we derived a formula for the optimal coarsening ratio, based on reasonable assumptions regarding the computational complexity for solving a linear system. With the increase of coarsening ratio, the multiscale solution errors increase because the size of the global coarse-grid system gets smaller and the region affected by the reduced boundary condition gets larger. Numerical examples show that the error growth with coarsening ratio is quite mild and that accuracy is still maintained even for coarsening ratios that are quite large. The effect of adaptive thresholds for updating the basis and correction functions was also studied. The result indicates that for practical multiphase problems of coupled flow and transport (i.e., slightly compressible, viscous dominated displacements), the accuracy of the multiscale solutions is weakly dependent on the adaptivity thresholds, while the overall efficiency is much more sensitive to the adaptivity thresholds.

In the original multiscale finite-volume method, multiscale computations produce a conservative fine-scale total-velocity field, which is used to solve the transport problems (saturation equations) on the fine grid. We developed an adaptive multiscale

formulation for the saturation equations, which employs three adaptive prolongation operators to solve for the saturation field by multiscale computations.

At a given time, different saturation prolongation operators are used based on the region a (primal) coarse block belongs to. Specifically, for the time interval of interest, the physical domain is divided into three distinct regions: (1) Region 1, where the injection fluid has not yet invaded the cell, (2) Region 2, where an injection front encroached and the saturation of the injection fluid increases rapidly, and (3) Region 3, where the saturation changes slowly after the sharp front has moved through. Simple threshold criteria were proposed to identify the transitions between the various regions. In Region 1, the transport computations can be completely skipped; whereas in Regions 2, the FVFS (full velocity-full saturation) operator is used, which reconstructs a conservative fine-scale velocity and solves for the fine-scale saturation. Finally for Region 3, we developed two efficient approximate prolongation operators: the AVFS (approximate velocity-full saturation) operator that approximates the fine-scale velocity and then solves for the fine-scale saturation, and the AS (approximate saturation) operator, which directly approximates the fine-scale saturation from the coarse-scale saturation. We devised a criterion for choosing between the AVFS and AV operators in Region 3.

The adaptive multiscale method for flow and transport was tested using a series of models with different permeabilities (homogeneous and heterogeneous) and boundary conditions (no-flow and Dirichlet). Challenging cases with additional physical mechanisms, such as compressibility and gravity, and changing well locations were also investigated using the multiscale formulation. It was demonstrated that the results obtained with adaptive multiscale computations of flow and transport are in excellent agreement with the reference fine-scale solutions for this wide range of problems.

Computational complexity analysis reveals that the adaptive multiscale formulation of transport is significantly more efficient than the original multiscale finite-volume method that entails full construction of both velocity and saturation fields on the fine scale. The computational time for large three-dimensional problems show clearly that the multiscale formulation of coupled flow and transport is much more efficient than the original multiscale finite-volume method, which is already significantly more efficient than fine-scale methods.

The efficiency of multiscale modeling of transport is strongly related to the adaptivity thresholds. The choice of these thresholds is problem dependent. For common flow and transport problems in reservoir simulation practice (i.e., slightly compressible, viscous dominated displacements), the accuracy of multiscale modeling is weakly dependent on the thresholds. We suggested threshold values for various transport problems.

An efficient two-stage algebraic multiscale solver (TAMS) was proposed to overcome the limitations of the multiscale finite-volume method for channelized permeability fields and highly anisotropic problems. The TAMS is purely algebraic and only needs the fine-scale coefficient matrix and the wirebasket ordering information of the multiscale grid. Thus, the TAMS can be applied as a preconditioner for solving the large-scale linear systems associated with the pressure field.

The TAMS consists of two stages, one global and one local. In the global stage, a multiscale solution is obtained purely algebraically from the fine-scale matrix. The prolongation operator is obtained algebraically using the wirebasket ordered reduced system of the original fine-scale coefficient matrix. Two restriction operators are defined: one is based on the finite-volume discretization and the other is based on the Galerkin scheme. In the second stage, a local solution is constructed from a simple block preconditioner, such as Block ILU(0) (BILU), or an Additive Schwarz (AS) method.

It is demonstrated by spectral analysis that the TAMS approximates the full spectra of the original matrix very well, and that convergence to the fine-scale solution is guaranteed. Moreover, the spectra of TAMS tend to cluster, and this leads to more rapid convergence by Kryolov subspace methods, such as GMRES. The TAMS can also preserve the favorable property of local mass conservation of the multiscale finite-volume method. This is achieved by applying a multiscale solution step with the finite-volume restriction operator to the latest approximate solution.

Challenging large-scale problems with complex heterogeneous structures and high anisotropy ratios were presented for TAMS. The Galerkin type restriction operator and the BILU local preconditioner with a reasonable block size are the most robust and efficient choice for TAMS across a wide range of problems.

The performance of TAMS is comparable to the state-of-the-art algebraic multigrid (AMG) preconditioner. The TAMS is easy to parallelize both in the construction of the multiscale operators and the factorization of the BILU blocks. Moreover, the CPU time of TAMS is almost linear with problem size, which is very important for large-scale problems. TAMS is expected to be especially efficient for time dependent problems with coupled multiphase flow and transport. This is due to adaptive computation of the prolongation operator and relaxed convergence tolerance for pressure, since local conservation can always be achieved.

In summary, the algebraic multiscale framework developed in this dissertation allows for efficient and accurate multiscale computation of both flow and transport problems. The algebraic multiscale framework has been used to construct a powerful two-stage linear preconditioner that ensures convergence and local mass conservation.

5.2 Recommendations for Future Work

We developed an algebraic multiscale framework for general multiphase problems of coupled flow and transport arising from reservoir simulation practice. The framework can be extended further in the following directions.

- Capillary pressure can be naturally incorporated into the OBMM framework. However, at an even smaller scale (for example, the pore scale), capillary forces are dominant and capillary pressure is a function of both saturation and rock type. It is much more challenging to perform multiscale computation on this scale. We may need to consider more scales (rather than two scales as in the current framework) for multiscale computations.
- Well models with multiple completions should be considered in OBMM. Existing approaches employ well basis functions for multiscale modeling of wells, which can be readily incorporated into OBMM. Another possible approach is to take into account well effects using local preconditioners as in the TAMS.
- We have compared the efficiency of OBMM with the fine-scale method based on computational complexity analysis. We also need to design efficient data structures to implement the OBMM such that the efficiency can be demonstrated for large-scale problems.
- Existing multiscale methods are all based on the sequential formulation of flow and transport. In practice, the fully implicit formulation is widely used for the coupled systems associated with general-purpose reservoir simulation. The development of multiscale formulations for fully implicit systems will further broaden the use of multiscale methods.
- We have shown problems where the dominant mechanism is compressibility, viscous force or gravity. It is also quite interesting to investigate problems

where the dominant mechanisms vary strongly in time and space and further test the robustness of the proposed multiscale method.

The TAMS developed here focused on the flow equations with simplified physics, which is a necessary first step. More work is needed to combine the general multiscale flow and transport modeling with TAMS, which may serve as the cornerstone for building next generation reservoir simulators. The following topics are specifically recommended.

- Apply the ideas of TAMS to the transport problems, i.e., combining the multiscale formulation of transport with some local preconditioners to achieve convergence of the saturation field. Thus, a two-stage preconditioner for transport problems can be constructed.
- Adaptive computation in the TAMS should be studied to achieve high efficiency, not only in the adaptive construction of the prolongation operators but also in the updating with the local preconditioner. For example, only blocks with large errors need to be updated during the BILU iteration. For coupled flow and transport problems, we can adaptively apply the TAMS algorithm for the pressure computations. In regions critical to the transport computation, a tight convergence tolerance for TAMS can be used to obtain an accurate fine-scale velocity, while in other regions, the tolerance can be relaxed. The overall efficiency in solving the coupled system would be greatly improved.
- TAMS is very suitable for parallel computation, as the construction of prolongation operator and LU factorization of BILU blocks are naturally parallel. An efficient parallel implementation of TAMS on GPU and multi-core hybrid architectures will be valuable.

Bibliography

- J. E. Aarnes. On the use of a mixed multiscale finite element method for greater flexibility and increased speed or improved accuracy in reservoir simulation. *Multiscale Modeling and Simulation*, 2(3):421–439, 2004.
- J. E. Aarnes and Y. Efendiev. An adaptive multiscale method for simulation of fluid flow in heterogeneous media. *Multiscale Modeling and Simulation*, 5(3):918–939, 2006.
- J. E. Aarnes and T. Y. Hou. Multiscale domain decomposition methods for elliptic problems with high aspect ratios. *Acta Mathematicae Applicatae Sinica*, 18(1):63–76, 2002.
- J. E. Aarnes, S. Krogstad, and K.-A. Lie. A hierarchical multiscale method for two-phase flow based upon mixed finite elements and nonuniform coarse grids. *Multiscale Modeling and Simulation*, 5(2):337–363, 2006.
- J. E. Aarnes, S. Krogstad, and K.-A. Lie. Multiscale mixed/mimetic methods on corner-point grids. *Computational Geosciences*, 12(3):297–315, 2008.
- I. Aavatsmark. An introduction to multipoint flux approximations for quadrilateral grids. *Computational Geosciences*, 6:405–432, 2002.

- T. Arbogast. Implementation of a locally conservative numerical subgrid upscaling scheme for two-phase Darcy flow. *Computational Geosciences*, 6:453–481, 2002.
- T. Arbogast and K. J. Boyd. Subgrid upscaling and mixed multiscale finite elements. *SIAM Journal of Numerical Analysis*, 44:1150–1171, 2006.
- T. Arbogast and S. L. Bryant. A two-scale numerical subgrid technique for waterflood simulations. *SPE Journal*, 7:446–457, 2002.
- P. Audigane and M. J. Blunt. Dual mesh method for upscaling in waterflood simulation. *Transport in Porous Media*, 55:71–89, 2004.
- K. Aziz and A. Settari. *Petroleum Reservoir Simulation*. Elsevier Applied Scientific Publisher, 1979.
- S. Bachu and D. Cuthiell. New pseudo functions to control numerical dispersion. *Water Resources Research*, 26:863–874, 1990.
- S. Balay, K. Buschelman, V. Eijkhout, W. D. Gropp, D. Kaushik, M. G. Knepley, L. C. McInnes, B. F. Smith, and H. Zhang. PETSc users manual. Technical Report ANL-95/11 - Revision 3.0.0, Argonne National Laboratory, 2008.
- J. W. Barker and P. Dupouy. An analysis of dynamic pseudo-relative permeability methods for oil-water flows. *Petroleum Geoscience*, 5:385–394, 1999.
- J. W. Barker and S. Thibeaudeau. A critical review of the use of pseudo-relative permeabilities for upscaling. *SPE Reservoir Engineering*, 12:138–143, 1997.
- F. Brezzi, J. Douglas, and L. D. Marini. Two families of mixed elements for second order elliptic problems. *Numerische Mathematik*, 47:217–235, 1985.
- W. L. Briggs, V. E. Henson, and S. F. McCormick. *A Multigrid Tutorial*. SIAM, second edition edition, 2000.

- J. Caers. *Petroleum Geostatistics*. Society of Petroleum Engineers, 2005.
- X. Cai, B. F. Nielsen, and A. Tveito. An analysis of a preconditioner for the discretized pressure equation arising in reservoir simulation. *International Journal of Numerical Analysis*, 19:291–316, 1999.
- X. C. Cai, W. D. Gropp, and D. E. Keyes. A comparison of some domain decomposition algorithms for nonsymmetric elliptic problems. In *Fifth International Symposium on Domain Decomposition Methods for Partial Differential Equations*, pages 224–235, 1992.
- R. Car and M. Parrinello. Unified approach for molecular dynamics and density-functional theory. *Physical Review Letters*, 55:2471–2474, 1985.
- Y. Chen. *Upscaling and subgrid modeling of flow and transport in heterogeneous reservoirs*. PhD thesis, Stanford University, Stanford, CA, 2005.
- Y. Chen and L. J. Durlofsky. Adaptive local-global upscaling for general flow scenarios in heterogeneous formations. *Transport in Porous Media*, 62:157–185, 2006.
- Y. Chen, L. J. Durlofsky, M. Gerritsen, and X. H. Wen. A coupled local-global upscaling approach for simulating flow in highly heterogeneous formations. *Advances in Water Resources*, 26:1041–1060, 2003.
- Z. Chen and T. Hou. A mixed finite element method for elliptic problems with rapidly oscillating coefficients. *Mathematical Computation*, 72:541–576, 2003.
- M. A. Christie. Flow in porous media – scale up of multiphase flow. *Colloid & Interface Science*, 6:236–241, 2001.
- M. A. Christie and M. J. Blunt. Tenth SPE comparative solution project: A comparison of upscaling techniques. *SPE Reservoir Evaluation & Engineering*, 4:308–317, 2001.

- M. A. Christie, T. C. Wallstrom, L. J. Durlofsky, D. H. Sharp, and Q. Zou. Effective medium boundary conditions in upscaling. In *the 7th European Conference on the Mathematics of Oil Recovery*, Baveno, Italy, 2000.
- G. Dagan. High-order correction of effective permeability of heterogeneous isotropic formation of log-normal conductivity distribution. *Transport in Porous Media*, 12: 279–290, 1993.
- C. V. Deutsch. Calculating effective absolute permeability in sandstone/shale sequences. *SPE Formation Evaluation*, 4:343–348, 1989.
- C. V. Deutsch and A. G. Journel. *GSLIB: Geostatistical Software Library and User's Guide*. Oxford University Press, New York, 1998.
- L. J. Durlofsky. Numerical calculation of equivalent grid block permeability tensors for heterogeneous porous media. *Water Resources Research*, 27:688–708, 1991.
- L. J. Durlofsky. Representation of grid block permeability in coarse scale models of randomly heterogeneous porous media. *Water Resources Research*, 28:1791–1800, 1992.
- L. J. Durlofsky. Upscaling of geocellular models for reservoir flow simulation: a review of recent progress. In *Proceedings of the 7th International Forum on Reservoir Simulation*, Bühl/Baden-Baden, Germany, 2003.
- W. E and B. Engquist. The heterogeneous multi-scale methods. *Communication in Mathematical Sciences*, 1:87–133, 2003.
- W. E, B. Engquist, and Z. Huang. Heterogeneous multiscale method: a general methodology for multiscale modeling. *Physics Review B*, 67:092–101, 2003.

- Y. Efendiev and L. J. Durlofsky. Numerical modeling of subgrid heterogeneity in two phase flow simulations. *Water Resources Research*, 38, 2002.
- Y. Efendiev and L. J. Durlofsky. A generalized convection-diffusion model for subgrid transport in porous media. *Multiscale Modeling and Simulation*, 1:504–526, 2003.
- Y. Efendiev, L. J. Durlofsky, and S. H. Lee. Modeling of subgrid effects in coarse-scale simulations of transport in heterogeneous porous media. *Water Resources Research*, 36:2031–2041, 2000a.
- Y. Efendiev, T. Hou, and X. Wu. Convergence of a nonconformal multiscale finite element method. *SIAM Journal of Numerical Analysis*, 37:888–910, 2000b.
- Y. Efendiev, T. Hou, and T. Strinopoulos. Multiscale simulations of porous media flows in flow-based coordinate system. *Computational Geosciences*, 12:257–272, 2008.
- S. Ekrann and J. Mykkeltveit. Dynamic pseudos: how accurate outside their parent case? In *SPE Symposium on Reservoir Simulation*, SPE 29138, San Antonio, Texas, February 12-15 1995.
- C. L. Farmer. Upscaling: a review. *International Journal for Numerical Methods in Fluids*, 40:63–78, 2002.
- Y. Gautier, M. J. Blunt, and M. A. Christie. Nested gridding and streamline-based simulation for fast reservoir performance prediction. *Computational Geosciences*, 4:295–320, 1999.
- J. J. Gómez-Hernández and A. G. Journé. Stochastic characterization of grid-block permeabilities: from point values to block tensors. In *2nd European Conference on Mathematics of Oil Recovery*, pages 83–90, Arles, 1990.

- I. G. Graham, P. O. Lechner, and R. Scheichl. Domain decomposition for multiscale PDEs. *Numerische Mathematik*, 106:589–626, 2007.
- D. R. Guérillot and S. Verdière. Different pressure grids for reservoir simulation in heterogeneous reservoirs. In *SPE Symposium on Reservoir Simulation*, SPE 29148, San Antonio, Texa, February 12-15 1995.
- A. F. Gulbransen, V. L. Hauge, and K.-A. Lie. A multiscale mixed finite-element method for vuggy and naturally-fractured reservoirs. *SPE Journal*, accepted, 2009.
- H. Hajibeygi, G. Bonfigli, M. A. Hesse, and P. Jenny. Iterative multiscale finite-volume method. *Journal of Computational Physics*, 227:8604–8621, 2008.
- M. A. Hesse, B. T. Mallison, and H. A. Tchelepi. Compact multiscale finite volume method for heterogeneous anisotropic elliptic equations. *Multiscale Modeling and Simulation*, 7:934–962, 2008.
- L. Holden and B. F. Nielsen. Global upscaling of permeability in heterogeneous reservoirs: the Output Least Squares (OLS) method. *Transport in Porous Media*, 40:115–143, 2000.
- T. Hou and X. H. Wu. A multiscale finite element method for elliptic problems in composite materials and porous media. *Journal of Computational Physics*, 134:169–189, 1997.
- T. Y. Hou, A. Westhead, and D. Yang. A framework for modeling subgrid effects for two-phase flows in porous media. *Multiscale Modeling and Simulation*, 5(4):1087–1127, 2006.
- T. J. R Hughes. Multiscale phenomena: greens functions, the Dirichlet-to-Neumann formulation, subgrid scale models, bubbles and the origins of stabilized methods. *Computational Methods in Applied Mechanical Engineering*, 127:387–401, 1995.

- T. J. R Hughes, G.R. Feijóo, L. Mazzei, and J.B. Quincy. The variational multiscale method – a paradigm for computational mechanics. *Computational Methods in Applied Mechanical Engineering*, 166:3–24, 1998.
- T. J. R. Hughes, A. A. Oberai, and L. Mazzei. Large eddy simulation of turbulent channel flows by the variational multiscale method. *Physics of Fluids*, 13:1784–1799, 2001.
- P. Jenny and I. Lunati. Modeling complex wells with the multi-scale finite-volume method. *Journal of Computational Physics*, 228:687–702, 2009.
- P. Jenny, S. H. Lee, and H. A. Tchelepi. Multiscale finite-volume method for elliptic problems in subsurface flow simulation. *Journal of Computational Physics*, 187:47–67, 2003.
- P. Jenny, S. H. Lee, and H. A. Tchelepi. Adaptive multiscale finite-volume method for multiphase flow and transportaion in porous media. *Multiscale Modeling and Simulation*, 3:50–64, 2004.
- P. Jenny, S. H. Lee, and H. A. Tchelepi. Adaptive fully implicit multiscale finite-volume method for multiphase flow and transport in heterogeneous porous media. *Journal of Computational Physics*, 217:627–641, 2006.
- A. G. Journal, C. V. Deutsch, and A. J. Desbarats. Power averaging for block effective permeability. In *SPE California Regional Meeting*, SPE 15128, Oakland, California, April 2-4 1986.
- R. Juanes and F. X. Dub. A locally conservative variational multiscale method for the simulation of porous media flow with multiscale source terms. *Computational Geosciences*, 12:273–295, 2008.

- M. J. King and M. Mansfield. Flow simulation of geologic models. *SPE Reservoir Evaluation & Engineering*, 2:351–367, 1999.
- P. R. King. The use of renormalization for calculating effective permeability. *Transport in Porous Media*, 4:37–58, 1989.
- V. Kippe, J. E. Aarnes, and K. A. Lie. A comparison of multiscale methods for elliptic problems in porous media flow. *Computational Geosciences*, 12(3):377–398, 2008.
- J. R. Kyte and D. W. Berry. New pseudo functions to control numerical dispersion. *SPE Journal*, 15:269–275, 1975.
- P. Le Tallec and F. Mallinger. Coupling Boltzmann and Navier-Stokes equations by half fluxes. *Journal of Computational Physics*, 136:51–67, 1997.
- S. H. Lee, C. Wolfsteiner, and H. A. Tchelepi. A multiscale finite-volume method for multiphase flow in porous media: Black oil formulation of compressible, three phase flow with gravity. *Computational Geosciences*, 12:351–366, 2008.
- R. LeVeque. *Numerical Methods for Conservation Laws*. Birkhäuser, 1992.
- X. Li and W. E. Multiscale modeling of the dynamics of solids at finite temperature. *Journal of the Mechanics and Physics of Solids*, 53:1650–1685, 2005.
- W. K. Liu, E. G. Karpov, S. Zhang, and H. S. Park. An introduction to computational nanomechanics and materials. *Computer Methods in Applied Mechanics and Engineering*, 193:1529–1578, 2004.
- I. Lunati and P. Jenny. Multi-scale finite-volume method for highly heterogeneous porous media with shale layers. In *Proceedings of the 9th European Conference on the Mathematics of Oil Recovery (ECMOR)*, Cannes, France, 2004.

- I. Lunati and P. Jenny. Multi-scale finite-volume method for compressible multi-phase flow in porous media. *Journal of Computational Physics*, 216:616–636, 2006.
- I. Lunati and P. Jenny. Multi-scale finite-volume method for multi-phase flow with gravity. *Computational Geosciences*, 12:337–350, 2008.
- B. F. Nielsen and A. Tveito. An upscaling method for one-phase flow in heterogeneous reservoirs. A weighted output least squares (WOLS) approach. *Computational Geosciences*, 2:93–123, 1998.
- J. M. Nordbotten and P. E. Bjørstad. On the relationship between the multiscale finite-volume method and domain decomposition preconditioners. *Computational Geosciences*, 12:367–376, 2008.
- D. W. Peaceman. *Fundamentals of Numerical Reservoir Simulation*. Elsevier Scientific Publisher, 1977.
- G. E. Pickup, P. S. Ringrose, J. L. Jensen, and K. S. Sorbie. Permeability tensors for sedimentary structures. *Mathematical Geology*, 26:227–250, 1994.
- M. Ramè and J. E. Killough. A new approach to the simulation of flows in highly heterogeneous porous media. In *SPE Symposium on Reservoir Simulation*, SPE 21247, Anaheim, California, February 17-20 1991.
- P. Renard and G. de Marsily. Calculating effective permeability: a review. *Advances in Water Resources*, 20:253–278, 1997.
- Y. Rubin and J. J. Gómez-Hernández. A stochastic approach to the problem of upscaling of conductivity in disordered media: Theory and unconditional numerical simulations. *Water Resources Research*, 26:691–701, 1990.
- Y. Saad. *Iterative methods for sparse linear system*. PWS Publishing, 1996.

- T. E. Schwartzentruber and I. D. Boyd. A hybrid particle-continuum method applied to shock waves. *Journal of Computational Physics*, 215(2):402–416, 2006.
- B. F. Smith, P. E. Bjørstand, and W. D. Gropp. *Domain Decomposition*. Cambridge University Press, 1996.
- H. L. Stone. Rigorous black oil pseudo functions. In *SPE Symposium on Reservoir Simulation*, SPE 21207, Anaheim, California, February 17-20 1990.
- K. Stüeben. *Multigrid*, chapter Algebraic Multigrid (AMG): An Introduction with Applications. Academic Press, 2000.
- H. A. Tchelepi, P. Jenny, S. H. Lee, and C. Wolfsteiner. Adaptive multiscale finite volume framework for reservoir simulation. *SPE Journal*, 12:188–195, 2007.
- A. Toselli and O. Wildlund. *Domain Decomposition Methods – Algorithms and Theory*. Springer, 2005.
- J. Wallis and H. A. Tchelepi. Apparatus, method and system for improved reservoir simulation using an algebraic cascading class linear solver, 2007. Patent: US 2007/0010979 A1.
- T. C. Wallstrom, M. A. Christie, L. J. Durlofsky, and D. H. Sharp. Effective flux boundary conditions for upscaling porous media equations. *Transport in Porous Media*, 46:139–153, 2002a.
- T. C. Wallstrom, S. Hou, M. A. Christie, L. J. Durlofsky, D. H. Sharp, and Q. Zou. Application of effective flux boundary conditions to two-phase upscaling in porous media. *Transport in Porous Media*, 46:155–178, 2002b.
- X. H. Wen and J. J. Gómez-Hernández. Upscaling hydraulic conductivities in heterogeneous media: an overview. *Journal of Hydrolog*, 183:ixxxii, 1996.

- X. H. Wen, L. J. Durlofsky, and M. G. Edwards. Upscaling of channel systems in two dimensions using flow-based grids. *Transport in Porous Media*, 51:343–366, 2003a.
- X. H. Wen, L. J. Durlofsky, and M. G. Edwards. Use of border regions for improved permeability upscaling. *Mathematical Geology*, 35:521–547, 2003b.
- C. Wolfsteiner, S. H. Lee, and H. A. Tchelepi. Modeling of wells in the multiscale finite volume method for subsurface flow simulation. *Multiscale Modeling and Simulation*, 5:900–917, 2006.
- Y. Zhang, T. S. Lee, and W. Yang. A pseudobond approach to combining quantum mechanical and molecular mechanical methods. *Journal of Chemical Physics*, 110:46–54, 1999.
- H Zhou. Operator based multiscale method for compressible flow. Master’s thesis, Stanford University, 2006.
- H. Zhou and H. A. Tchelepi. Operator based multiscale method for compressible flow. *SPE Journal*, 13:267–273, 2008.